EUROPEAN COMMISSION

European Research Area

Long-term Performance of Engineered Barrier Systems

PEBS

Long-term Performance of Engineered Barrier Systems

PEBS

DELIVERABLE (D-N°: D3.3-3)

Modelling and interpretation of the FEBEX mock up test and of the long-term THM tests

Contract (grant agreement) number: ***FP7 249681***

Authors:

Marcelo Sánchez (Texas A&M), Antonio Gens (CIMNE-UPC)

Date of issue of this report: 02/05/14

Start date of project : **01/03/10** Duration : 48 Months

Project co-funded by the European Commission under the Seventh Euratom Framework Programme for Nuclear Research &Training Activities (2007-2011)		
Dissemination Level		
PU	Public	PU
RE	Restricted to a group specified by the partners of the PEBS project	
CO	Confidential, only for partners of the PEBS project	

EURATOM

TABLE OF CONTENT

List of Figures

List of Tables

Notation

$\mathbf{D}_e$	elastic matrix
$\mathbf{D}_{ep}$	elasto-plastic matrix
e	void ratio
e_M	macrostructural level void ratio
e_m	microstructural level void ratio
F_{LC}	*BBM* yield surface
F_{NL}	Neutral Line
f_β	interaction function for β mechanism
G	plastic potential
G_t	shear modulus
g	a lode angle function
$\mathbf{H}$	hardening modulus matrix
$\mathbf{H}^c$	critical softening matrix.
$\overline{\mathbf{H}}$	effective hardening matrix
$\mathbf{I}$	identity matrix
$\mathbf{i}^i_{\alpha j}$	non-advective mass flux (i=w,a; α=l,g; j=1,2)
$\mathbf{i}_{cj}$	non-advective heat flux (j=1,2)
J	2nd stress invariant of deviatoric stress tensor
J_h	hydraulic gradient
J_o	threshold hydraulic gradient
J_c	critical hydraulic gradient
$\mathbf{j}^i_{Ej}$	advective energy flux in α phase with respect to a fixed reference system (j=1,2)
$\mathbf{j}'^i_{Ej}$	advective energy flux in α phase with respect to the solid phase (j=1,2)
$\mathbf{j}^i_{\alpha j}$	total mass flux of i-species in α phase with respect to a fixed reference system (j=1,2)
$\mathbf{j}'^t_{\alpha j}$	total mass flux of i-species in α phase with respect to the solid phase (j=1,2)
$\mathbf{K}_{\alpha j}$	permeability tensor (α=l,g; j=1,2)
$\mathbf{k}_j$	intrinsic permeability tensor (j=1,2)
$k_{r\alpha j}$	α phase relative permeability (α=l,g; j=1,2)
K	global bulk modulus
K_s	macrostructural bulk modulus for changes in suction
K_T	macrostructural bulk modulus for changes in temperature
K_M	macrostructural bulk modulus for changes in mean stress

K_m	microstructural bulk modulus for changes in mean stress plus suction
k_s	parameter describing the increase in cohesion with suction
LC	Loading-Collapse yield surface (*BBM*)
lc	plastic mechanism related to *BBM*
$\mathbf{m}$	auxiliary unit vector $\mathbf{m}^T = (1,1,1,0,0,0)$
$\mathbf{m}_{LC}$	flow rule direction of *BBM*
$\mathbf{m}_\beta$	flow rule direction of mechanism β
M	slope of critical state line
MC	microstructural contraction path
MS	microstructural swelling path
mc	plastic mechanism related to *MC* path
ms	plastic mechanism related to *MS* path
$\hat{p}$	microstructural effective stress
p	mean net stress
p_c	reference stress
p_0	net mean yield stress at current suction and temperature
p_0^*	net mean yield stress for saturated conditions at reference temperature
p_{0T}^*	net mean yield stress for saturated conditions at current temperature
p_r	reference stress
$\mathbf{q}_{\alpha j}$	volumetric flux of α phase with respect to the solid ($\alpha=l,g;\ j=1,2$)
r	parameter defining the maximum macrostructural soil stiffness
$S_{\alpha j}$	volumetric fraction of pore volume occupied by α phase ($\alpha=l,g;\ j=1,2$)
S_{rl}	residual saturation
S_{ls}	maximum saturation
s_o	osmotic suction
s_t	total suction
T	temperature (T_0 = reference temperature)
T_v	time factor
t	time
$\mathbf{u}$	solid displacement vector
u_j	excess pores pressures ($j=1,2$)
V, V_v	volume, volume of pores

V_s	volume of solids
V_{vM}, V_{vm}	V_v of macrostructure and microstructure
$\boldsymbol{\alpha}_{sM}$	elastic vector associated with macrostructural suction
$\boldsymbol{\alpha}_{sm}$	elastic vector associated with microstructural suction
$\boldsymbol{\alpha}_T$	elastic vector associated with temperature
α	parameter related to the plastic potential
α_0	parameter for elastic thermal strain
α_1	parameter that relates p_o^* with T
α_2	parameter for elastic thermal strain
α_3	parameter that relates p_o^* with T
α_m	parameter controlling the microstructural soil stiffness
α_s	parameter controlling the soil stiffness (*BBM*)
α_{sp}	parameter controlling the soil stiffness (*BBM*)
$\boldsymbol{\beta}_{sM}$	elasto-plastic vector associated with macrostructural suction
β	indicates the direction of the microstructural stress path (β=*C* =>*MC* path , β=S =>M*S* path)
β_m	parameter controlling the microstructural soil stiffness
χ	F_{NL} slope
ΔT	temperature increment (T- T_0)
$\boldsymbol{\varepsilon}$	strain vector. $\{\varepsilon_x, \varepsilon_y, \varepsilon_z, \gamma_{xy}, \gamma_{xz}, \gamma_{yz}\}^T$
$\dot{\boldsymbol{\varepsilon}}^e$	elastic strain increment due to stress changes
$\dot{\boldsymbol{\varepsilon}}_s^e$	elastic strain increment due to suction changes
$\dot{\boldsymbol{\varepsilon}}_T^e$	elastic strain increment due to temperature changes
$\dot{\varepsilon}_{vm}$	elastic volumetric strain at microstructural level
ε_v^p	total plastic volumetric strain
ε_{vi}^p	plastic volumetric strain related to *i* plastic mechanism (i= *lc*, β)
$\boldsymbol{\gamma}_{sM}$	elasto-plastic vector associated with macrostructural suction
$\boldsymbol{\gamma}_{sm}$	elasto-plastic vector associated with microstructural suction
$\boldsymbol{\gamma}_T$	elasto-plastic vector associated with temperature
η	stress ratio
κ_i	macrostructural elastic stiffness parameter for changes in mean stress

κ_s macrostructural elastic stiffness parameter for changes in suction

κ_m parameter controlling the microstructural soil stiffness

$\lambda_{(s)}$ macrostructural stiffness parameter for changes in net mean stress for virgin states of soil at suction s

λ_o, λ_d retention curve parameters

μ Poisson's coefficient

$\mu_{\alpha j}$ dynamic viscosity of α phase (α=l,g; j=1,2)

∇ gradient vector

θ Lode's angle

$\theta^i_{\alpha j}$ ($=\rho_{\alpha j}\omega^i_{\alpha j}$)mass of i-species in α phase per unit volume of α phase (i=w,a; α=l,g; j=1,2)

$\omega^i_{\alpha j}$ mass fraction of i-species in α phase (i=w,a; α=l,g; j=1,2)

ρ parameter that relates cohesion and T

ρ_s solid density

$\rho_{\alpha j}$ mass of α phase per unit of volume of α phase (α=l,g; j=1,2)

$\boldsymbol{\sigma}_t$ total stress vector. $\left\{\sigma_x, \sigma_y, \sigma_z, \tau_{xy}, \tau_{xz}, \tau_{yz}\right\}^T_t$

$\boldsymbol{\sigma}$ net stress vector ($\boldsymbol{\sigma}_t - \mathbf{I}p_g$)

$\boldsymbol{\sigma}^*$ stress vector at the image point

$\hat{\boldsymbol{\sigma}}\}$ generalized stress vector

ω_β variable related to β mechanism (= +1 for *MC* path, or = -1 for *MS* path)

ζ parameter controlling the rate of increase of macrostructural soils stiffness with suction.

1. INTRODUCTION

This Deliverable contains the main results of the numerical analyses performed by CIMNE-UPC in the context of Work Package 3.3 of the PEBS Project. The numerical analyses have focused on the study of the THM (Thermo-Hydro-Mechanical) processes in the near field, with special attention to the behaviour of the clay barrier. A fully coupled THM formulation (Olivella et al., 1994) and the associated finite element program CODE_BRIGHT (Olivella et al., 1996) have been used in the simulations. CODE_BRIGHT has been developed to perform fully coupled THM problems in geological media. This code has been extensively verified and validated using different numerical solutions and actual cases, most of them associated with nuclear waste disposal,

Important THM phenomena take place in the engineered barrier and in the near field due to the combined actions of heating and hydration. For example, hydration takes place from the external boundary inwards driven by the gradient between the rock water pressure and the suction in the bentonite. Hydration causes a progressive rise in degree of saturation. These processes affect both the temperature field, due to the modifications of thermal conductivity, and the stress/strain distribution, due to suction changes. On the other hand, in the inner part of the buffer, applied heat causes a temperature rise that moves outwards. In addition, water evaporation causes drying of the bentonite close to the heat source. Vapour coming from the inner part of the barrier will diffuse towards the outer regions where it will condense causing a local rise of degree of saturation. Water transfer is also affected by the dependence of water viscosity on temperature and by porosity changes arising from variations of stresses and suction. There are other significant THM couplings in this kind of problem as discussed in the following sections. Therefore, coupled THM analyses are always required to achieve a good understanding of this problem.

Three experiments, all performed at CIEMAT, were modelled in this Work Package of the PEBS project, namely:

- two long-term infiltration cell tests: i) an isothermal cell test, and ii) a thermal gradient cell test, and
- mock-up test.

The numerical modelling has been performed with the objective of gaining a better understanding on the THM processes controlling the hydration of the clay barrier. Only if the buffer behaviour is successfully modelled on its own, the higher complexity introduced by the buffer/rock interaction can be satisfactorily tackled. Because of some divergences between model computations and observations, the analyses performed using a conventional THM formulation have been extended to incorporate a number of different additional hypotheses. Thus the main four types of analysis carried out have been:

- reference analyses, using the conventional THM formulation. It is named Operational Bases Case (OBC);
- analyses assuming non-Darcy flow due to the existence of a threshold gradient in the liquid flow law. It is coded as Threshold Hydraulic Gradient (THG) case;
- analyses incorporating thermo-osmosis, called Thermo Osmosis (THO) case;
- analyses incorporating the evolution of micro-fabric by means of a double structure constitutive law. Denoted as Double Structure (DS) case

This report is organized in five main sections. After this Introduction, Section 2 presents the main aspects of the basic THM formulation and computer code used in the numerical analyses. Section 3 is devoted to the study of the infiltration tests using the four different types of models

mentioned above. Section 4 examines the performance of the mock-up heating test focusing mainly on the comparisons between model predictions and experimental results under different hypotheses. Section 5 closes the report with the main conclusions from the THM modelling. An Appendix complements the information given in the main body of this Report.

2. FORMULATION AND COMPUTER CODE

2.1. Conventional formulation

The formulation reported in this section has been presented in more general terms in Deliverable D3.5-2 (Gens & Sanchez 2014). Here, this conventional formulation is described in somewhat more detail and with explicit references to the analyses to be described in later sections.

The formulation used is based on a macroscopic approach developed in the context of the continuum theory for porous media (Olivella et al., 1994). It is assumed that the porous medium is made up of three phases: solid, liquid and gas. The liquid phase contains water and dissolved air whereas the gas phase is made up of dry air and water vapour. The formulation incorporates basic thermal, hydraulic and mechanical phenomena in a coupled manner. The hydraulic component should be understood in a generalized way, i.e. including both liquid and gas flow.

The formulation allows the performance of coupled THM analyses within a unified and integrated framework. The approach also acts as a repository where new advances and developments have been incorporated and integrated. During the development of the project, there has been a growing knowledge of the THM behaviour of the engineered barrier and the near field components. Therefore, the formulation has been updated as new physical insight, experimental data and application results have become available. The condition is, of course, that the formulation is open, flexible and structured in an accessible way.

In this Section 2.1 the main parts of the conventional THM formulation are presented. The new developments are introduced later this Report, with Sections explicitly devoted to them. The basic THM formulation takes into account the following phenomena:

- Heat transport:
    - Heat conduction.
    - Heat convection (liquid water).
    - Heat convection (water vapour).
    - Phase changes
- Water flow:
    - Liquid phase.
    - Water vapour diffusion.
- Air flow:
    - Gas phase.
    - Air solution in water.
    - Dissolved air diffusion.
- Mechanical behaviour:
    - Thermal expansion of materials.
    - Behaviour of materials dependent on stresses, suction, water pressure and temperature.

The problem is approached using a multi-phase, multi-specie formulation that expresses mathematically the main THM phenomena in terms of:

- Balance equations.
- Constitutive equations.
- Equilibrium restrictions
- Phase physical properties

In the following Sections the basic aspects of these four main parts of the conventional formulation are presented.

2.1.1 Balance equations

The compositional approach has been adopted to establish the mass balance equations. This approach consists of balancing the species (mineral, water and air) rather than the phases (solid, liquid and gas). In this way the phase change terms do not appear explicitly, which is particularly useful when equilibrium is assumed. In the notation, the subscript is used to identify the phase (*s* for solid, *l* for liquid and *g* for gas) and the superscript indicates the species: *w* for water and *a* for air. No symbol is attributed to the mineral species, because it has been assumed that it coincides with the solid phase in this case. The main balance equations are presented in the following paragraphs, a more detailed description can be found elsewhere (i.e. Olivella et al., 1994).

Balance of mass of water:

$$\frac{\partial}{\partial t}\left(\theta_l^w S_l \phi + \theta_g^w S_g \phi\right) + \nabla.\left(\mathbf{j}_l^w + \mathbf{j}_g^w\right) = f^w \tag{1}$$

where θ_l^w and θ_g^w are the masses of water per unit volume of liquid and gas phase respectively. ϕ is the porosity and S_α is the volumetric fraction of pore volume occupied by the alpha phase (α=*l,g*). $\mathbf{j}_l^w$ and $\mathbf{j}_g^w$ denote the total mass fluxes of water in the liquid and gas phases with respect to a fixed reference system. f^w is the external mass supply of water per unit volume of medium.

Balance of mass of air:

$$\frac{\partial}{\partial t}\left(\theta_l^a S_l \phi + \theta_g^a S_g \phi\right) + \nabla.\left(\mathbf{j}_l^a + \mathbf{j}_g^a\right) = f^a \tag{2}$$

where θ_l^a and θ_g^a are the masses of air per unit volume of liquid and gas phase respectively. $\mathbf{j}_l^a$ and $\mathbf{j}_g^a$ denote the total mass fluxes of air in the liquid and gas phases with respect to a fixed reference system. f^a is the external mass supply of air per unit volume of medium. Note that dry air is considered as a single species in spite of the fact that it is a mixture of gasses. The gaseous phase is assumed as a mixture of air and water vapour. Air is also dissolved in the liquid phase.

Balance of energy:

$$\frac{\partial}{\partial t}\left[E_s \rho_s \left(1-\phi\right)\right] + \frac{\partial}{\partial t}\left(E_l \rho_l S_l \phi + E_g \rho_g S_g \phi\right) + \nabla.\left(\mathbf{i}_c + \mathbf{j}_{Es} + \mathbf{j}_{El} + \mathbf{j}_{Eg}\right) = f^E \tag{3}$$

The balance of energy has been expressed in terms of internal energy where E_s is the solid specific internal energy, E_l and E_g are specific internal energies corresponding to the liquid and gas phases respectively. ρ_l and ρ_g are the liquid and gas phase densities of the medium. f^E is the energy supply per unit volume of medium. The most important processes for energy transfer in a porous medium have been considered in (3), i.e. conduction, advection and phase change. $\mathbf{i}_c$ is the conductive heat flux. $\mathbf{j}_s$, $\mathbf{j}_{El}$ and $\mathbf{j}_{Eg}$ are the energy fluxes due to the motion of phase. In this approach, thermal equilibrium between the phases has been assumed, therefore the temperature is the same for the phases and only one equation of total energy is required. This assumption is generally valid in low permeability media.

Balance of mass of solid:

$$\frac{\partial}{\partial t}\left(\rho_s\left(1-\phi\right)\right)+\nabla\cdot\left(\rho_s\left(1-\phi\right)\dot{\mathbf{u}}\right)=0 \tag{4}$$

where $\dot{\mathbf{u}}$ is the solid velocity vector. The variation of porosities in terms of changes in solid density and volumetric deformation of the soil skeleton can be obtained from (4).

Balance of momentum (equilibrium):

$$\nabla.\boldsymbol{\sigma}_t+\mathbf{b}=0 \tag{5}$$

where $\boldsymbol{\sigma}_t$ is the total stress tensor and **b** the vector of body forces. In (5), inertial terms have been neglected. This assumption is appropriate because both velocities and accelerations are small, yielding terms that are negligible in comparison with the stress terms. The assumption of small strain rates is also made.

2.1.2 Constitutive equations

The constitutive equations establish the link between the unknowns and the dependent variables. There are several categories of dependent variables depending on the complexity with which they are related to the unknowns. The governing equations are finally written in terms of the unknowns when the constitutive equations are substituted in the balance equations. Here, the basic constitutive laws are presented, divided in thermal, hydraulic and mechanical. In spite of this distinction between the three basic components of the problem, the constitutive equations provide in fact the links that couple the various phenomena considered in the formulation. The general expressions of the constitutive laws for the thermal, hydraulic and mechanical problems are presented below. Some additional specific models are introduced when the analyses of the mock-up test and the in-situ test are presented.

2.1.2.1 Thermal

Conductive heat flow is assumed to be governed by Fourier's law:

$$\mathbf{i}_c=-\lambda\nabla T \tag{6}$$

where λ is the global thermal conductivity of the porous medium, generally dependent on degree of saturation and porosity. A general expression, based on the geometric mean of the thermal conductivities of the three phases can be expressed as:

$$\lambda=\lambda_{sat}^{\,S_l}\lambda_{dry}^{\,(1-S_l)} \tag{7}$$

where the values of λ_{sat} = 1.15 and λ_{dry} = 0.47 W/mºC have been obtained based on the experimental measurements presented in Figure 1 (FEBEX Report, 2000).

The internal energy for the medium is computed assuming that it is additive in relation to the phase (Olivella et al., 1994). The procedure to evaluate the internal energy per each phase is presented in the Appendix.

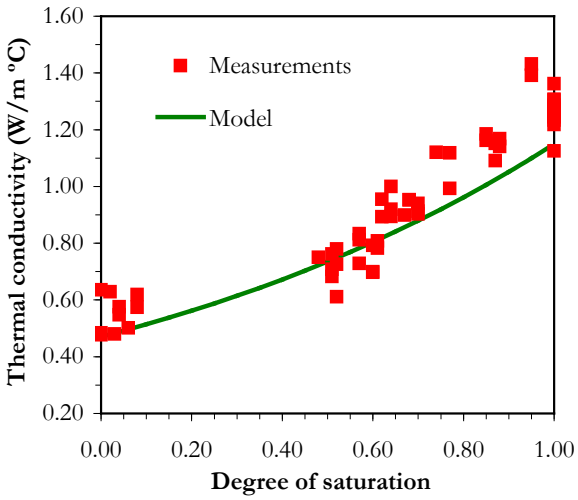

Figure 1. Experimental results and adopted thermal conductivity law for the FEBEX bentonite.

2.1.2.2 Hydraulic

Advective phase fluxes (both liquid and water) are computed using generalized Darcy's law, expressed as:

$$\mathbf{q}_\alpha = -\mathbf{K}_\alpha \left(\nabla P_\alpha - \rho_\alpha \mathbf{g}\right); \qquad \alpha = l, g \tag{8}$$

where P_α is the phase pressure, $\mathbf{K}_\alpha$ is the permeability tensor of α phase and **g** is the gravity vector. The permeability tensor is not constant but it depends on other variables, according to:

$$\mathbf{K}_\alpha = \mathbf{k}\frac{k_{r\alpha}}{\mu_\alpha}; \qquad \alpha = l, g \tag{9}$$

where **k** is the intrinsic permeability tensor, μ_α is the dynamic viscosity of the α phase and $k_{r\alpha}$ is the α phase relative permeability. The dependence of intrinsic permeability on pore structure is considered in terms of total porosity according to:

$$\mathbf{k} = k_0 \frac{\phi^3}{(1-\phi)^2}\frac{(1-\phi_0)^2}{\phi_0^3}\mathbf{I} \tag{10}$$

where k_0 is the reference permeability at the reference porosity ϕ_0.

Figure 2 shows experimental measurements of saturated permeability at different densities for FEBEX bentonite, together with the results obtained from equation (10). The reference permeability adopted is $k_0 = 1.9\text{x}10^{-21}$ m^2, for a reference porosity of $\phi_0 = 0.4$.

The relative permeability of the liquid phase (k_{rl}) is made dependent on the degree of saturation according to:

$$k_{rl} = S_{el}^{\ n} \tag{11}$$

where n is a model parameter and S_{el} the effective degree of saturation, evaluated as follows:

$$S_{el} = \frac{S_l - S_{lr}}{S_{ls} - S_{lr}} \tag{12}$$

where S_{lr} is the residual saturation and S_{ls} is the maximum saturation. The relative permeability of the gaseous phase (k_{rg}) is obtained as follows:

$$k_{rg} = A S_g^{n_g} \tag{13}$$

where A and n_g are a model parameters.

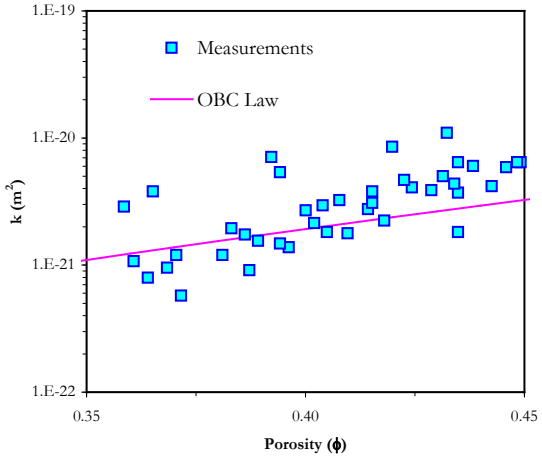

Figure 2. Variation of saturated permeability with porosity. Experimental data and adopted model for the intrinsic permeability law.

Equation (11) considers the reduction of hydraulic permeability as the degree of saturation decreases. This variation is very difficult to determine directly and it is necessary to resort to indirect means of estimation. During the pre-operational study, the parameters of the relative permeability law for the bentonite were determined from the backanalysis of the results of a hydration test carried out in a small cell (FEBEX Report, 1998). The law determined in that study has been adopted. The law parameters are: $S_{lr} = 0.01$; $S_{ls} = 1.0$ and $n = 3$.

Very low values of intrinsic permeability were measured in FEBEX bentonite under saturated conditions. On the other hand, much higher values are observed when the permeability to gas was determined in unsaturated conditions. Differences close to seven orders of magnitude were measured between water and gas intrinsic permeability for dry densities ranging from 1.65 and 1.70 Mg/m^3. For instance, gas permeability close to 2.2x10^{-15} m^2 was measured for a $S_l \approx 0.61$ and for a dry density of 1.70 Mg/m^3 (Lloret & Villar, 2001). According to that, it is difficult to assume a single value of intrinsic permeability for FEBEX bentonite. If the value of intrinsic permeability for water were used, the gas permeability obtained is several orders of magnitude smaller than the actual values. In fact, the gas permeability is computed as the product of the intrinsic permeability (evaluated for the corresponding porosity) by the relative permeability to gas obtained applying Equation (13), divided by the gas viscosity. The correct inclusion in the modelling of this high contrast between gas and liquid permeabilities is still an open matter, probably related to the micro-fabric evolution of the material.

In the modelling, a very simple modification has been adopted to consider a gas permeability closer to the values measured in the laboratory. In order to maintain the concept of intrinsic permeability, a correction has been applied to the relative permeability law, pre-multiplying (13) by a factor large enough (i.e. A=1.0x10^7) to ensure a gas mobility in the FEBEX bentonite close to the values of gas permeability measured in the laboratory tests.

The retention curve adopted in the OBC analysis is based on the one proposed by van Genuchten (1978). The relation between degree of saturation and suction is given by:

$$S_{el} = \left[1+\left(\frac{s}{P_o}\right)^{\frac{1}{1-\lambda_o}}\right]^{-\lambda_o} f_d \tag{14}$$

where P_o and λ_o are model parameters and f_d is a function included in order to model properly the high suction range where. The adopted expression is the following:

$$f_d = \left(1-\frac{s}{P_d}\right)^{\lambda_d} \tag{15}$$

where P_d is related with the suction at 0 degree of saturation and λ_d is a model parameter. When $\lambda_d = 0$ the original model is recovered (*i.e.* Gens et al., 1998).

To determine the retention curve of FEBEX bentonite, tests under conditions of 'free' and 'constant' volume were performed (FEBEX II Report, 2004). The results obtained under constant volume conditions have been used to obtain the model parameters, since this condition is closer to the confined conditions of the tests analysed. Figure 3 presents the results of these tests together with the model adopted in the analysis of the mock-up test. The adopted model parameters are presented in Table 1. Experimental results have shown that, in most cases, the influence of temperature on retention curve is small (FEBEX II Report, 2004).

Table 1. Parameters related to the retention curve used in analysis.

P_0 (MPa)	λ_o	λ_d	P_d (MPa)
28	0.18	1.1	1100

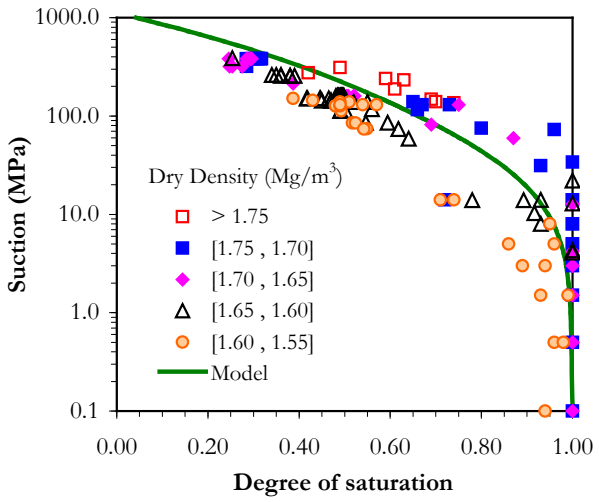

Figure 3. Retention curve adopted, together with the experimental data of FEBEX bentonite (symbols).

Non-advective fluxes of species inside the fluid phases are computed through Fick's law, which expresses them in terms of gradients of mass fraction of species through a hydrodynamic dispersion tensor that includes both molecular diffusion and mechanical dispersion:

$$\mathbf{i}_\alpha^i = -\mathbf{D}_\alpha^i \nabla \omega_\alpha^i; \qquad i = w,a; \qquad \alpha = l,g \tag{16}$$

where $\mathbf{D}^i_\alpha$ is the dispersion tensor of the medium. For vapour diffusion, the following expression for the hydrodynamic dispersion tensor is adopted:

$$\mathbf{i}^w_g = -\mathbf{D}^w_g \nabla \omega^w_g = -\left(\phi \rho_g S_g \tau D^w_m \mathbf{I} + \rho_g \mathbf{D}'_g\right) \nabla \omega^w_g \tag{17}$$

where D_m^w is the dispersion coefficient corresponding to molecular diffusion of vapour in air, D'_g is the mechanical dispersion tensor and τ is the tortuosity. Tortuosity takes into account the fact that the vapour diffusion takes place inside the voids of a porous media. A tortuosity $\tau = 0.8$ (vapour diffusion law) has been adopted (FEBEX Report, 2000).

The molecular diffusion coefficient is given by:

$$D^w_m = 5.9x10^{-12} \frac{\left(273.15 + T\right)^{2.3}}{P_g} \tag{18}$$

where D_m^w is in m^2/s, P_g is in MPa and T in ºC. It can be noted that in vapour diffusion, the THM couplings are evident: thermal effects through the variation of molecular diffusion with temperature; hydraulic effect through the influence of degree of saturation; and mechanical effects due to porosity changes. In the simulations it has been assumed that the molecular diffusion is dominant and the mechanical dispersion of vapour has been neglected. The same consideration can be made regarding diffusion of air in the liquid phase:

$$\mathbf{i}^a_l = -\mathbf{D}^a_l \nabla \omega^a_l = -\left(\phi \rho_l S_l \tau D^a_m \mathbf{I} + \rho_l \mathbf{D}'_l\right) \nabla \omega^a_l \tag{19}$$

2.1.2.3 Mechanical

A constitutive equation showing explicitly the contributions of strains, temperature and fluid pressures can be expressed generically as:

$$\dot{\boldsymbol{\sigma}} = \mathbf{D}\dot{\boldsymbol{\varepsilon}} + \mathbf{f}\dot{s} + \mathbf{t}\dot{T} \tag{20}$$

where $\boldsymbol{\sigma}$ is the constitutive stress (net or effective stress), $\boldsymbol{\varepsilon}$ is the strain vector, s is the matric suction computed as the difference between gas pressure and liquid pressure (p_g- p_l), $\mathbf{D}$ is the constitutive stiffness matrix, $\mathbf{f}$ is the generic constitutive vectors relating the changes in the fluid pressures and stresses and $\mathbf{t}$ is the constitutive vector relating stresses and temperature. The two main mechanical models adopted in the simulations are presented in the following sections, namely, the Barcelona basic model and the double structure model.

2.1.2.3.1 Barcelona Basic Model

The Barcelona Basic Model, BBM, (Alonso et al., 1990) has been selected as the basis for the thermoplastic constitutive law in the OBC analysis. The BBM considers two independent stress variables to model the unsaturated behaviour: the net stress ($\boldsymbol{\sigma}$), computed as the excess of the total stresses over the gas pressure ($\boldsymbol{\sigma}_t$-$\mathbf{I}p_g$), and the matric suction (s). The BBM is an elasto-plastic model in which the yield surface depends not only on stresses (and history variables) but also on matric suction and temperature. The model is formulated in terms of three stress invariants (p, J, θ), suction (s) and temperature (T), where p is the mean net stress, J is the square root of the second invariant of deviatoric stress tensor and θ is Lode's angle. The expressions for the evaluation of the invariants are presented in the Appendix.

The BBM yield surface (F_{LC}) is expressed as follows:

$$F_{LC} = 3J^2 - \left[\frac{g(\theta)}{g(-30^o)}\right]^2 M^2 (p + p_s)(p_0 - p) = 0 \quad (21)$$

where M is the slope of the critical state, p_o is the apparent unsaturated pre-consolidation pressure, $g(\theta)$ is a function of the Lode angle (θ) and p_s considers the dependence of shear strength on suction and temperature.

The hardening law is expressed as a rate relation between the volumetric plastic strain (ε_v^p) and the saturated isotropic pre-consolidation stress (p^*_0), according to:

$$\dot{p}_0^* = \frac{(1+e)}{(\lambda_{(0)} - \kappa)} p_0^* \dot{\varepsilon}_v^p \quad (22)$$

where e is void index, κ is the elastic stiffness parameter for changes in net mean stress and $\lambda_{(0)}$ is the compressibility parameter for changes in net mean stress for virgin states of the soil in saturated conditions.

The mathematical formulation of the BBM is presented in the Appendix. A relevant aspect to comment here is that the original BBM is not able to reproduce satisfactorily the swelling behaviour of clays. Therefore, some modifications in the elastic part of the model are introduced in order to reproduce the expansive behaviour of FEBEX bentonite. This is mainly due to the fact that the description of the material behaviour inside the yield surface is particularly important due to the high compaction that the bentonite blocks have been subjected to. The variation of stress-stiffness with suction and, especially, the variation of swelling potential with stress and suction have been considered. The resulting elastic model is the following:

$$\dot{\varepsilon}_v^e = \frac{\kappa}{(1+e)} \frac{\dot{p}}{p} + \frac{\kappa_s}{(1+e)} \frac{\dot{s}}{(s + p_{at})} + (\alpha_0 + \alpha_2 \Delta T)\dot{T} \quad (23)$$

$$\dot{\varepsilon}_s^e = \frac{\dot{J}}{G_t} \quad (24)$$

where ε_v^e and ε_s^e are the volumetric and deviatoric component of the elastic strain, respectively. κ_s is the elastic stiffness parameter for changes in suction; α_0 and α_2 are model parameters, ΔT is the temperature difference with respect to an arbitrary reference temperature T_0 and G_t is the shear modulus, obtained from a linear elastic model (more details are given in the Appendix).

The following expression has been proposed to evaluate the elastic stiffness parameter for changes in net mean stress:

$$\kappa = \kappa_0 (1 + \alpha_s s) \quad (25)$$

where κ_0 is the elastic stiffness parameter in saturated conditions and α_s is a model parameter. The elastic stiffness parameter for changes in suction is computed according to:

$$\kappa_s = \kappa_{s0} (1 + \alpha_{sp} \ln p / p_{ref}) \quad (26)$$

where κ_{s0} and α_{sp} are model parameters

The parameters of the mechanical model have been mainly determined from back-calculation of swelling pressure tests during the pre-operational stage of the experiments (FEBEX Report,

1998). As an example of the constitutive law capabilities, Figure 4 presents the model prediction in a swelling pressure test. The stress path prescribed in this simulation is similar to the one followed by a point located close to the heater, that is, an initial drying (in this case close to the 200 MPa) followed by wetting. In the same Figure, the results of the swelling pressure tests carried out on samples with two different dry densities are also shown. As it can be observed, the model results can be considered satisfactory, because the stress path is reasonably well reproduced as well as the observed value of the swelling pressure. Changing the parameters would lead to a closer agreement, but only the overall model behaviour is intended to be demonstrated here.

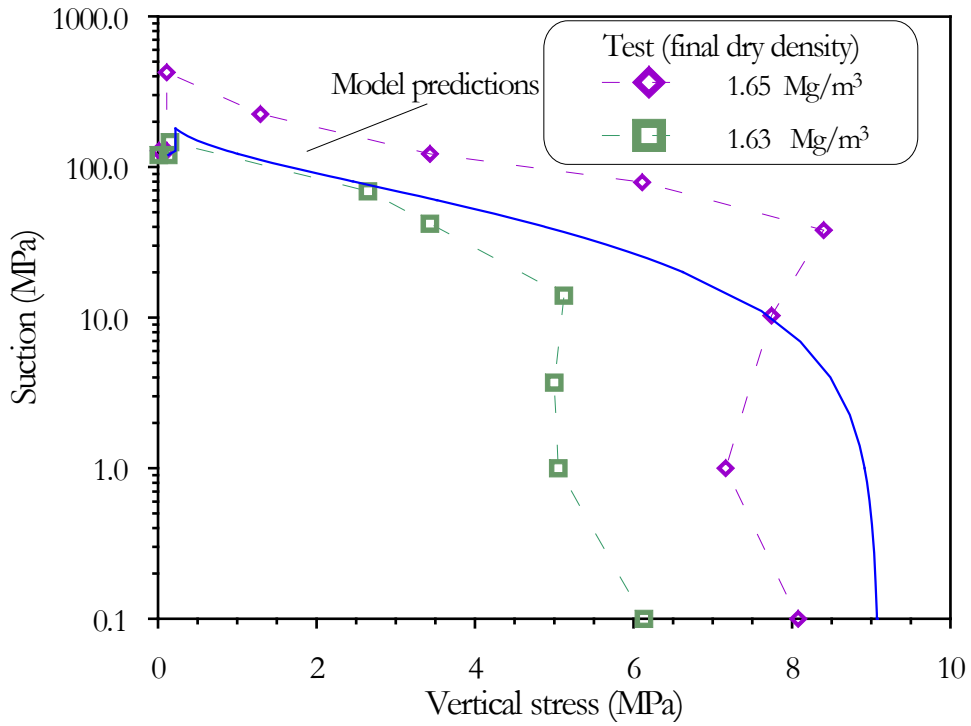

Figure 4. Computed stress path for swelling pressure tests using the BBM. Experimental results are provided for comparison.

Figure 5 shows experimental data of the thermal response of FEBEX bentonite (for dry densities between 1.60 and 1.70 Mg/m^3). The data identified as CIEMAT and UPC correspond to oedometer tests carried out at constant vertical stress and in conditions of constant water content (hygroscopic conditions). The data coded as Pintado (2002) result from tests performed under conditions of free expansion and with a liquid degree of saturation close to 92 %. Figure 5 also presents the output obtained with the adopted thermoelastic model.

Finally, Table 2 presents the adopted parameters of the BBM model in the OBC analyses of the mock-up and in-situ tests.

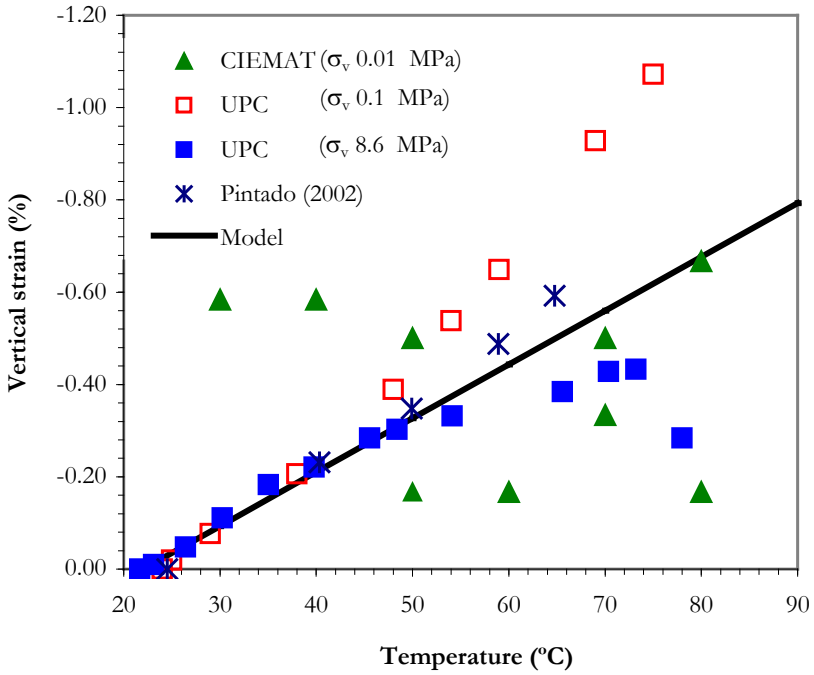

Figure 5. Comparisons between computed and measured thermal swelling at constant water content (FEBEX II Report, 2004; Pintado, 2002).

Table 2. Parameters of the Barcelona Basic Model adopted in the OBC analyses.

κ_0	0.05	$\lambda_{(0)}$	0.15
κ_{s0}	0.30	r	0.925
μ	0.40	ζ	0.10
α_s (MPa)	-0.003	ρ ($^oC^{-1}$)	0.20
α_{sp}	-0.147	k	0.10
p_{ref} (MPa)	0.01	p_c (MPa)	0.50
α_0 ($^oC^{-1}$)	$1.5x10^{-4}$	M	1.00
α_2($^oC^{-2}$)	0	α	0.53
μ	0.40	p_o^* (MPa)	12.0
α_1 ($^oC^{-1}$)	0	α_3 ($^oC^{-2}$)	0

2.1.2.3.2 Double Structure Model

This section presents the main components of the double structure model used in some numerical analyses. Background information about the fabric prevailing in expansive clays is introduced first. Then, the main components of the double structure model are described. Finally the basic ingredients of the mathematical formulation of the model are presented.

Background on clay fabric

The fabric of the compacted swelling clays plays an important role in the behaviour of these materials. The structure of the FEBEX bentonite has been studied using a variety of techniques. For instance, Mercury Intrusion Porosimetry (MIP) tests were performed to examine the pore size distribution of the statically compacted material used in the experimental programme. Figure 6 shows the measured incremental pore volume for two samples compacted to quite different values of dry density (ρ_d), 1.5 Mg/m^3 and 1.8 Mg/m^3. It can be clearly observed the characteristic bi-modal pore size distribution of compacted expansive materials. The dominant values are 0.01 μm that would correspond to the pores inside clay aggregates and a larger pore size, that depends on the compaction dry density and ranges from 10 μm (for ρ_d=1.8 Mg/m^3) and 40 μm (for ρ_d=1.5 Mg/m^3). These larger voids would correspond to the inter-aggregate pores. The boundary between the two pore size families can be seen to be around 0.13 μm, as pores smaller than this magnitude do not appear to be affected by the magnitude of the compaction load. As Figure 6 clearly shows, compaction affects mainly the pore structure of the larger inter-aggregate pores.

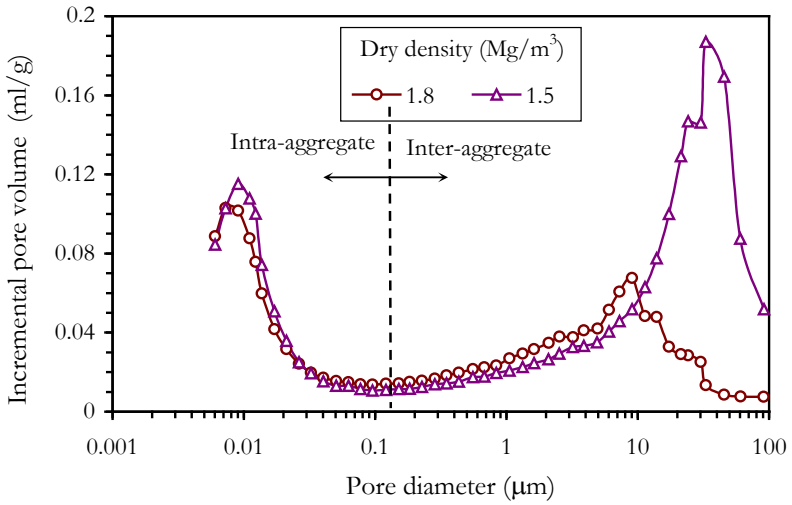

Figure 6. Distribution of incremental pore volume for two compacted bentonite samples at different dry densities. Mercury intrusion porosimeter test (Lloret et al., 2003).

These two dominant pore sizes can be associated with two basic structural levels (Figure 7):

- the macrostructure, composed by arrangements of clay aggregates, with macropores between them, and,
- the microstructure, which corresponds to the active clay minerals and their vicinity.

The microstructure is the seat of the basic physical-chemical phenomena occurring at clay particle level. These phenomena underlie the behaviour of expansive soils. On the other hand, deformations due to loading and collapse will have a major effect at the macrostructural level. This macrostructural behaviour can be described by concepts and models of conventional

unsaturated non-expansive soils. In addition, a proper modelling of the expansive clays behaviour requires the consideration of the interactions between the two basic structural levels defined above.

The behaviour of unsaturated expansive clays is potentially very complex since it results from the interaction between the volume change of aggregates made up from a highly expansive clay mineral (microstructural level) and the rearrangement of the granular-like skeleton formed by the aggregates (macrostructural level). Experimental studies of the FEBEX bentonite structure and information on the main mechanisms and phenomena that control the adsorption of water in expansive clays are presented in detail in FEBEX II Report (2004) and Fernández (2004). Particularly helpful has been the experimental study related to the changes in the fabric of the FEBEX bentonite during wetting and drying. A systematic study of this issue was performed using a Scanning Electron Microscope (SEM) and an Environmental Scanning Electron Microscope (ESEM).

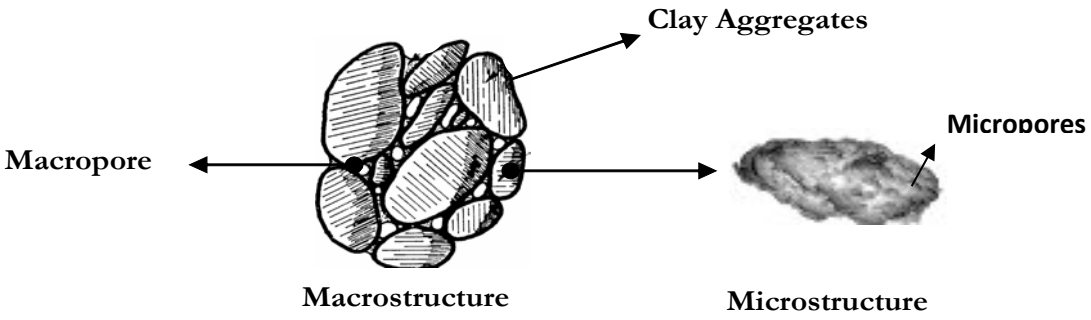

Figure 7. Schematic representation of the two structural levels considered.

A key aspect of the behaviour of compacted expansive bentonite is that the clay fabric is not static during hydration, but subject to change. For example, the change in clay structure generated by the progressive wetting of compacted bentonite with an initial dry density of 1.40 Mg/m^3 can be observed in Figure 8. Figure 8a shows a micrograph obtained using SEM where the presence of aggregates, the size of inter-aggregate voids and the bimodal distribution of pore sizes are readily apparent. Suction changes under isochoric conditions were applied to specimens before subjecting them to microstructural observations. Figure 8b presents the image of the clay fabric after application of a suction of 10 MPa ($\rho_{d\ final}$=1.46 g/cm^3) on bentonite initially compacted under hygroscopic conditions to ρ_d=1.65 Mg/m^3. Figure 8c shows the micro-fabric, after saturation under isochoric conditions ($\rho_{d\ final}$=1.43 g/cm^3), on bentonite initially compacted with hygroscopic water content to ρ_d=1.65 Mg/m^3. The differences in final dry density are due to the rebound experienced by the bentonite after unloading.

The progressive occlusion of the inter-aggregate pores due to particle swelling can be easily noted. Although the observations provide mainly qualitative information, the use of this technique allows the improvement of the knowledge of the structure changes due to hydration. As it can be observed in Figure 8, during hydration the clay fabric exhibits a dynamic character that can affect strongly the kinetics of hydration, especially if confined conditions prevail. Single porosity models are not able to handle properly the role that the structure of the swelling clays may play during hydration. Therefore, in order to perform a more detailed analysis of the clay fabric effects, a double structure THM formulation has been developed. A more suitable framework has been adopted to simulate problems in which two different pore levels (the macro and micro structure of the FEBEX bentonite) can be clearly distinguished. This approach would allow the adoption of a conceptual model for the hydration of the swelling clays closer to the observed behaviour. The explicit consideration of the two dominant levels of pores can also assist towards a better understanding of some key processes that take place during heating and hydration of the expansive clay.

.

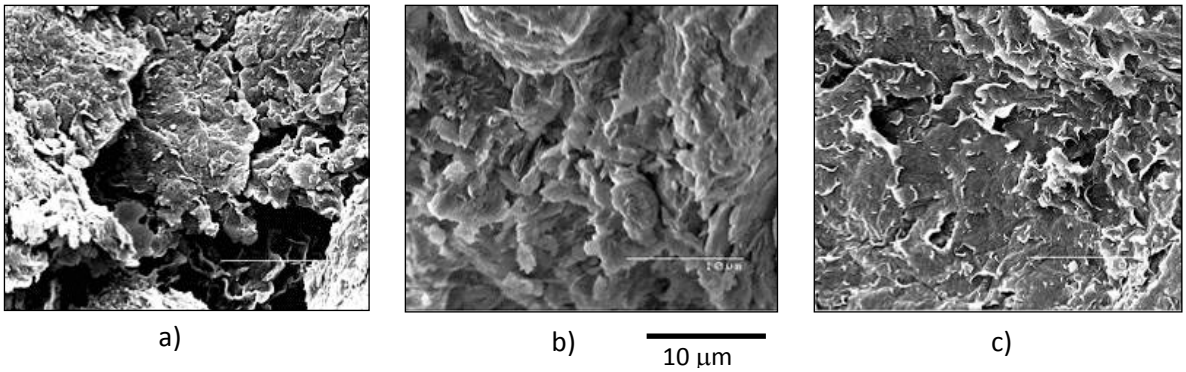

Figure 8. Micrographs (SEM, x 6000). a) Compacted with hygroscopic water content to ρ_d=1.40 g/cm^3. b) After application of a suction of 10 MPa in isochoric conditions ($\rho_{d\ final}$=1.46 g/cm^3) on bentonite initially compacted in hygroscopic conditions to ρ_d=1.65 Mg/m^3 and c) after saturation in isochoric conditions (ρ_d final=1.43 g/cm^3) on bentonite initially compacted with hygroscopic water content to ρ_d=1.65 Mg/m^3 (FEBEX II Report, 2004).

Mathematical Model

Due to the strong influence of the mechanical problem on the swelling clay behaviour, the mechanical constitutive law is a key element in the modelling of these materials. The model described here integrates the main aspects of expansive clay behaviour in a unified and formal framework. The mechanical law is based on the general approach proposed by Gens & Alonso (1992) and also considers some of the improvements proposed by Alonso et al. (1999) and Sánchez et al. (2005). Particular attention is placed on clay fabric and how it can be incorporated in the constitutive modelling of expansive soils.

The mechanical model has been developed using concepts of elasto-plasticity for strain hardening materials. As the BBM, the model is formulated in terms of the three stress invariants (p, J, θ), suction (s) and temperature (T), where p is the mean net stress, J is the square root of the second invariant of deviatoric stress tensor and θ is Lode's angle (see the Appendix).

A characteristic of this model is the explicit consideration of the two main structural levels identified previously (i.e. Figure 7), and also the interaction between the two structures. Therefore, the complete formulation of the model requires the definition of laws for describing the behaviour of:

- The macrostructural level.
- The microstructural level.
- The interaction between the structural levels.

Macrostructural model

The inclusion of this structural level in the analysis allows the consideration of phenomena that affect the skeleton of the material, for instance deformations due to loading and collapse. These phenomena have a strong influence on the macroscopic response of expansive materials. The macrostructural behaviour can be described by concepts and models of unsaturated non-expansive soils, such as the elasto-plastic Barcelona Basic Model (BBM) presented in Section 2.1.2.3.1. In the double structure model constant values of κ and κ_s are assumed. Figure 9a presents a three dimensional representation of BBM in the space: p, J, s.

Microstructural model

The microstructure is associated to the active clay minerals, and its behaviour is controlled mainly by the physico-chemical phenomena occurring at this level. It is assumed that these phenomena are basically reversible. The strains arising from microstructural phenomena are considered elastic and volumetric. The microstructural effective stress is defined as:

$$\hat{p} = p + \chi s_t ; \qquad s_t = s_2 + s_o \tag{27}$$

where s_o the osmotic suction. It is assumed that χ is a constant ($\chi > 0$) and that the total suction (s_t) is equal to the matric suction (s_2), because the effect of the osmotic suction is not explicitly considered in this work. In Guimarães et al. (2001), the formulation is extended to include geochemical variables. In equation (27) hydraulic equilibrium between the water potentials of both structural levels is assumed (this implies $s=s_1=s_2$). The extension of the constitutive model to handle problems in which this hypothesis is released is presented in Sanchez (2004).

In the *p-s* isotropic plane, the line corresponding to constant microstructural effective stresses is referred to as Neutral Line (*NL*), since no microstructural deformation occurs when the stress path moves on it (Figure 9.b). The increment of microstructural elastic strains is expressed as:

$$\dot{\varepsilon}^{e}_{v_1} = \frac{\dot{\hat{p}}}{K_1} = \frac{\dot{p}}{K_1} + \chi \frac{\dot{s}}{K_1} \tag{28}$$

where the subscript 1 refers to the microstructural level and the superscript *e* refers to the elastic component of the volumetric (subscript *v*) strains. For the microstructural bulk modulus (K_1) the following law has been adopted:

$$K_1 = \frac{e^{-\alpha_m \hat{p}}}{\beta_m} \tag{29}$$

where α_m and β_m are model parameters.

According to Figure 9.b) the Neutral Line divides the *p-s* plane into two parts (Figure 9.b), identified as:

$\hat{p} > 0 \quad \Rightarrow$ microstructural contraction (*MC*) ; $\qquad \hat{p} < 0 \quad \Rightarrow$ microstructural swelling (*MS*)

Interaction between structural levels

In expansive soils there are other mechanisms in addition to the ones included in the BBM that induce plastic strains. This irreversible behaviour is attributed to the interaction between the macro and micro structures. Analysing the behaviour of expansive clays under cycles of suction reversals (e.g. Pousada, 1984), two main aspects can be highlighted: the irreversible behaviour appears independent of the applied suction and it is difficult to determine the initiation of yielding. These facts suggest the use of the more general framework of generalized plasticity theory to formulate the model. In a generalized plasticity model the yield function is not defined or, at least, it is not defined in an explicit way. This is particularly advantageous in expansive materials, because no clear evidence exists concerning the shape of the internal yield surfaces corresponding to the interaction mechanisms between the two structural levels (Sánchez et al., 2005).

A basic assumption is that the microstructural behaviour is not affected by the macrostructure but the opposite is not true, i.e. macrostructural behaviour can be affected by microstructural deformations, generally in an irreversible way. It is assumed that that the irreversible deformations of the macrostructure are proportional to the microstructural strains according to interaction functions *f*. The plastic macrostructural strains are evaluated by the following expression:

$$\dot{\varepsilon}_{v2}^{p} = f\,\dot{\varepsilon}_{v1}^{e} \tag{30}$$

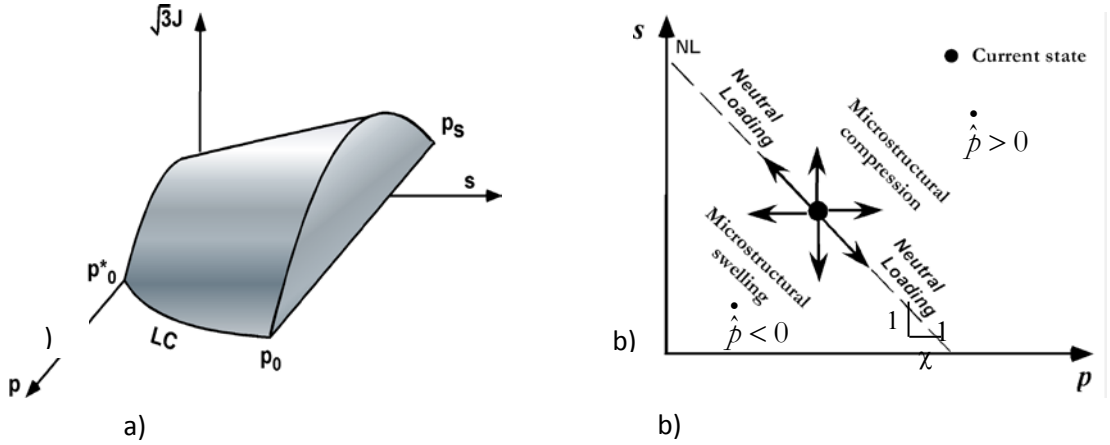

Figure 9. a) Three dimensional representation of the BBM yield surface. b) Definition of microstructural swelling and contraction directions.

Two interaction functions *f* are defined: f_c for microstructural contraction paths and f_S for microstructural swelling paths. In the case of isotropic load, the interaction function depends on the ratio p/p_o (p_o is the net mean yield stress at current suction and temperature). This ratio is a measure of the degree of openness of the macrostructure. When p/p_o is low it implies a dense packing of the material. It is expected that, under this condition, the microstructural swelling (*MS* path) affects strongly the global arrangements of clay aggregates. Therefore, the higher values of the f_s function correspond to low values of p/p_o. In this case the microstructure effects induce a more open macrostructure, which implies a macrostructural softening. On the other hand, when the microstructure contracts (*MC* path) the larger (induced) macrostructural plastic strains occur with open macrostructures (values of p/p_o close to 1). Under this path the clay tends to a more dense state, which implies a hardening of the macrostructure. This coupling between both plastic mechanisms is considered mathematically assuming that:

$$\dot{\varepsilon}_{v}^{p} = \dot{\varepsilon}_{vLC}^{p} + f\,\dot{\varepsilon}_{v1}^{e} \tag{31}$$

where ε_{vLC}^{p} is the plastic strains induced by the yielding of the macrostructure (BBM). In fact the coupling is given by p_o^*, the hardening variable of the macrostructure (Figure 9a), which depends on the total plastic volumetric strain (22). In this way, the possibility that microstructural effects can affect the global arrangements of aggregates (macrostructure) is taken into account.

Note that the material response will depend strongly on the direction of the microstructural stress path relative to the *NL*, which delimits two regions of different material behaviour. A proper modelling of this behaviour requires the definition of specific elasto-plastic laws for each domain, in order to describe correctly the material behaviour according to the microstructural stress path followed (*MC* or *MS*). Generalized plasticity theory can deal with such conditions,

allowing the consideration of two directions of different behaviour and the formulation of proper elasto-plastic laws for each region (Sánchez et al., 2005).

In summary, the behaviour of the macrostructure is modelled in the context of classical plasticity (BBM). This is a proper framework because the yield surface associated to this behaviour can be generally inferred using the usual methodology of classic plasticity. The microstructural effects have been modelled using a nonlinear elastic model. The interaction between both structural levels has been modelled using the more general framework of generalized plasticity theory. As described in Sánchez (2004) and Sánchez et al. (2005), the governing small strain-stress equations have been obtained using a general framework for multidissipative materials. Finally the numerical integration of the model has been performed using a scheme with error control.

Laboratory tests carried out in the context of the FEBEX project have been used to validate the double structure mechanical model. Oedometric tests, swelling pressure tests and experiments aimed to examine the structure of the FEBEX bentonite have been used to identify the main model parameters. A detailed description of this study can be found in Lloret et al. (2003).

2.1.3. Equilibrium restrictions

It is assumed that phase changes are rapid in relation to the characteristic times typical of the problems analysed. Therefore, they can be considered to be in local equilibrium, giving rise to a set of equilibrium restrictions that must be satisfied at all times. Equilibrium restrictions are given below for the concentration of water vapour in gas phase and for the concentration of dissolved air in liquid phase.

The vapour concentration in the gaseous phase is governed by the psychometric (Kelvin's) law, that can be expressed as:

$$\theta_g^w = \left(\theta_g^w\right)^0 \exp\left(\frac{\Psi M_w}{R\left(273.15+T\right)\rho_l}\right) \tag{32}$$

where θ_g^w is the vapour concentration in the gas phase; $(\theta_g^w)^0$ is the vapour concentration in the gas phase in equilibrium with a liquid at flat surface (at the sample temperature). Ψ is the total water potential of the water (excluding gravity terms); M_w is the molecular mass of the water (0.018 kg/mol) and R the gas constant (8.314 J/mol/ºK).

Henry's law is adopted to define the amount of air dissolved in water. This law expresses a linear relationship between the concentration of air in dissolution and the partial pressure of air (P_a) in the gaseous phase:

$$\theta_l^a = \omega_a^l \rho_l = \frac{P_a}{H}\frac{M_a}{M_w}\rho_l \tag{33}$$

where M_a is the molecular mass of the air (0.02895 kg/mol), and H is Henry's constant (1000 MPa).

2.1.4. Phase physical properties

The properties of the fluid phase appear in the balance equations and in the constitutive laws. In general, they depend on the composition of the phase and on the state variables (temperatures and pressures).

The function of density for the liquid phase can be expressed as (i.e. Olivella, 1995 and Gens & Olivella, 2001):

$$\rho_l = 1002.6 \exp\left(4.5x10^{-4}\left(P_l - 0.1\right) - 3.4x10^{-4}T\right) \tag{34}$$

where T is expressed in ºC, P_l in MPa and in ρ_l kg/m^3. This expression must have a cut-off for large negative liquid pressures; if not, unrealistic low liquid density is obtained.

The air density is obtained from the law of ideal gases:

$$\theta_g^a = \frac{M_a P_a}{R\left(273.15 + T\right)} \tag{35}$$

The density of the gas phase is obtained adding the partial densities of the two species:

$$\rho_g = \theta_g^w + \theta_g^a \tag{36}$$

Finally, the viscosity of the liquid and gas phase are, respectively (i.e. Olivella, 1995):

$$\mu_l = 2.1x10^{-12} \exp\left(\frac{1808.5}{273.15 + T}\right) \tag{37}$$

$$\mu_g = 1.48x10^{-12} \exp\left(\frac{\left(273.15 + T\right)^{1/2}}{1 + \frac{119}{\left(273.15 + T\right)}}\right) \tag{38}$$

where T is expressed in ºC and μ_α in MPa.s.

.2.2 Modified formulations

This section presents the extension of the conventional THM formulation described above to include other phenomena not considered in the original framework. The aim is to explore the hypothetical influence of these phenomena on the evolution of the tests modelled, especially on the longer term predictions.

As noted earlier, three phenomena have been considered:

- Non-Darcy flow
- Thermo-osmosis
- Evolution of micro-fabric

2.2.1 Non-Darcy flow

This Section considers the possible effect of a limit of applicability of the Darcy's law at low hydraulic gradients. Some experimental evidence shows that under low hydraulic gradients (J), Darcy's simple relationship does not govern the liquid flow in some porous media, especially in soils containing active clay minerals. Arguments based on the strong clay-water interactions have been suggested to explain this non-Darcy flow behaviour (*i.e.* Bear, 1972).

There are several models for the description of this phenomenon. A well-known law considers two characteristic gradients (Figure 10): the threshold hydraulic gradient (J_o) and the critical

hydraulic gradient (J_c). J_o is the hydraulic gradient below which no flow occurs. J_c is the hydraulic gradient below which flow occurs but it does not fully follow Darcy's law. If the hydraulic gradient is higher than J_c, Darcy's law applies in an incremental form.

A certain amount of experimental work can be found in the literature aimed to explore the validity of the Darcy's law under low gradient in saturated conditions (i.e. Hansbo, 1960; Russell & Swartzendruber, 1971; Dixon et al., 1992). A threshold gradient close to 50 has been reported in some of these works. This deviation from the Darcy's law is sometimes explained considering the high energy of the adsorbed water (Dixon et al., 1992; Cui et al., 2001) and also the pore clogging effect when active clays are present in the porous media (Russell & Swartzendruber, 1971; Cui et al., 2001). On the other hand, Cui et al. (2001) detected higher values of critical gradient, close to 7500, in a pressure reduction path for a mixture of sodium bentonite and sand.

When low permeability clays are tested, the main problem is the long time required by the experiments. A widespread experimental technique to overcome these problems is the application of large hydraulic gradients. A drawback of this practice is that the applied hydraulic gradients are very far from those operating in actual conditions, especially at long times. So, the experimental results obtained may not be immediately applicable in some cases. Figure 11 presents a summary of reported hydraulic gradients used in the testing of low permeability soils. Figure 12 shows the applied hydraulic gradient and the measured hydraulic permeability of the FEBEX bentonite. The figure presents the results obtained for values of bentonite dry density between 1.74 and 1.55 Mg/m^3 (FEBEX II Report, 2004).

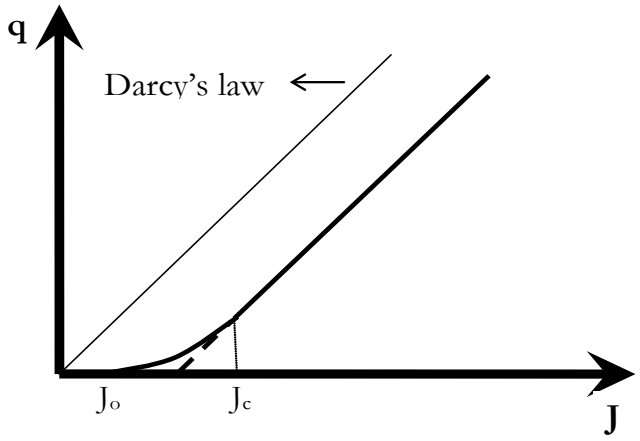

Figure 10. Schematic representation of the non-Darcy low for liquid flow (Dixon et al., 1992).

From the formulation point of view, the only change required to account for this phenomenon is the modification of the flow equation as:

$$\mathbf{q}_l = -\mathbf{K}_l\left(\nabla P_l - \rho_l \mathbf{g}\right) = -\frac{\mathbf{k}}{\mu_l}\left\langle \frac{J - J_o}{J} \right\rangle^{n_t} \left(\nabla P_l - \rho_l \mathbf{g}\right) \tag{39}$$

and

$$\mathbf{J} = \nabla\left(\frac{p}{\gamma_l} + z\right) \quad \text{and} \quad J = \left|\mathbf{J}\right| \tag{40}$$

where J_o is the threshold gradient and n_t is a parameter that controls the value of the critical gradient J_c.

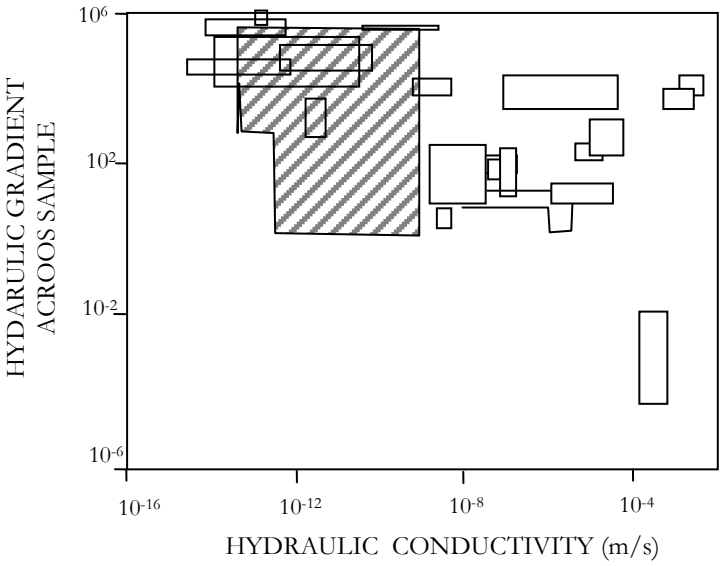

Figure 11. Range of hydraulic conductivities and hydraulic gradients reported in the literature, Dixon et al. (1999). The shaded area indicates the data obtained by Dixon et al. (1999). The other data were collected by Neuzil et al. (1986).

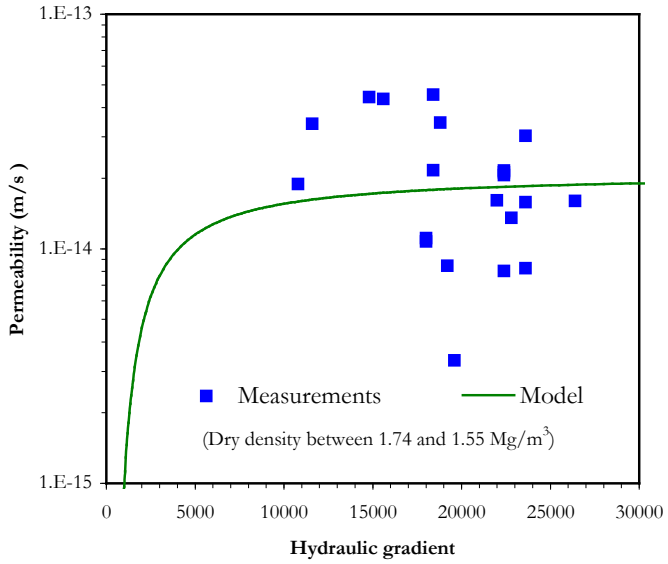

Figure 12. Experimental hydraulic gradient *vs.* saturated permeability (FEBEX II Report, 2004) and adopted flow model.

2.2.2 Thermo-Osmosis

The hydraulic gradient is generally the main force controlling the movement of water in the soils. It is, however, not the only one. Figure 13 presents the different kinds of flow (apart from the electrical flow) that can occur in the porous media and the corresponding gradient responsible for the movements. The word 'law' is used for the diagonal terms associated to the direct flow phenomena, and the name 'effect' is reserved for the non-diagonal ones, called

'coupled processes' (i.e. Bear, 1972; Mitchell, 1993). The Figure also includes the names given to some of these non-diagonal flows.

The 'phenomenological coefficient' that links each flow with the corresponding driving force must be measured experimentally (Mitchell, 1993). Generally, the non-diagonal coefficients are relatively small and negligible compared to the diagonal terms and coupled processes can be ignored. However there are certain problems in which, due to their particular conditions, the coupled process may play a more influential role.

In constant temperature heating tests, a constant thermo-osmotic liquid flow associated with the thermal gradient may exist. In contrast, the hydraulic gradient is very high at the beginning of the test, but diminishes with the hydration of the barrier. The liquid flows associated to these two gradients have opposite directions. Generally, the advective flow due to the pressure gradients (Darcy's law) is the dominant flow. However, at advanced stages of the tests (when the hydraulic gradient becomes smaller), it is possible that the flow of liquid due to the coupled process (thermo-osmotic flow) could have a noticeable effect on the behaviour of the experiment causing a tendency to slow down the hydration in the hot zones close to the heaters.

Flow	Gradients		
	Hydraulic Head	**Chemical Concentration**	**Temperature**
Fluid	**Darcy's Law** (Hydraulic Conduction)	**Chemical Osmosis**	**Thermo Osmosis**
Solutes	**Ultra Filtration**	**Fick's Law** (Diffusion)	**Soret Effect** (Thermal Diffusion)
Heat	**Thermo Filtration** (Isothermal Heat Transfer)	**Dufour Effect**	**Fourier's Law** (Thermal Conduction)

Figure 13. Direct and coupled flow processes

The magnitude of this effect will depend on the ratio between the gradients of the two mechanisms and on the relationship between the phenomenological coefficients associated to either flow. Figure 14 presents a schematic representation of these conditions. To account for thermo-osmosis, a new term has to be added to the equation for liquid flow:

$$\mathbf{q}_l = -\mathbf{K}_l \left(\nabla P_l - \rho_l \mathbf{g} \right) - \mathbf{K}_{HT} \nabla T \qquad (41)$$

where $\mathbf{K}_{HT}$ is the thermo-osmotic coefficient.

Unfortunately, experimental evidence on the value of the thermo-osmotic coefficient is scarce or altogether lacking. Values falling in the very wide range of 10^{-10}-10^{-14} $m^2/K/s$ have been reported in the literature (Soler, 1999, 2001; Djeran, 1993). For the FEBEX bentonite there are no experimental data. The values of the thermo-osmotic constant adopted in the analyses, 5.60 10^{-12} $m^2/K/s$ and 2.73 10^{-13} $m^2/K/s$, fall within the range of possible values reported.

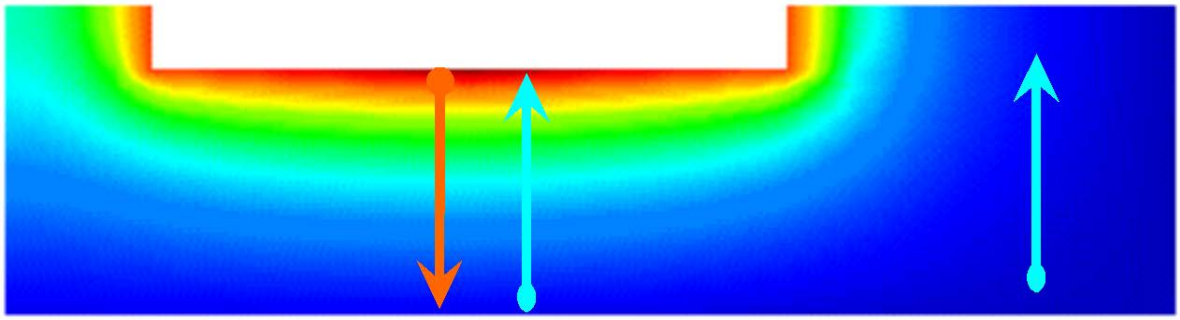

Figure 14. Schematic representation of the conditions related to the advective flow and thermo-osmotic flow in the mock-up test.

2.2.3. Micro-fabric evolution

As explained in Section 2.1.2.3.2, the fabric of the compacted clay consists of dense aggregates of clay particles with intra-aggregate pores (micropores) between them. The arrangement of these clay aggregates conforms a granular skeleton of the material with interaggregate pores (macropores) between them. Once hydration starts, the clay aggregates tend to adsorb water and swell. Due to the confinement conditions of the tests (constant volume conditions practically prevail), the expansion of the microstructure is made possible by reductions of the macropores. This has a significant influence on the permeability value and hence on the hydration of the bentonite. These phenomena imply a changing clay fabric during wetting, resulting in a strong coupling between the mechanical and the hydraulic problem.

Experimental evidences of this strong hydro-mechanical behaviour can be found in Cui et al. (2001) in which measured values of macroporosity and permeability at different suctions are reported (Figure 15). Assuming that the water flow takes place predominately through the macropores, it is possible to suggest that changes in macroporosity could lead to a reduction in the permeability at advanced stages of hydration.

A quite simple approach to take this phenomenon into account is based on the double structure model presented in Section 2.1.2.3.2. It is assumed that the flow of liquid water takes place mainly through the macropores. Although in the proposed double structure approach it is possible to consider also that the water can flow also through the micro level (pores lower than 0.13 μm, in the case of FEBEX bentonite, Figure 6), this possibility has been disregarded in the analyses reported herein.

Thus, it is assumed that the intrinsic permeability is a function of the macro porosity through the following exponential law:

$$\mathbf{k} = k_0 \exp[b(\phi_M - \phi_{M0})]\mathbf{I} \tag{42}$$

where k_0 is the intrinsic permeability at the reference macroporosity ϕ_{M0}, ϕ_M is the macroporosity, and b is a model parameter. The exponential law is just considered as a convenient approximation. It is important to note that in the double structure framework, the evolution of the clay fabric (macro and microporosity) is controlled by the changes in the main variables of the problem (displacements, temperature and macro and micro suctions), which are considered in a fully coupled way. In this way, the main phenomena that affect the changes in both pores levels, and their mutual interactions, are taken into account. The limit condition of this permeability model corresponds to the saturated state.

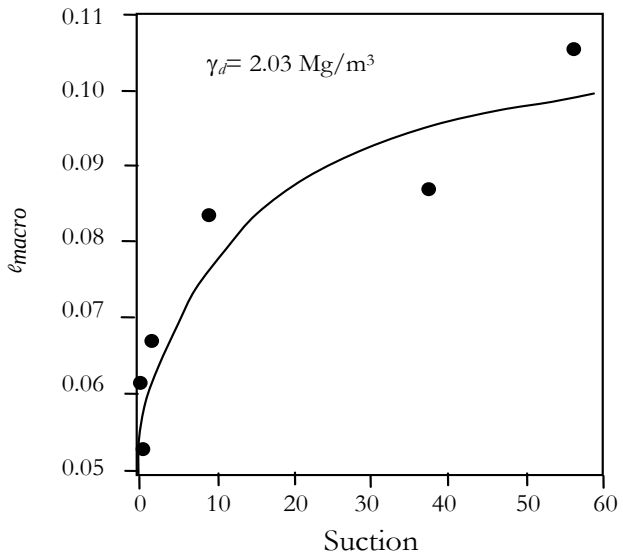

Figure 15. Variation of the macropores void ratio with suction (Cui et al., 2001).

2.3 Computer Code

All the analyses have been carried out using the computer code CODE_BRIGHT (Olivella et al., 1996; CODE_BRIGHT User's Manual, 2014). It is a finite element code designed to solve thermo-hydro-mechanical problems in geological media. One type of unknown (state variable) is associated with each of the balance equations presented. The unknowns are obtained by solving the system of PDE's (Partial Differential Equations) numerically in a coupled way.

The state variables are: solid velocity, **u** (one, two or three spatial directions); liquid pressure, P_l ; gas pressure, P_g ; and temperature T. From state variables, dependent variables are calculated using the constitutive equations or the equilibrium restrictions. Strains are defined in terms of displacements. Small strains and small strain rates are assumed for solid deformation. Additionally, advective terms due to solid displacement are neglected after the formulation is transformed in terms of material derivatives (i.e. material derivatives are approximated as eulerian time derivatives). The numerical approach can be viewed as divided in two parts: spatial and temporal discretization. Galerkin finite element method is used for the spatial discretization while finite differences are used for the temporal discretization. The discretization in time is linear and an implicit scheme is used. Finally, as the problem presented here is non-linear, the Newton-Raphson method was adopted as iterative scheme.

The numerical code can use a wide library of elements including segments, triangles, quadrilaterals, tetrahedrons, triangular prisms and quadrilateral prisms. Linear interpolation functions and, for some elements, quadratic interpolation functions are adopted. Analytical or numerical integration is used depending on element type. For the mechanical problem, selective integration is used for quadrilateral and quadrilateral prisms (i.e. the volumetric part is integrated with a reduced integration of 1 point).

The program has a scheme for the automatic discretization of time. Reduction of time increment may be caused by excessive variation of unknowns per iteration, by excessive number of iterations to reach convergence or by corrections larger than those in the previous iteration (more details in CODE_BRIGHT User's Manual, 2014). Convergence criteria are established in terms of forces or flows and of state variables. Regarding the boundary conditions of the

mechanical problem, forces and displacement rate can be enforced in any spatial direction and at any node. In the hydraulic problem, mass flow rate of water and dry gas can be prescribed at any node, and liquid/gas pressure can be also enforced at any node. Finally, regarding the thermal problem, heat flow and temperature can be prescribed at any node of the mesh (Olivella et al., 1996; CODE_BRIGHT User's Manual, 2014).

3. INFILTRATION TESTS IN CELLS

The infiltration tests were carried out at CIEMAT laboratories on small cells of different lengths (8 cm, 40 cm and 60 cm) in which the compacted bentonite is subjected simultaneously to hydration under isothermal or thermal gradient (non-isothermal) conditions (Villar et al., 2012). During the test, water intake, relative humidity and temperature have been measured using a series of sensors placed on specific locations along the cells.

This section concerns the description and experimental results of the 40 cm infiltration tests. Specifically, two cells were analysed in this project: i) an isothermal cell and b) a cell with a thermal gradient. The results of the numerical analyses will be compared to the experimental observations.

3.1 Description of the tests

The two infiltration tests were performed by CIEMAT (Villar and Gómez-Espina, 2009; Villar et al., 2008) in cylindrical cells with an internal diameter of 7 cm and an inner length of 40 cm, as shown in Figure 16. These cells were made of Teflon to reduce the lateral heat conduction and also covered with steel semi cylindrical pieces to avoid the deformation of the cell caused by bentonite swelling (Figure 17). Five blocks of FEBEX clay were compacted with a compaction pressure of 30 MPa and piled up inside each cell with their hygroscopic water content of 14 % at an initial dry density of 1.65 Mg/m^3. The two blocks placed at the ends of each cell have a length of 5 cm and the other three in the middle have a length of 10 cm.

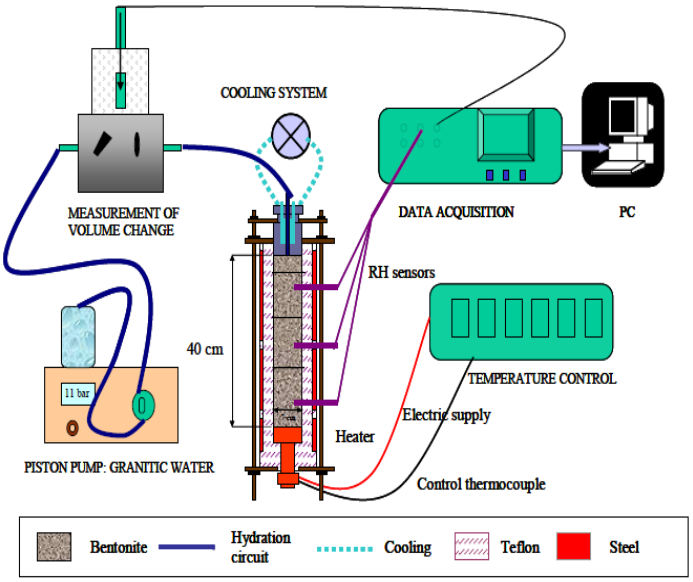

Figure 16. Experimental setup for infiltration tests (Villar and Gómez-Espina, 2009).

The hydration process was initiated by the injection of granitic water through the upper part of the cell at a pressure of 1.2 MPa. This simulates the saturation of the clay barrier due to the water flowing from the host rock. In one of the tests, the non-isothermal test (GT40), the clay was heated through the bottom of the cell at a temperature of 100°C to simulate the heat emission from the nuclear waste. In contrast, in the isothermal test (I40) the bottom of the cell was not heated, so the test was performed at room temperature. The cells were instrumented with sensors placed inside the clay at a spacing of 10 cm (10 cm, 20 cm and 30 cm from the bottom of the cell) to measure temperature and relative humidity. The sensors used are the VAISALA HMP237 that uses the humidity sensor HUMICAP that varies its dielectrical characteristics with small variations in humidity. The temperature was measured with the Pt100

temperature sensing system. In addition to temperature and relative humidity, water intake was measured by electronic volume change measurement systems with a resolution of 0.001 cm^3.

In the modelling performed, it has been assumed that the tests are perfectly tight. As a matter of fact, however, the possibility that some vapour escapes from the cell, especially in the thermal gradient test cannot be totally discarded. Such evaporation would slow down the rate of hydration by an amount that would depend on the amount of leaked vapour. This consideration should be borne in mind when examining the comparison between observation and model computations.

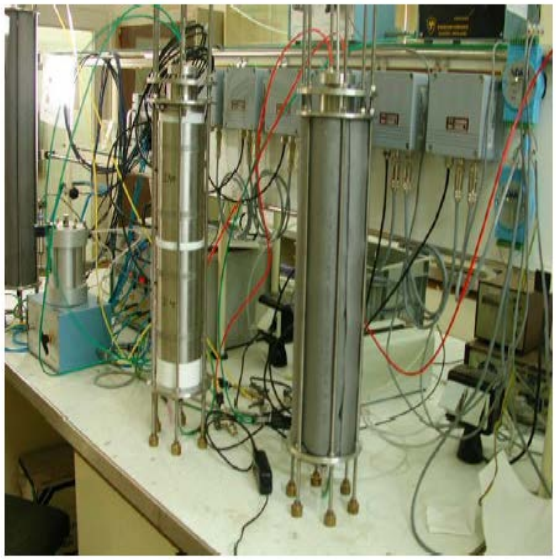

Figure 17. Infiltration cells in operation: isothermal, I40 (left) and thermal gradient, GT40 (right) (Villar and Gómez-Espina, 2009).

3.2 Results of the numerical analyses

Experimental results from independent laboratory tests were used to obtain the parameters of the constitutive models for the thermal, hydraulic and mechanical problems, as described elsewhere (Huertas et al., 2006, Gens et al., 2009, Sanchez et al., 2012). Using those constitutive laws, the infiltration tests were modelled to examine the behaviour of the bentonite cell under isothermal and non-isothermal conditions. The results correspond to temperature and relative humidity measurements made by the sensors located along the cells for a period of practically 10 years (3600 days).

The problem was modelled with a 1D mesh composed of 50 linear elements and 51 nodes. Five cases of numerical simulations were performed: Operational Base Case (OBC), Non-Dracy flow (THG), Thermo-osmosis (THO), Micro-fabric evolution (DS) and Micro-fabric evolution + Thermo-osmosis (DS + THO). Values of temperature, liquid pressure and displacements were obtained directly from the program. The values of relative humidity were computed by means of the psychometric law based on the computed values of temperature, fluid pressures and phase properties.

3.2.1 Operational Base Case (OBC)

The Operational Base Case (OBC) was based on the conventional formulation and the Barcelona Basic Model (BBM). For this case, the model parameters introduced in Section 2.1 were adopted for the mechanical, thermal and hydraulic problems.

The numerical results for the I40 test are presented in the following figures. Figure 18 shows the measurements of temperature along the cell during the test for a period of 3600 days. According to this plot, values between 18°C and 32°C were recorded due to the seasonal temperature changes during the year. The model is set to a constant temperature of 23°C (solid line) along the entire cell.

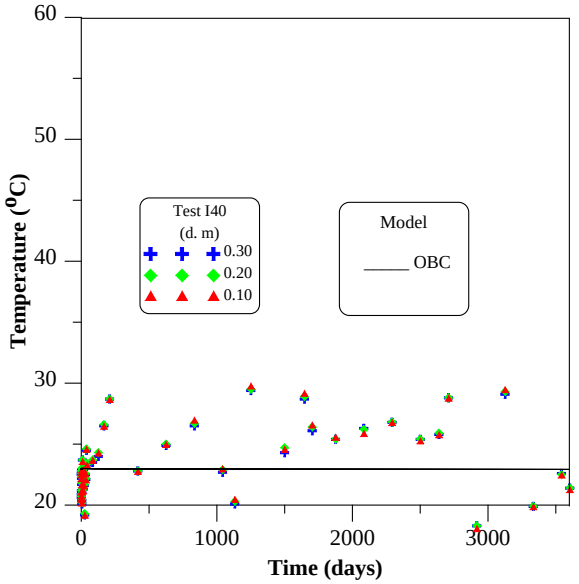

Figure 18. Evolution of Temperature for the I40 test: Experimental Data (scatter points) and Model Predictions (OBC) up to 3600 days (10 years) at 0.30 m, 0.20 m and 0.10 m from the bottom of the cell.

Hydration is performed with a liquid pressure of 1.2 MPa applied at the top of the sample. Figure 19 shows the data related to the relative humidity for the same three locations where the temperature was measured. The first thing to be observed from the experimental data is a monotonic increase in relative humidity with time in all the positions. This means that hydration is taking place and the water is moving from one end to the other driven by hydraulic gradient. However, the relative humidity is increasing at a different rate in each location. The sensor closest to the top (hydration source), is the one showing a higher rate of hydration in the measurements. Moving further away from the hydration source, this rate is naturally reduced. It is also noted that a fully saturated condition is not achieved at any location of the cell. The sensor closest to the upper end measured a maximum value close to 93% relative humidity, the one in the middle 92% and the one near the bottom end 88%. Regarding the numerical results for this test, it can be seen that the model reproduced the general trend of the measurements but does not show an especially good agreement with the experimental values.

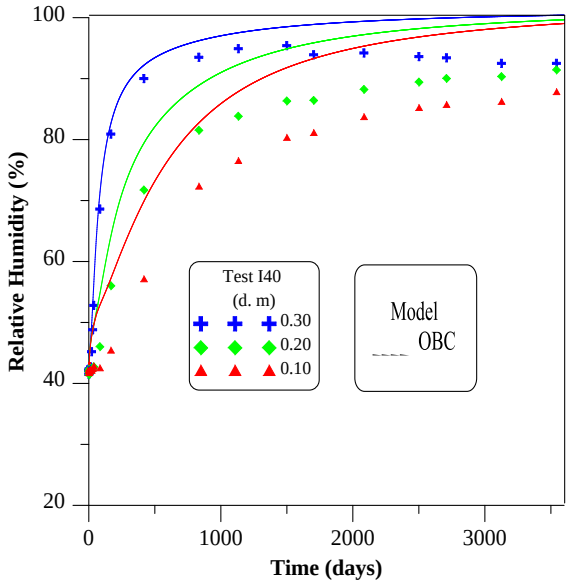

Figure 19. Evolution of Relative Humidity for the I40 test: Experimental Data (scatter points) and Model Predictions (OBC) up to 3600 days (10 years) at 0.30 m, 0.20 m and 0.10 m from the bottom of the cell.

The OBC predicts practically fully saturation at the top of the cell after 3000 days approximately. In the middle of the cell (0.20 m), there is also an increase in relative humidity with time but at a lower rate. Here the model predicts a value of around 99% of relative humidity at 10 years, extremely close to saturation. The bottom part of the cell (0.30 m) shows a very similar behaviour, increasing the relative humidity with time but at a lower rate than the other two positions. In this location, the predicted value of relative humidity after 10 years is close to 98%. In the long term, the model predicts values of 100% of relative humidity at the throughout the cell (Figure 20).

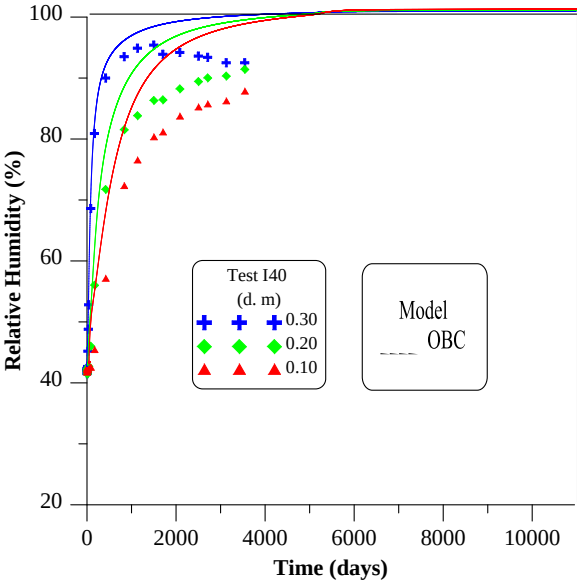

Figure 20. Evolution of Relative Humidity for the I40 test: Experimental Data (scatter points) and Model Predictions (OBC) up to 10950 days (30 years) at 0.30 m, 0.20 m and 0.10 m from the bottom of the cell.

Comparing the experimental values with the predicted ones, it is evident that there has been an overestimation of relative humidity by the model in all the sensors; the numerical simulations predict higher hydration rates than the real ones.

Figure 21 presents the experimental values and model predictions of temperature for the GT40 test. As indicated previously, in addition to the hydration from the upper part of the cell, this test is heated at a temperature of 100°C at the bottom end. Because of the difference in temperature between both ends, there is a thermal gradient along the specimen. Average temperatures close to 51°C were recorded by the sensor closest to the heater (0.10 m) while values around the 29°C were measured close to the hydration source (0.30 m). In the middle of the cell (0.20 m), an average intermediate value of 36°C was measured.

In general terms, the model captures satisfactorily the average measured temperatures for each position. It can also be observed that there is a slightly increase of the predicted temperature values with time in all the sensors due to the variation of thermal conductivity associated with the progress of hydration. The predicted long-term evolution of the temperature is shown in Figure 22.

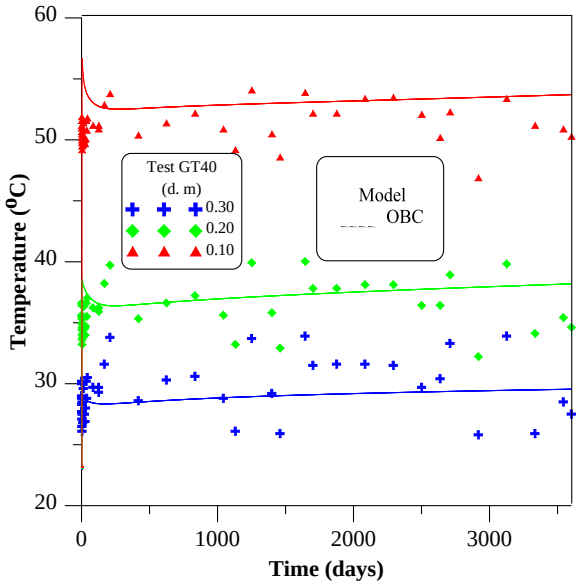

Figure 21. Evolution of Temperature for the GT40 test: Experimental Data (scatter points) and Model Predictions (OBC) up to 3600 days (10 years) at 0.30 m, 0.20 m and 0.10 m from the bottom of the cell.

The experimental data and numerical results of relative humidity for the GT40 test are shown in Figure 23. Examining the measurements, it is observed that the evolution depends strongly of the measurement location.

The data recorded by the sensor located near the top of the cell (0.30 m), has a similar pattern to the one observed in the I40 test. However, the hydration rate is lower than the one observed in the isothermal test. Also, a fully saturated condition is not achieved in this position as the sensor registered a maximum value of 93% at the end of the test. In the mid-section of the cell (0.20 m), an increase in the values of relative humidity is also observed but developing at a lower rate. A value of 80% was measured close to the end of the test, implying that the cell in this location remained unsaturated. The location closest to the heater shows a very characteristic behaviour. In the first 300 hours (approximately 12 days) of the test, the sensor (0.10 m) captured an increase in the measured values. In the following days, the measurements started to decrease to a value around 35% relative humidity. This drop is due to the drying of the clay close to the heat source. At later times, the overall hydration process causes a small increase in relative humidity; a maximum value of relative humidity of 43% was recorded. This implies that under these conditions, it is expected that the bentonite will likely remain unsaturated for a long time.

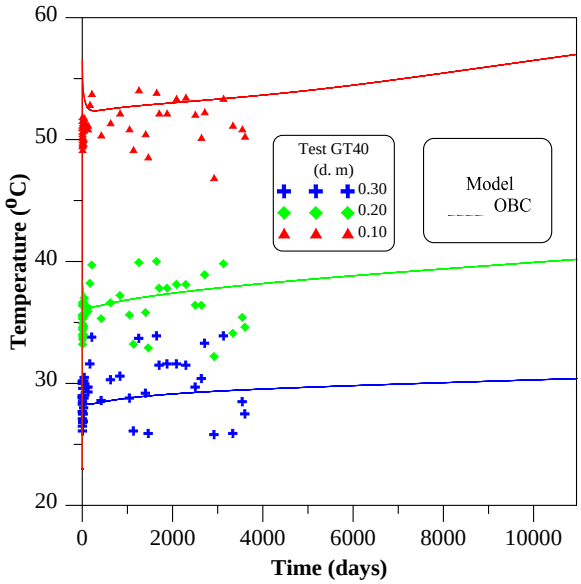

Figure 22. Evolution of Temperature for the GT40 test: Experimental Data (scatter points) and Model Predictions (OBC) up to 10950 days (30 years) at 0.30 m, 0.20 m and 0.10 m from the bottom of the cell.

The numerical results of relative humidity for this test, based on the OBC model, do not show the same evolution as the experimental data points. At the top of the cell (0.30 m), the model seems to capture the tendency of the measurements at the beginning of the test. However, after some time (around 300 days), the model overpredicts the hydration rate in this part of the cell. By the end of the test, as in the I40 test, the model shows a value of 100% of relative humidity. In the centre of the cell (0.20 m), the simulation shows also an overprediction of the experimental values. The maximum value of relative humidity at the end of the test predicted by the model was around 99%. Finally, for the section closer to the heat source (0.10 m), the curve seems to have the same qualitative shape as the data points, but it can be observed an even higher overestimation of hydration by the model; predicting a final value of 89% relative humidity. In the long term, the model predicts a fully saturated condition after aboit 8000 days (i.e. 22 years) as shown in Figure 24. The experimental results suggest strongly and this is a gross underestimation of the saturation time.

In general terms, it is possible to state that the OBC model was not able to explain satisfactorily the behaviour observed in the infiltration tests. In all the locations, the model overestimated the relative humidity observations by predicting a faster hydration rate. In an effort to achieve a better agreement, other alternative cases are presented in the following sections.

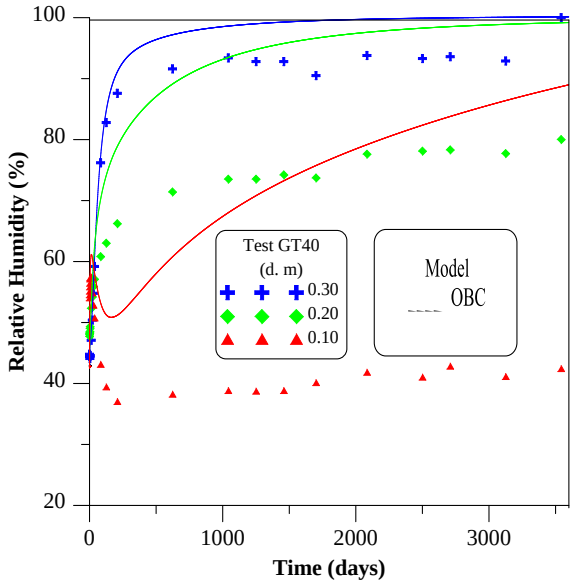

Figure 23. Evolution of Relative Humidity for the GT40 test: Experimental Data (scatter points) and Model Predictions (OBC) up to 3600 days (10 years) at 0.30 m, 0.20 m and 0.10 m from the bottom of the cell.

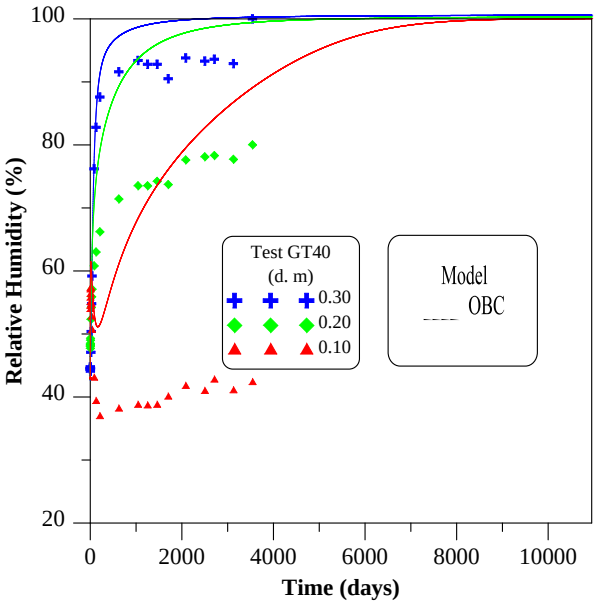

Figure 24. Evolution of Relative Humidity for the GT40 test: Experimental Data (scatter points) and Model Predictions (OBC) up to 10950 days (30 years) at 0.30 m, 0.20 m and 0.10 m from the bottom of the cell.

3.2.2 Non-Darcy Flow Case (THG)

In the numerical analysis considering non-Darcy flow (THG) the general, mechanical and thermal parameters are the same as the ones in the OBC. However, the non-Darcy formulation for liquid flow described in 2.2.1 is adopted with the parameters shown in Table 3. As Figure 12 illustrates, the values adopted are consistent with the experimental evidence (Villar and Gómez-Espina, 2009).

Table 3. Parameters used in in the non-Darcy law for liquid flow to simulate the isothermal infiltration test.

Parameter	**Value**
J_0	5
Power law coefficient	180

A graphical representation of this law with the Darcy's relationship for comparison is shown in Figure 25.

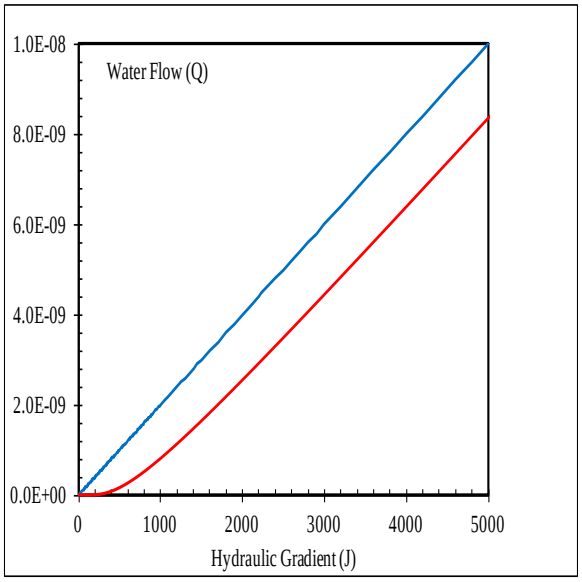

Figure 25. Graphical representation of Darcy's law (blue line) and non-Darcy law (red line) used during the numerical analysis for the isothermal infiltration test.

Figure 26 presents the experimental measurements of relative humidity in the I40 test along with the numerical results obtained from the THG and OBC analyses. The values predicted by the THG in all the positions are quite lower than the measured ones. Maximum relative humidity values of 87%, 80% and 76% were predicted by the model for the sensors located at 0.30 m, 0.20 m and 0.10 m from the bottom of the cell respectively. In the long term, the model estimates a small increase in these values but does not yet predict a fully saturated condition after 30 years of hydration, as Figure 27 shows.

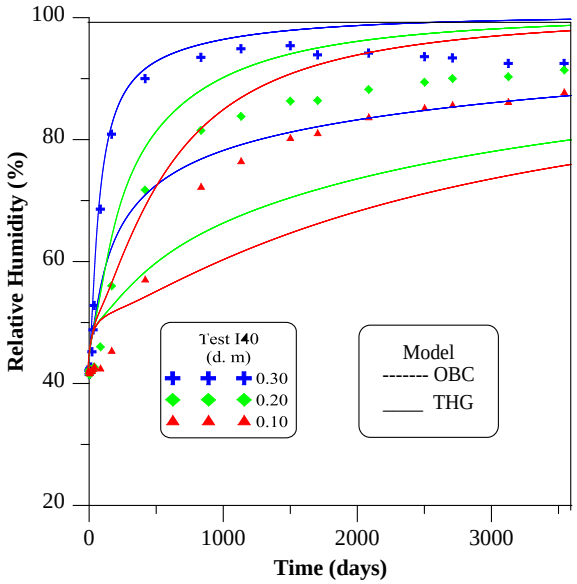

Figure 26. Evolution of Relative Humidity for the I40 Test: Experimental Data (scatter points) and Model Predictions up to 3600 days (10 years) for the (THG) and (OBC) cases at 0.30 m, 0.20 m and 0.10 m from the bottom of the cell.

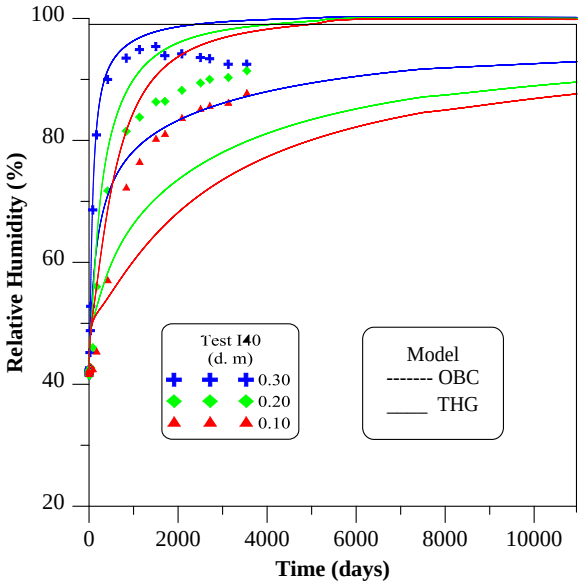

Figure 27. Evolution of Relative Humidity for the I40 Test: Experimental Data (scatter points) and Model Predictions up to 10950 days (30 years) for the (THG) and (OBC) cases at 0.30 m, 0.20 m and 0.10 m from the bottom of the cell.

The same formulaiton was used to simulate the GT40 test. However, when the parameters of Table 3 were used, the model didn't manage to predict correctly the slowdown in the hydration rate observed in the GT40 cells. Because of this, a different set of parameters was determined, by backcalculation, to reproduce better the observed experimental results (Table 4). A graphical representation of the non-Darcy and Darcy's laws is presented in Figure 28. Comparing the parameters in Table 4 with the ones used in the I40 test (i.e. Table 3), it can be seen that the power law coefficient is still the same but the threshold hydraulic gradient has been increased by a factor of 10.

Table 4. Parameters used in the non-Darcy law for liquid flow to simulate the non-isothermal infiltration test.

Parameter	**Value**
J_0	50
Power law coefficient	180

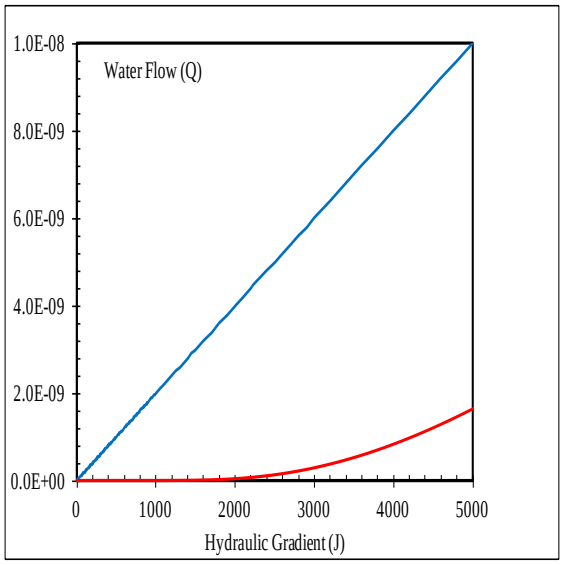

Figure 28. Graphical representation of Darcy's law (blue line) and non-Darcy law (red line) used during the numerical analysis for the isothermal infiltration test.

The next two figures present the measured and predicted values of temperature for the thermal test (GT40). Figure 29 shows a good agreement between the experimental and numerical results. It is also noted that the predicted values of temperature remained constant in the long term, as Figure 30 shows reflecting the very slow progress of hydration.

The experimental and numerical results of relative humidity are displayed in Figure 31. According to this figure, it can be observed that the model THG capture fairly satisfactorily the trend of the data points in some of the positions. For the position closer to the top of the cell (0.30 m), the curve generated by the model shows a shape similar to the one observed in the data points. However, the measured values are being underestimated. A maximum value of 89% of relative humidity at the end of the test was predicted.

In the centre of the cell (0.20 m), in the first 250 days, the model showed a higher rate of hydration than the experimental points leading to an over estimation of the measured values. After that, the rate of hydration decreased and at the end of the test a value of 68% of relative humidity was reported. For the location closest to the heater (0.10 m), the numerical results obtained were very close to the data points in a range of time between the 1000 days and the end of the test, where a value of 39% was reached. In the long term, it appears that steady sate conditions are achieved with no tendency observed towards full hydration of the bentonite (Figure 32).

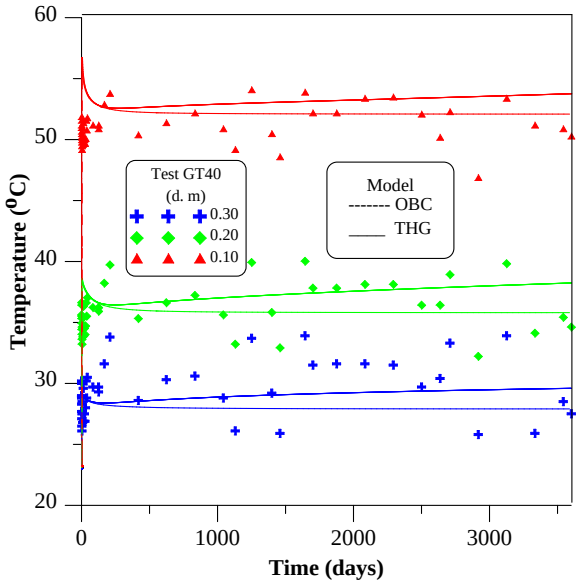

Figure 29. Evolution of Temperature for the GT40 Test: Experimental Data (scatter points) and Model Predictions up to 3600 days (10 years) for the (THG) and (OBC) cases at 0.30 m, 0.20 m and 0.10 m from the bottom of the cell.

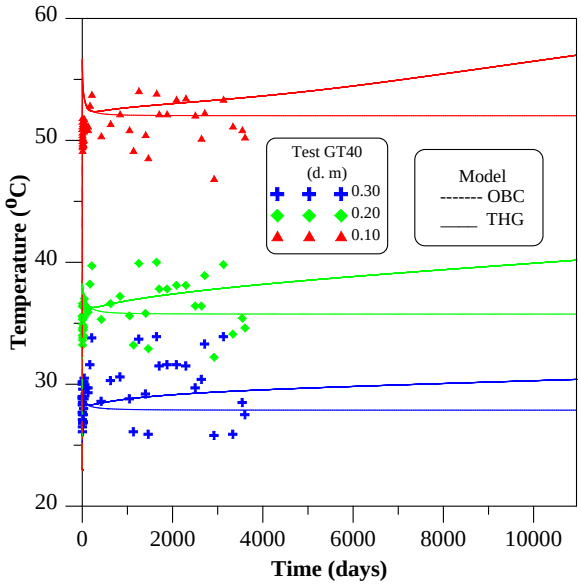

Figure 30. Evolution of Temperature for the GT40 Test: Experimental Data (scatter points) and Model Predictions up to 10950 days (30 years) for the (THG) and (OBC) cases at 0.30 m, 0.20 m and 0.10 m from the bottom of the cell.

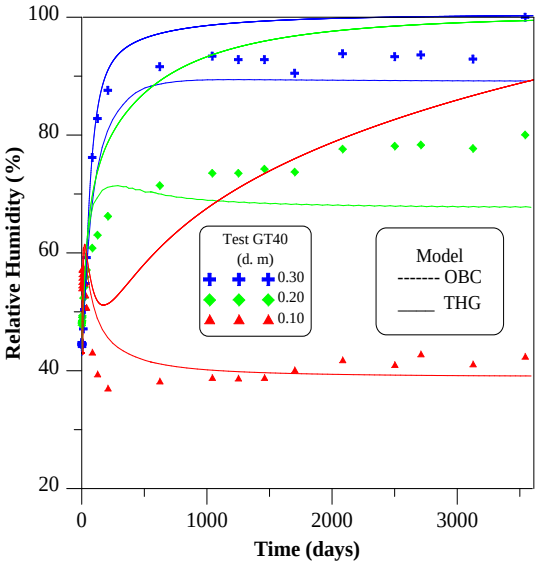

Figure 31. Evolution of Relative Humidity for the GT40 Test: Experimental Data (scatter points) and Model Predictions up to 3600 days (10 years) for the (THG) and (OBC) cases at 0.30 m, 0.20 m and 0.10 m from the bottom of the cell.

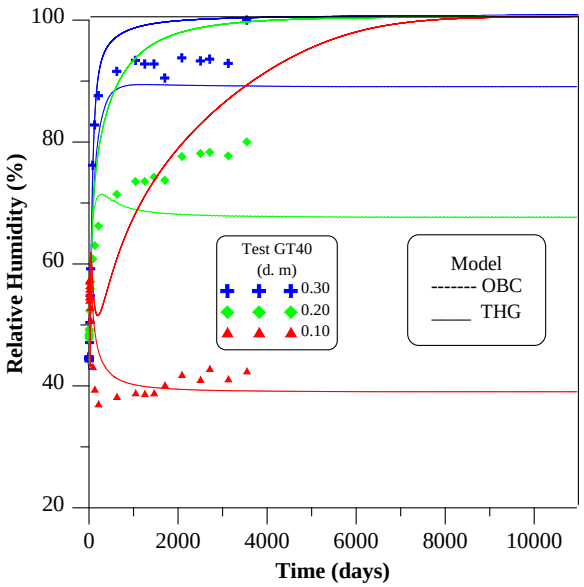

Figure 32. Evolution of Relative Humidity for the GT40 Test: Experimental Data (scatter points) and Model Predictions up to 10950 days (30 years) for the (THG) and (OBC) cases at 0.30 m, 0.20 m and 0.10 m from the bottom of the cell.

In summary, there was an improvement in the numerical predictions of temperature and, especially, relative humidity. The incorporation in the modelling of the threshold hydraulic gradient and a power law for permeability at low gradients allowed a better reproduction of the hydration rate in the bentonite. However, there is still a significant difference between the measured and predicted values like the under estimation of hydration observed in the isothermal test and the steady state condition obtained by the model in the non-isothermal case. The fact that different parameters have been required in the two cases indicates that either the threshold value depends on temperature or, more likely, that the non-Darcy flow law on its own is unable to explain the full set of observations.

3.2.3. Thermo-Osmosis Case (THO)

The thermo-osmosis phenomenon is related to the movement of water induce by temperature gradients. It is clear that this phenomenon will have no influence in the isothermal case (I40 test) due to absence of thermal gradient (Figure 33). This is borne out by the comparison of the numerical results obtained of the THO and the OBC analyses; as expected, they are practically identical.

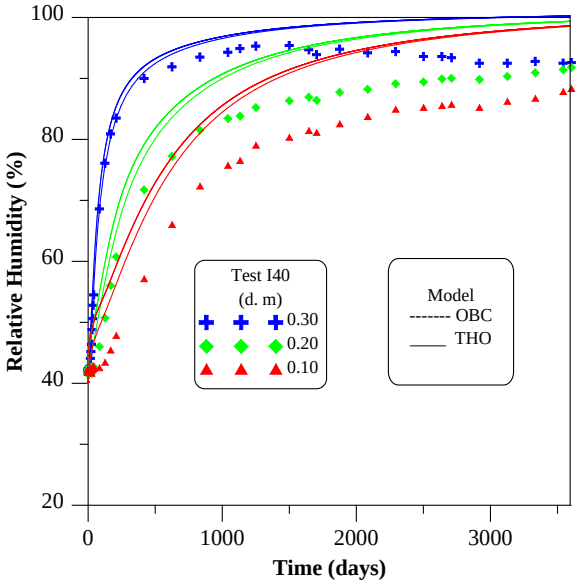

Figure 33. Evolution of Relative Humidity for the I40 Test: Experimental Data (scatter points) and Model Predictions up to 3600 days (10 years) for the (THO) and (OBC) cases at 0.30 m, 0.20 m and 0.10 m from the bottom of the cell.

In the thermal test (GT40), a temperature gradient is present due to the heating at the bottom of the cell. If thermo-osmosis is relevant, the water (as liquid) will move from the top to the bottom of the cell driven by the hydraulic gradient but water will also move from bottom to top in the liquid phase driven by temperature gradient. As indicated above, the thermo-osmotic constant adopted in the numerical analysis is 5.60×10^{-12} $m^2/K/s$ but all the general, mechanical, hydraulic and thermal parameters still the same as those used in the OBC case.

The following figures show the numerical results obtained from the THO and OBC cases together with the experimental data of temperature and relative humidity. Figure 34 shows that the predicted values of temperature given by the model are somewhat lower than the ones given by the OBC, reflecting different computed thermal conductivities in the two analyses. The model also predicts that the temperature will remain constant in the long term (Figure 35).

Figure 36 presents the modelling results for relative humidity in the GT40 test. In general terms, it can be said that the predicted values are closer to the observations and that the behaviour observed inside the cell is reasonably well captured by the model THO. At the upper end of the cell (0.30 m), it is possible to see that during the first days of the test, the measured values are very well reproduced. However, as time increases, a small overestimation can be noted. On the other hand, in the middle of the cell, the values are being over predicted but as time increases, the model results get closer to the experimental values. For the location nearest to the heater, the drying process during the first days of the experiment is well captured by the model. In contrast, the hydration that occurs afterwards has been underestimated. Figure 37 shows the long term predictions of the model indicating that after 30 years, the bentonite will still be unsaturated.

Overall, the inclusion of thermo-osmosis to the analysis appears to improve the performance of the model concerning the reproduction of experimental observations over the time that the test has been running (10 years).

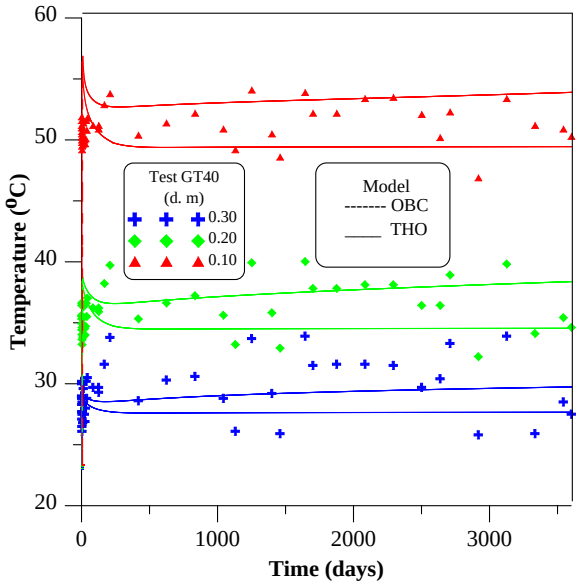

Figure 34. Evolution of Temperature for the GT40 Test: Experimental Data (scatter points) and Model Predictions up to 3600 days (10 years) for the (THO) and (OBC) cases at 0.30 m, 0.20 m and 0.10 m from the bottom of the cell.

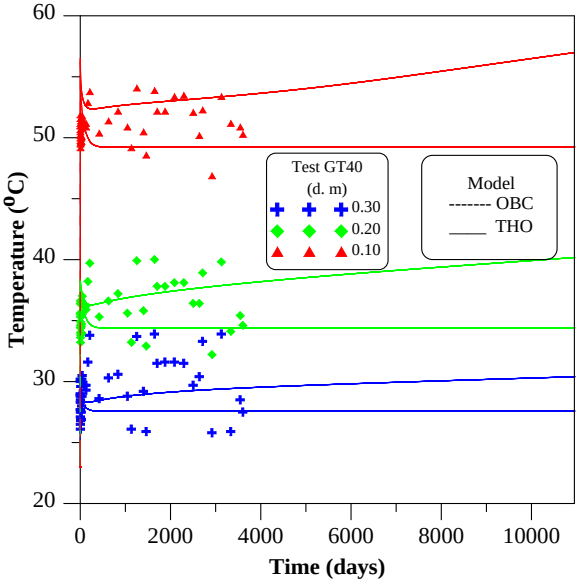

Figure 35. Evolution of Temperature for the GT40 Test: Experimental Data (scatter points) and Model Predictions up to 10950 days (30 years) for the (THO) and (OBC) cases at 0.30 m, 0.20 m and 0.10 m from the bottom of the cell.

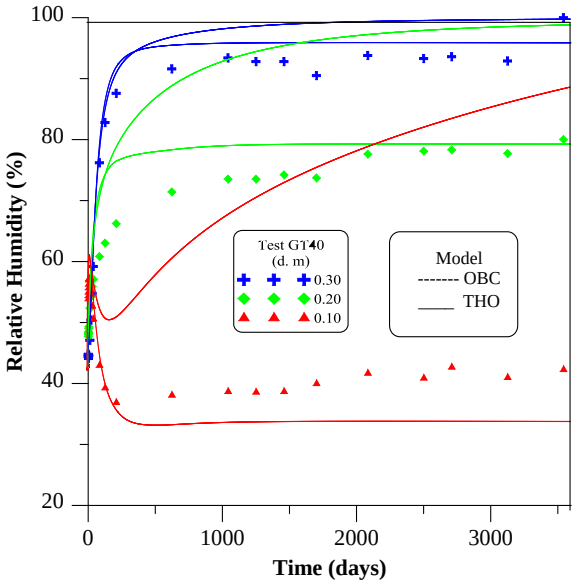

Figure 36. Evolution of Relative Humidity for the GT40 Test: Experimental Data (scatter points) and Model Predictions up to 3600 days (10 years) for the (THO) and (OBC) cases at 0.30 m, 0.20 m and 0.10 m from the bottom of the cell.

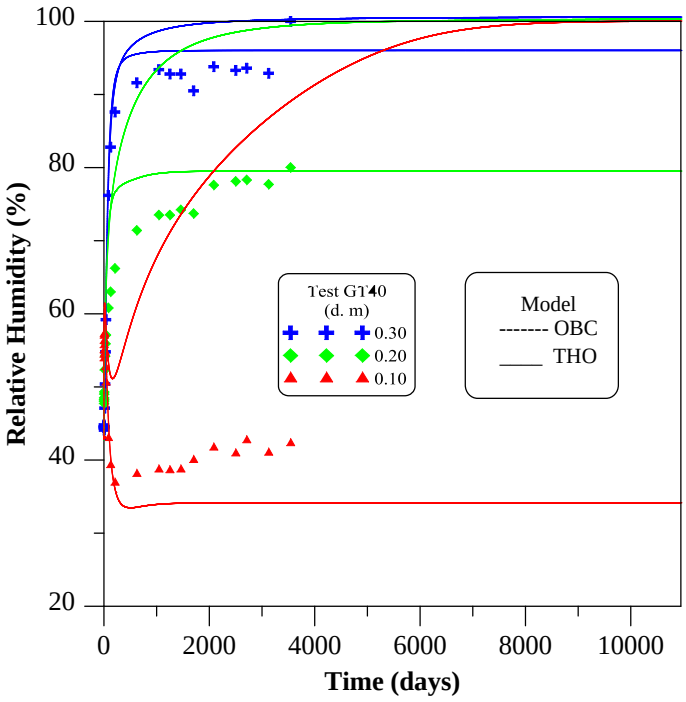

Figure 37. Evolution of Relative Humidity for the GT40 Test: Experimental Data (scatter points) and Model Predictions up to 10950 days (30 years) for the (THO) and (OBC) cases at 0.30 m, 0.20 m and 0.10 m from the bottom of the cell.

3.2.4. Micro-fabric evolution (DS)

The Double Structure (DS) constitutive law is used to perform the numerical analysis in the infiltration tests. As described above, this approach assumes the existence of two basic pore levels: the macropores or inter-aggregate pores (associated with the space between the clay aggregates) and the microstructure of intra-aggregate pores (related to the pore space inside the

clay aggregates). It is assumed that the flow of water takes place mainly through the macropores and, as explained before, intrinsic permeability is assumed to depend only on the porosity of the macrostructural level. The mechanical, thermal and hydraulic parameters used in the analyses are listed in Tables 5, 6, 7 and 8. It is important to highlight that a dry density equivalent to the dry density of bentonite block was (i.e. 1.74 Mg/m^3) used in this analyses, which is somewhat higher than the dry density of the column (i.e. 1.64 Mg/m^3).

Table 5. General parameters used in the DS case to perform the numerical analysis for the 1D infiltration tests.

Parameter	**Value**
ρ_{db} [Mg/m^3]	1.74
w [%]	14.00
G_S	2.72
e_{total}	0.563
e_{micro}	0.450
e_{macro}	0.113
ϕ_{micro}	0.288
ϕ_{macro}	0.072
ϕ_{total}	0.360

Table 6. Mechanical parameters used in the DS case to perform the numerical analysis for the 1D infiltration tests.

Parameter	**Value**	**Parameter**	**Value**
κ_{i0}	0.005	λ_0	0.080
κ_{s0}	0.001	r	0.900
ν	0.400	β [MPa^{-1}]	0.200
α_{ss}	0	ρ_o	0.200
α_{is}	0	k	0.100
α_{sp}	0	p_c [MPa]	0.500
p_{ref} [MPa]	0.010	M	1.00
α_0	$1.00x10^{-05}$	α	0.530
T_{ref} [°C]	20	e_0	0.113
p_0^* [MPa]	6.00		

Table 7. Thermal parameters used in the DS case to perform the numerical analysis for the 1D infiltration tests.

Parameter	**Value**
λ_{dry}	0.47
λ_{wet}	1.15

Table 8. .Hydraulic parameters used in the DS case to perform the numerical analysis for the 1D infiltration tests.

Parameter	**Value**	**Parameter**	**Value**
p_{0d} [MPa]	7	p_{sec} [MPa]	1100
σ_0 [kN/m]	0.072	λ_2	2.1
λ	0.1	K_{xx} [m^2]	$5.00x10^{-20}$
s_{rl}	0	K_{yy} [m^2]	$5.00x10^{-20}$
s_{ls}	1	K_{zz} [m^2]	$5.00x10^{-20}$
p	0	ϕ_0	0.14
d	0	**b**	50
s_d	0		

The following figures show the numerical results obtained using in the DS computation. Figure 38 presents the results of relative humidity for the I40 (isothermal) test. According to this figure, the model can capture the general trend of the measurements with some quantitative differences in the prediction of the real values. If one compares this model against the OBC, it can be seen that the DS model predicts better the hydration rate at the three locations along the cell. Observing the long term predictions (Figure 39), it can be noted that he values of relative humidity keep increasing with time and after 30 years, the bentonite is not totally saturated yet. It should be noted that the parameter *b* in Equation (42) was not independently determined but back-calculated to achieve a good match of the experimental data.

Figure 40 presents the evolution of for the GT40 (thermal gradient) test. Figure 40 shows that model can reproduce quite well the measured values of temperature in the three locations during the duration of the test. At the position close to the top, the model predicted a temperature near to 29°C, same as the average measured value. At the centre of the cell, the temperature obtained by the model was about 38°C versus the 36°C measured by the sensor. For the location near the heater, the simulations recorded a temperature of 54°C while the sensor measured 51°C. In Figure 41 the long term predictions of temperature are shown. The model predicts a slight increase of temperature values for a period of 30 years because hydration now does not stop and thermal conductivity, therefore, changes accordingly.

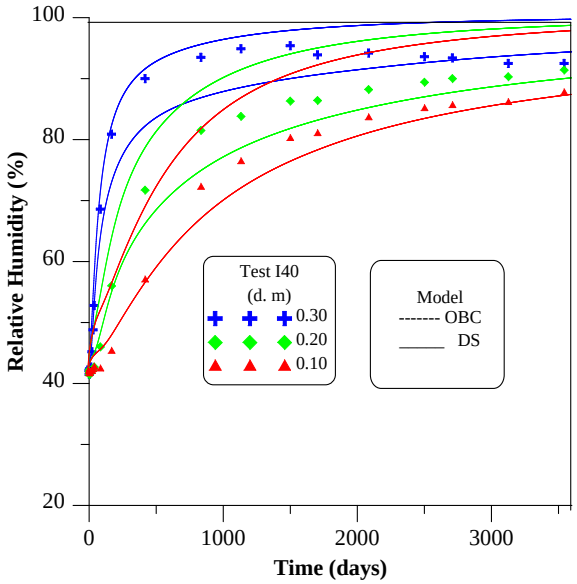

Figure 38 Evolution of Relative Humidity for the I40 Test: Experimental Data (scatter points) and Model Predictions up to 3600 (10 years) for the (DS) and (OBC) cases at 0.30 m, 0.20 m and 0.10 m from the bottom of the cell.

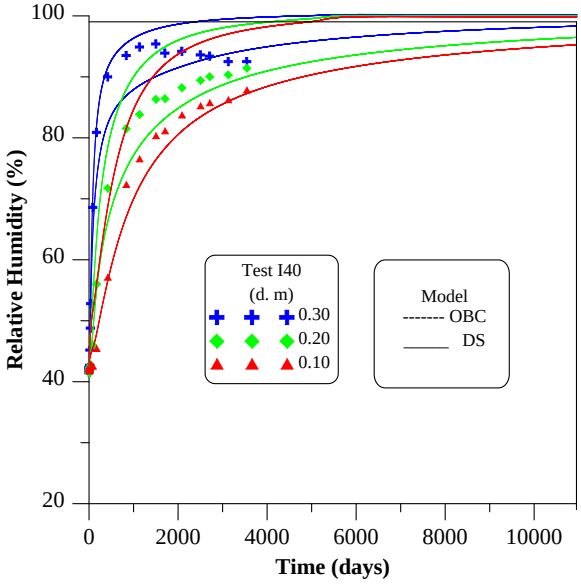

Figure 39. Evolution of Relative Humidity for the I40 Test: Experimental Data (scatter points) and Model Predictions up to 10950 (30 years) for the (DS) and (OBC) cases at 0.30 m, 0.20 m and 0.10 m from the bottom of the cell.

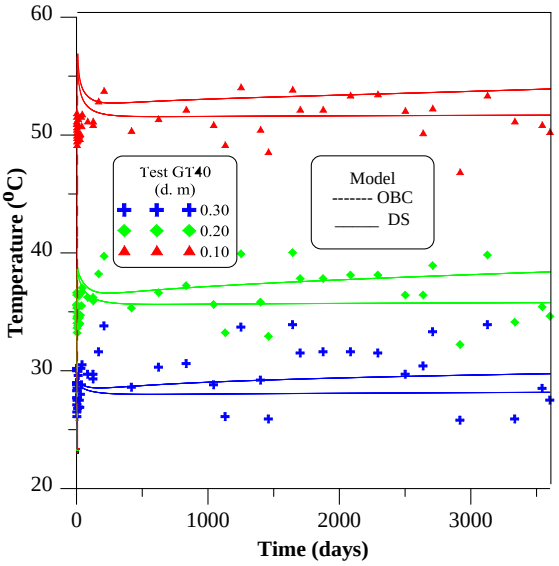

Figure 40. Evolution of Temperature for the GT40 Test: Experimental Data (scatter points) and Model Predictions up to 3600 days (10 years) for the (DS) and (OBC) cases at 0.30 m, 0.20 m and 0.10 m from the bottom of the cell.

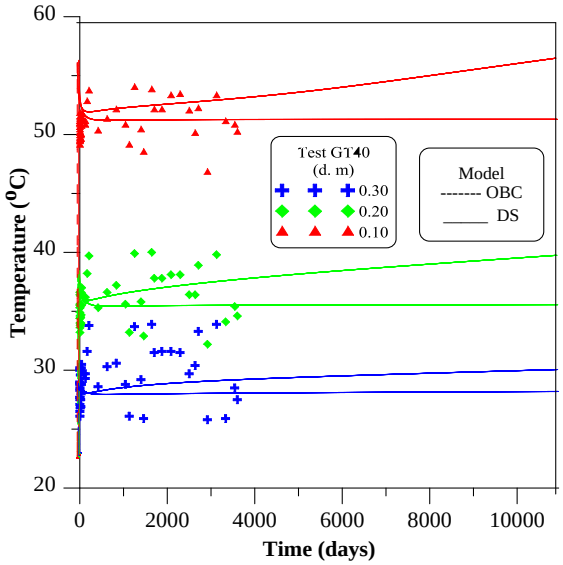

Figure 41. Evolution of Temperature for the GT40 Test: Experimental Data (scatter points) and Model Predictions up to 10950 days (30 years) for the (DS) and (OBC) cases at 0.30 m, 0.20 m and 0.10 m from the bottom of the cell.

Regarding the results of relative humidity (Figure 42), the DS analysis simulated quite well the behaviour observed in the experimental data. The difference between the results of this model and those obtained in the OBC analysis can also be noted. In contrast to the OBC computation, the DS analysis predicts that there will be unsaturated conditions throughout the entire experiment. These conditions will remain in the bentonite for more than 30 years according to the long term model predictions. As Figure 43 shows, only the sensor near to the hydration source will measure 100 % of relative humidity after 30 years. The other two sensors (i.e. the one in the centre of the cell and the other close to the heater), will remain under unsaturated conditions with values around of 88 % and 49 % respectively. These unsaturated conditions are caused by hydro-mechanical coupled phenomena. When hydration progresses, the micropores are filled with water and the bentonite expands. This swelling reduces the size of the pores of the macrostructure and, as a result, permeability (and water flow) reduces strongly.

In addition to the numerical results that can be directly compared to observations, it is also interesting in this case to plot the distributions at different times (up to 10000 days, 27 years) of a number of variables for both the isothermal and non-isothermal case.

Figure 44 shows the distribution of the macro void ratio along the cell for the isothermal case. It can be noted that the macro void ratio decreases as hydration progresses. This implies that the volume of the macro-pores has been reduced and the macro-structure has become denser. This densification in the macro-structure is caused by the swelling behaviour in the microstructure as Figure 45 shows. In this Figure it can be seen that as hydration proceeds, the micro void ratio increases as the result of an expansion in the micro-structural level. This swelling occurring at particle level will partially fill the voids in the macro-structure. Figure 46 shows the distribution of the global void ratio along the cell.

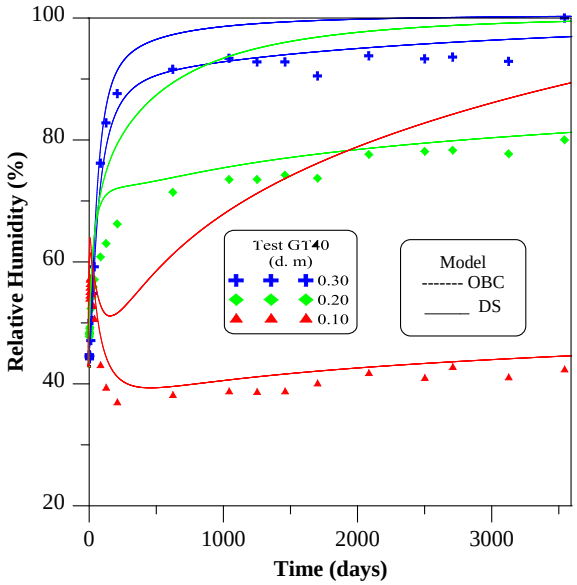

Figure 42. Evolution of Relative Humidity for the GT40 Test: Experimental Data (scatter points) and Model Predictions up to 3600 days (10 years) for the (DS) and (OBC) cases at 0.30 m, 0.20 m and 0.10 m from the bottom of the cell.

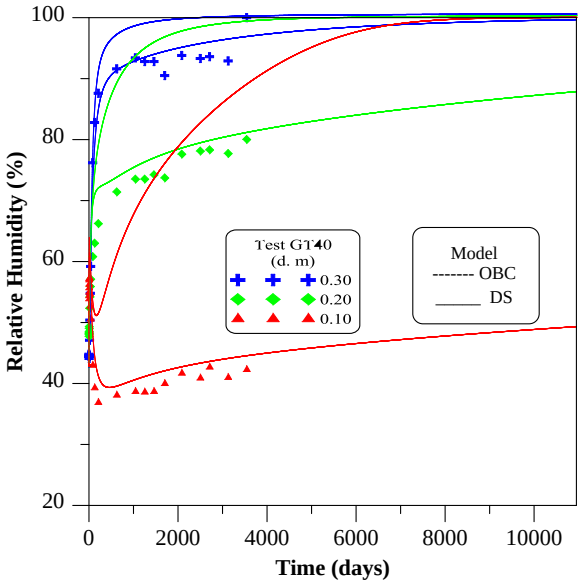

Figure 43. Evolution of Relative Humidity for the GT40 Test: Experimental Data (scatter points) and Model Predictions up to 10950 days (30 years) for the (DS) and (OBC) cases at 0.30 m, 0.20 m and 0.10 m from the bottom of the cell.

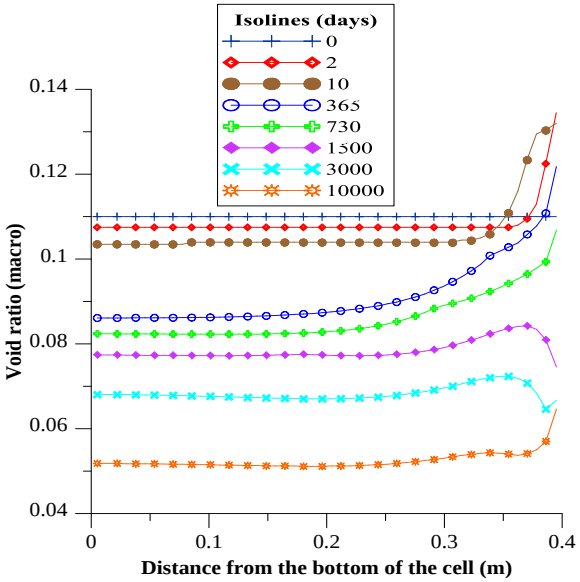

Figure 44. Distribution of macro void ratio along the 40 cm infiltration cell for the isothermal case. Model predictions up to 10000 days.

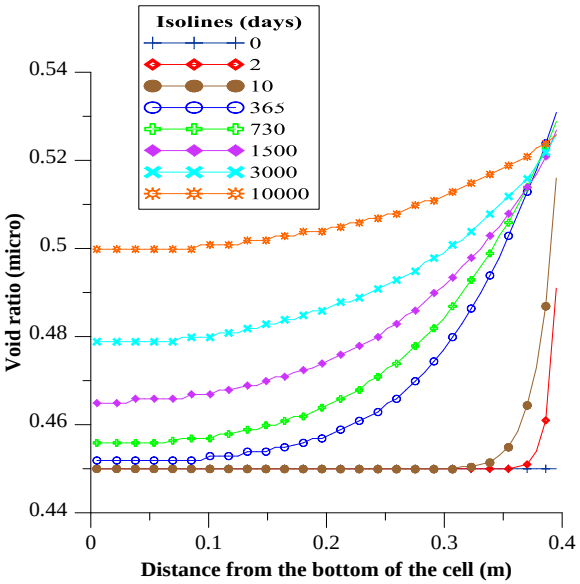

Figure 45. Distribution of micro void ratio along the 40 cm infiltration cell for the isothermal case. Model predictions up to 10000 days.

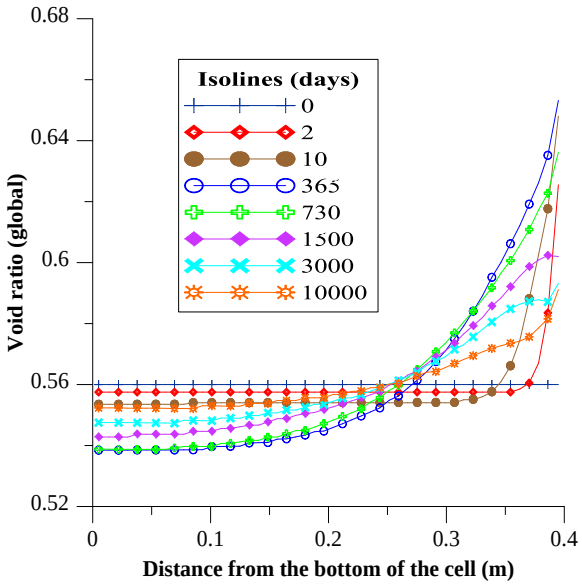

Figure 46. Distribution of global void ratio along the 40 cm infiltration cell for the isothermal case. Model predictions up to 10000 days.

Regarding now the results of liquid degree of saturation shown in Figure 47, it can be observed, that, as expected, higher values close to the hydration front and lower values near the bottom of the cell prevail. As the saturation cotinues, an increase in the liquid degree of saturation can be observed in all the sensor locations along the cell with a reduction in the hydration rate. In addition, it can be seen the similar shape of these curves with the ones showed by the micro void ratio. These results are in agreement with the adopted conceptual model that considers that a large amount of water is stored inside the micro-structure.

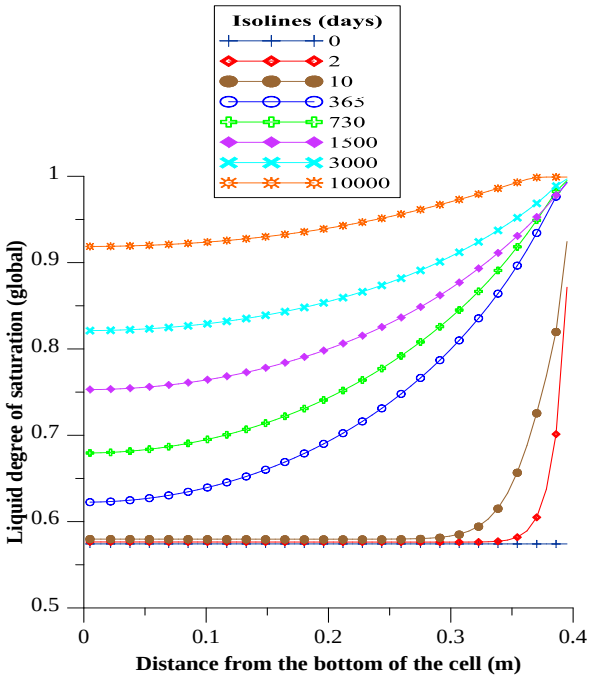

Figure 47. Distribution of liquid degree of saturation along the 40 cm infiltration cell for the isothermal case. Model predictions up to 10000 days.

The distribution of the macro void ratio along the cell for the non-isothermal case is shown in Figure 48. A swelling behaviour can be seen only at the beginning of the test and for a very small zone close to the hydration front. This swelling is due to suction reduction and also to the interaction mechanism between the two structural levels. For other times and locations, the values of macro void ratio are lower than the initial ones. This is caused by micro-structural expansion (see Figure 49) in the external zones due to hydration under constant volume conditions. The final condition corresponds to important reductions of the macro-pores along the cell especially near the hydration source. Another important phenomenon to be considered is the macro-structural compression or collapse that can be observed across the cell moving progressively to the bottom of the cell as hydration proceeds. The local wetting caused by the condensation of vapour coming from the zones close to the heater, induces a reduction in the macro void ratio. In this case (see Figure 50), the global void ratio is higher in the zones close to the hydration front and lower near the heater.

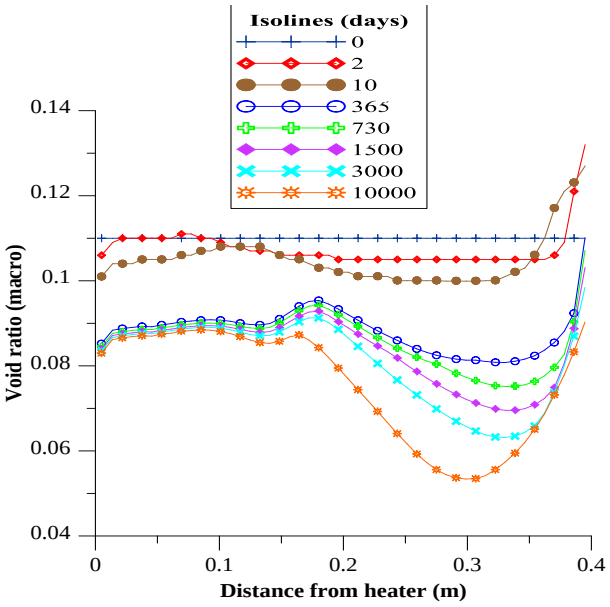

Figure 48. Distribution of the macro void ratio along the 40 cm infiltration cell for the non-isothermal case. Model predictions up to 10000 days.

Regarding the results of liquid degree of saturation (Figure 51), higher values close to the hydration front and lower values near the bottom of the cell are obtained, as expected. As hydration goes on, an increase in the liquid degree of saturation can be observed in all the locations along the cell with a reduction in the hydration rate. In addition, the similar shape of these curves with the ones showed by the micro void ratio can be noted, similarly to the previous case.

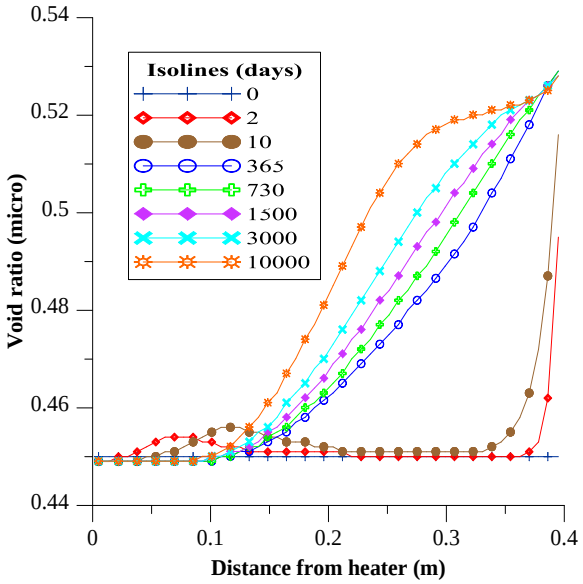

Figure 49. Distribution of the micro void ratio along the 40 cm infiltration cell for the non-isothermal case. Model predictions up to 10000 days.

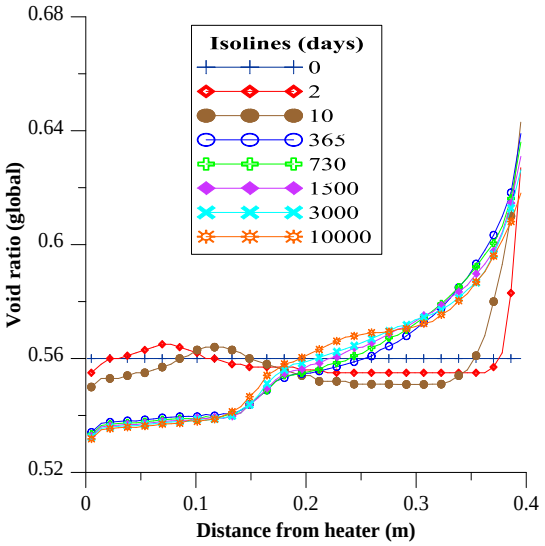

Figure 50. Distribution of global void ratio along the 40 cm infiltration cell for the non-isothermal case. Model predictions up to 10000 days.

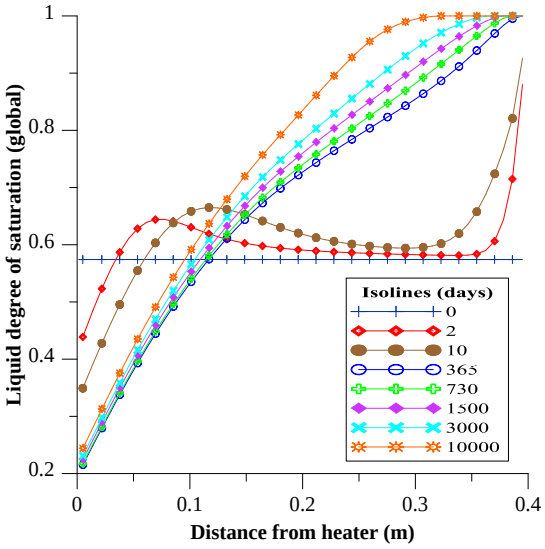

Figure 51. Distribution of liquid degree of saturation along the 40 cm infiltration cell for the non-isothermal case. Model predictions up to 10000 days.

3.2.5 Case Combining Micro-Fabric Evolution and Thermo-Osmosis Effects (DS+THO)

In order to extend the scope of the analysis, a simulation of the CIEMAT cell tests have been performed using a combination of the micro-fabric evolution and thermo-osmosis formulations. The aim is to check the response of the model assuming that these two plausible phenomena are acting simultaneously. To perform the simulations, the parameters from the two models were combined to obtain the best fit. Thus a value of the thermo-osmotic constant of 2.73×10^{-13} $m^2/K/$ (still within the experimental range) has been adopted. Since thermo-osmosis only occurs under thermal conditions, the modelling only covered the GT40 test. Figure 52 shows the evolution of temperature in the different positions along the cell. It can be seen that the agreement is very close. In the long term, Figure 53 shows that predicted values will remain constant throughout the first 30 years.

Figure 54 presents the numerical results of relative humidity. It can be observed that the model can predict quite satisfactorily the observed results. According to the model, the maximum

values of relative humidity until the end of the test (10 years) near the top (0.30 m), at the centre (0.20 m) and close to the heater (0.10 m) were 97 %, 80 % and 43 % respectively. In the long term (Figure 55), after the first 30 years, the model shows almost constant values of relative humidity.

In general, it can be stated that the combination of the Micro-fabric evolution and Thermo-osmosis cases makes this model quite capable to reproduce the thermo-hydro-mechanical (THM) phenomena observed in the infiltration test under non-isothermal conditions, at least in the shorter term. This analysis has been presented as a timely reminder that more than one of the additional phenomena considered van be acting at the same time, making the identification of the relevant phenomena more complex.

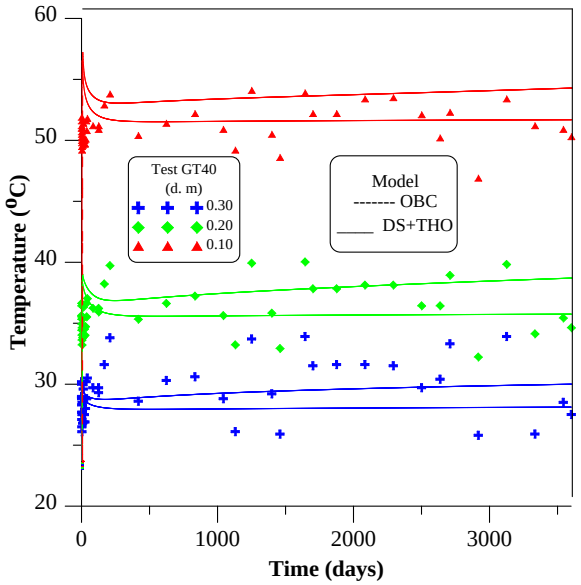

Figure 52. Evolution of Temperature for the GT40 Test: Experimental Data (scatter points) and Model Predictions up to 3600 days (10 years) for the (DS + THO) and (OBC) cases at 0.30 m, 0.20 m and 0.10 m from the bottom of the cell.

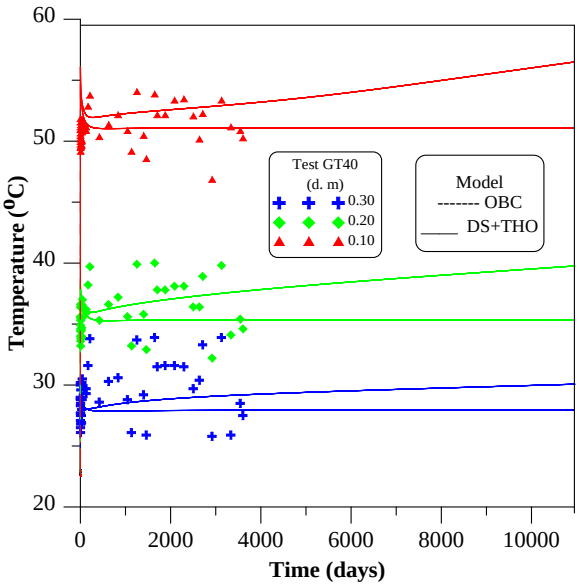

Figure 53. Evolution of Temperature for the GT40 Test: Experimental Data (scatter points) and Model Predictions up to 10950 days (30 years) for the (DS + THO) and (OBC) cases at 0.30 m, 0.20 m and 0.10 m from the bottom of the cell.

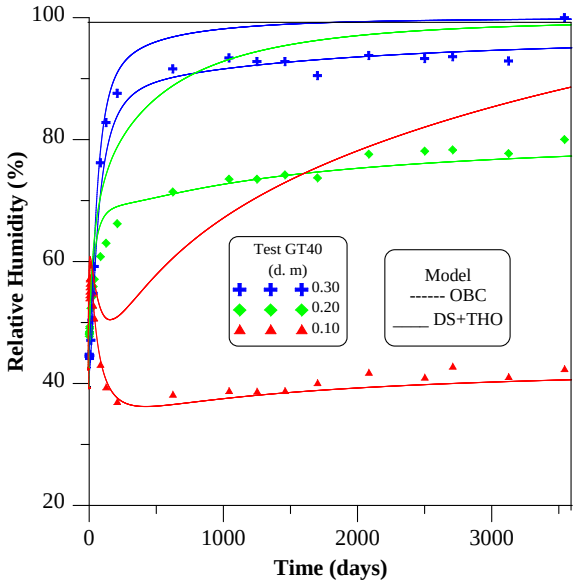

Figure 54.Evolution of Relative Humidity for the GT40 Test: Experimental Data (scatter points) and Model Predictions up to 3600 days (10 years) for the (DS + THO) and (OBC) cases at 0.30 m, 0.20 m and 0.10 cm from the bottom of the cell.

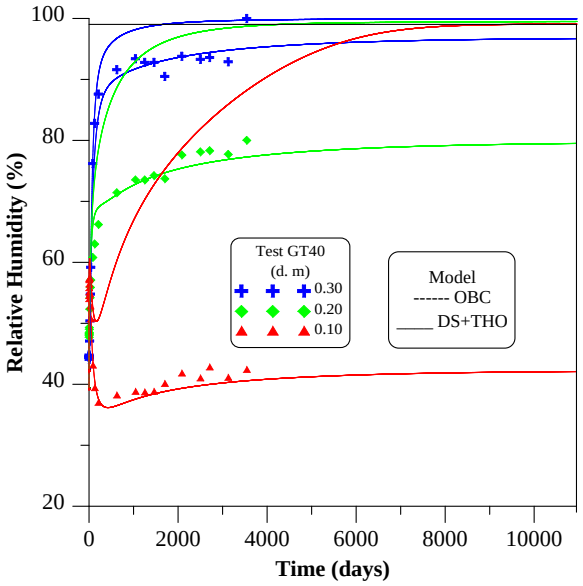

Figure 55. Evolution of Relative Humidity for the GT40 Test: Experimental Data (scatter points) and Model Predictions up to 10950 days (30 years) for the (DS + THO) and (OBC) cases at 0.30 m, 0.20 m and 0.10 cm from the bottom of the cell.

4. MOCK-UP TEST

4.1 Description of the Experiment

The FEBEX mock-up test is being carried out in the CIEMAT facilities in Madrid. The experiment avoids many of the uncertainties arising from the natural system. This is achieved mainly due to the good control of the initial and boundary conditions of the experiment. Figure 56 presents the main components of the test. Two electrical heaters (simulating canisters containing heat-emitting waste) are placed in the centre of a steel cylinder 6 m long and with an inner diameter of 1.62 m. The space between the heaters and the steel cylinder is filled with a 0.64 m-thick engineered barrier made up from blocks of compacted bentonite. The barrier is hydrated uniformly from all around the cylinder with an applied water pressure of 0.55 MPa. Simultaneously, the barrier is heated maintaining a constant temperature of 100 ºC at the contact between heaters and bentonite. A complete description of the mock-up test can be found in FEBEX Report (2000). It is convenient to comment here some characteristics of this experiment that are very suitable from a modelling point of view:

- the heterogeneities of the natural system (particularly the host rock) are avoided,
- the test has a clay barrier with an unlimited availability of hydration water, supplied at constant and controlled pressure,
- the mass of water introduced into the system is continuously measured and recorded,
- the boundary conditions are well defined
- the initial conditions are quite well-known at the beginning of the heating phase,
- the test is well instrumented, with several sensors located along the barrier which record the evolution of the main THM variables, and
- the experiment has two electrical heaters, symmetrically placed with respect to the central section of the test. This allows checking the reliability of measurements by comparing readings of symmetrical sections.

These facts facilitate the identification of the main processes and couplings that take place in a barrier submitted to heating and hydration.

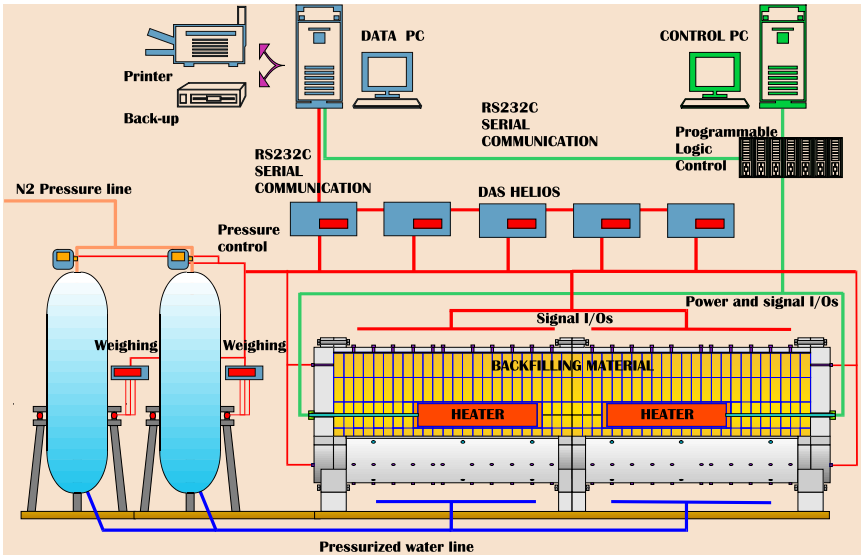

Figure 56. Scheme of the mock-up test (Martin & Barcala, 2005).

There are five basic units in the mock-up: the confining structure with its hydration system, the clay barrier, the heating system and heater control system (HCS), instrumentation, and data acquisition system (DAS). Figure 56 shows a schematic representation of the mock-up test with all of its physical components. These tests components are briefly presented in the following sections.

Confining structure and hydration system

The confining structure is a cylindrical body made of carbon steel with an inner length of 6.00 m and an internal diameter of 1.62 m. The surface of the cylindrical structure is perforated at 234 points: 186 for the exit of sensor cables and 48 for water injection that connect the cylindrical body with the hydration system.

The hydration system consists of two stainless steel tanks 3.0 m height and 0.8 m in diameter with a total capacity of 1.3 m^3. The system injects granitic water with a salinity of 0.02 % and a pH of 8.3 for the hydration of the bentonite at a constant and controlled pressure of 0.55 MPa. In order to homogenize the water supply around the periphery of the clay barrier, the internal surface of the confining structure is covered with several layers of geotextile.

Clay Barrier

The clay barrier is formed from highly compacted blocks of FEBEX bentonite. In total 25870 kg of bentonite were compacted to manufacture 1012 blocks. The blocks were fabricated with an average water content of 13.6 % and average dry density of 1.65 Mg/m^3.

Heating System and Heater Control System (HCS)

The heat system consists of two carbon steel cylindrical heaters with the corresponding monitoring and control systems. Each heater is 1.62 m long and 0.34 m in diameter. In this experiment, the heaters are in contact with the bentonite barrier and have a 0.75 m horizontal separation between them. The heaters are capable of individually supply the thermal power necessary to maintain a constant temperature of 100 °C in the heater/bentonite interface.

The HCS consists of all the electrical, electronic components and computer programs for the automatic supervision of the operation and control of the power supply to the heaters, data acquisition and activation of the processes and alarms in the event of failure of any of the components (heater resistor, electronics, etc…). The control parameter for the heating is either the temperature or the supplied power. In the event of failure of any of the heating elements, the control system compensates by using the rest of the heating elements. The nine sensors installed in each heater allow internal temperature distributions to be observed.

Instrumentation and Data Acquisition System (DAS)

In order to measure the continuous evolution of the variables in the test, the components of the system were instrumented with the appropriate temperature, total pressure, fluid pressure, relative humidity and deformation sensors. Table 9 shows the number and type of sensors, the variable measured and the location in the system.

The test has been divided in two zones, one including Heater A (Zone A) and the other containing Heater B (Zone B). The sensors in the clay barrier have been grouped into 25 sections, 12 in each zone, and one section (AB) that coincides with the central vertical plane. The instrumented sections are called Ann or Bnn, depending on the zone (A or B) and on the distance from the central vertical plane, where nn is the ordinal number of the placement. Figure 57 shows the two zones with the distribution of the different sections and Figure 58 the coordinate system for the identification of the location of the clay barrier sensors. .

In addition to the sensors placed inside the clay barrier, other sensors have been installed in the confining structure and in the outside auxiliary systems, as well as in the hydration and heater control systems.

These sensors are located on the surface of the heater and are distributed in three sections located near the front end cover (sensors numbered 1 to 4), in the control zone (sensors numbered 5 to 8) and in the solid end cover (sensor number 9). The sensors are distributed at 90º in each section, in a strip measuring less than 0.02 m in width. The control level is located in the middle of the heater and provides the average temperature value in order to calculate the power supplied to the heater.

Also, twenty temperature sensors have been installed on the outer surface of the confining structure at locations associated with the position of the deformation measuring points. Finally external sensors include all the signals that come from external sources such as room temperature or water pressure in the inner surface of the structure, from instruments in the hydration system (injection pressure and weight of tanks) and also the calculated values like the injected water volume, average control temperature and power supplied.

The Data Acquisition System (DAS) includes all the electronic components, as well as the software necessary to automatically supervise, record and store on a disk the data obtained from the test. The system is capable of acquire, adopt, display and record all the information generated by the installed instrumentation.

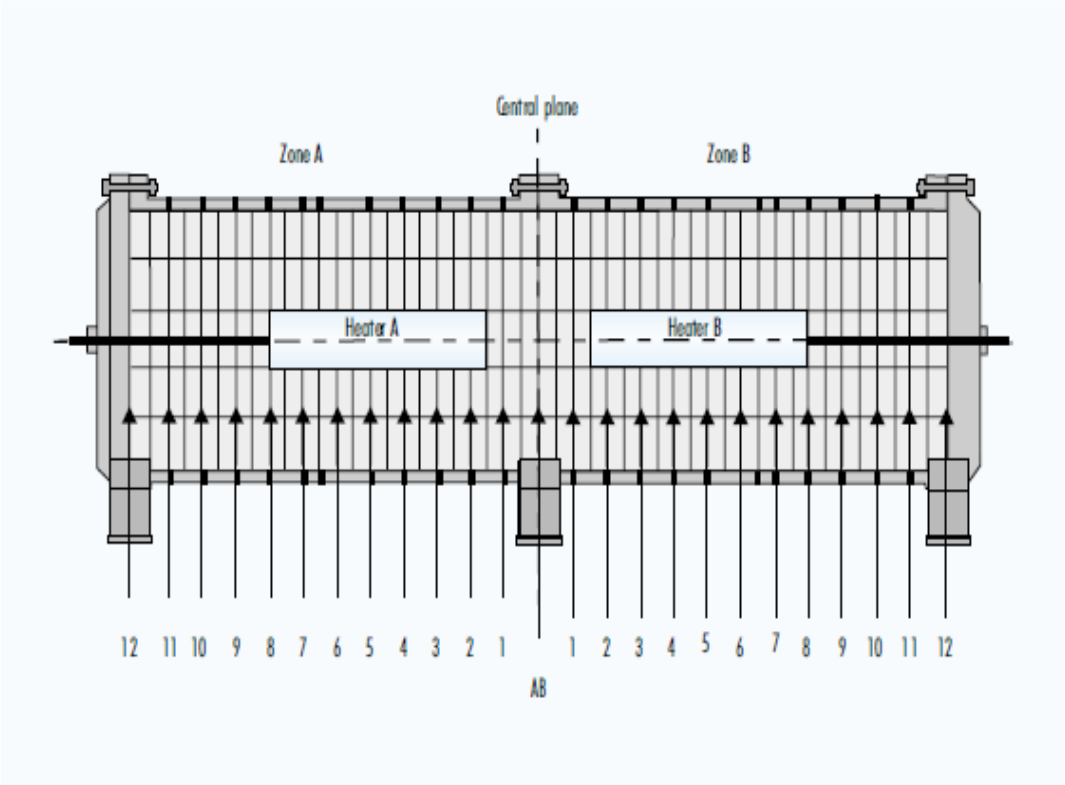

Figure 57. Distribution of instrumented sections (Martin & Barcala, 2005).

Table 9. Installed instrumentation (ENRESA, 2000).

Variable	**Type of sensor**	**Area**			**Total**
		Bentonite	Confining Structure	Exterior	
Temperature	RTD Pt100	328	20		348
Room temperature	RTD Pt100			1	1
Injection pressure					
manometer	DIGIBAR II			1	1
water pressure	DRUCK 1400PTX		2		2
Mass of hydration tanks	MVD 2510				
Total pressure					50
radial	KULITE BG0234	14			
tangential	KULITE BG0234	14			
axial	KULITE BG0234	22			
Fluid pressure	KULITE HKM375	20			20
RH + Temperature	VAISALA HMP233	40			40
Deformation (Strain gages)	HBM		19		19
PLC values					
temperature	RTD Pt100			18	18
average temperature	calculated			2	2
power	calculated			2	2
DC voltages				2	2
Totals		438	41	26	505

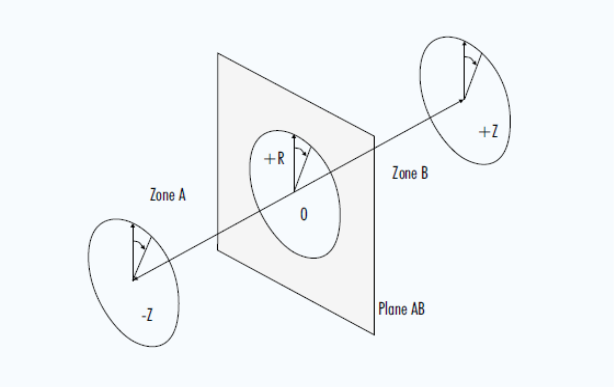

Figure 58. Cylindrical coordinate system in the mock-up test ((Martin & Barcala, 2005)).

4.2 Operational Base case (OBC)

A two-dimensional axisymmetric models has been used in the simulations of the mock-up test. In these simulations only one half of the problem (one heater) is analysed because of symmetry (Figure 59). The modelling presented herein is applied to the analysis of the behaviour of the mock-up test during the operational stage, i.e. the phase of heating and hydration of the test that started in February 1997 and is ongoing at present. The evolution of the experiment is critically examined by comparing the test data with the model results.

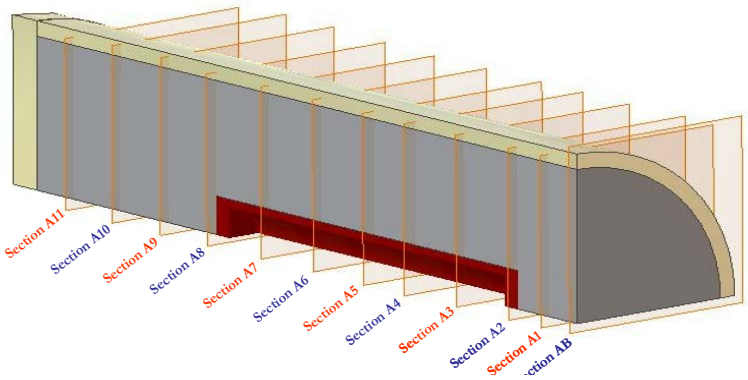

Figure 59. 3-D schematic representation of the barrier.

As explained in the analyses of the infiltration cells (Section 3), the experimental results from independent laboratory tests were used to obtain the parameters of the constitutive models for the thermal, hydraulic and mechanical problems, more details are given elsewhere (Huertas et al., 2006, Gens et al., 2009, Sanchez et al., 2012).

As explained previously, the OBC analysis was based on the Barcelona Basic Model (BBM), for isothermal conditions (Alonso et al. 1990) and expanded to the non-isothermal conditions by Gens (1995). The model incorporates the geotextile present between the confining structure and the buffer. The properties of this material have been reported in Martin & Villar (1997). The main longitudinal and transversal cross-sections selected for the analyses are shown in Figure 60.

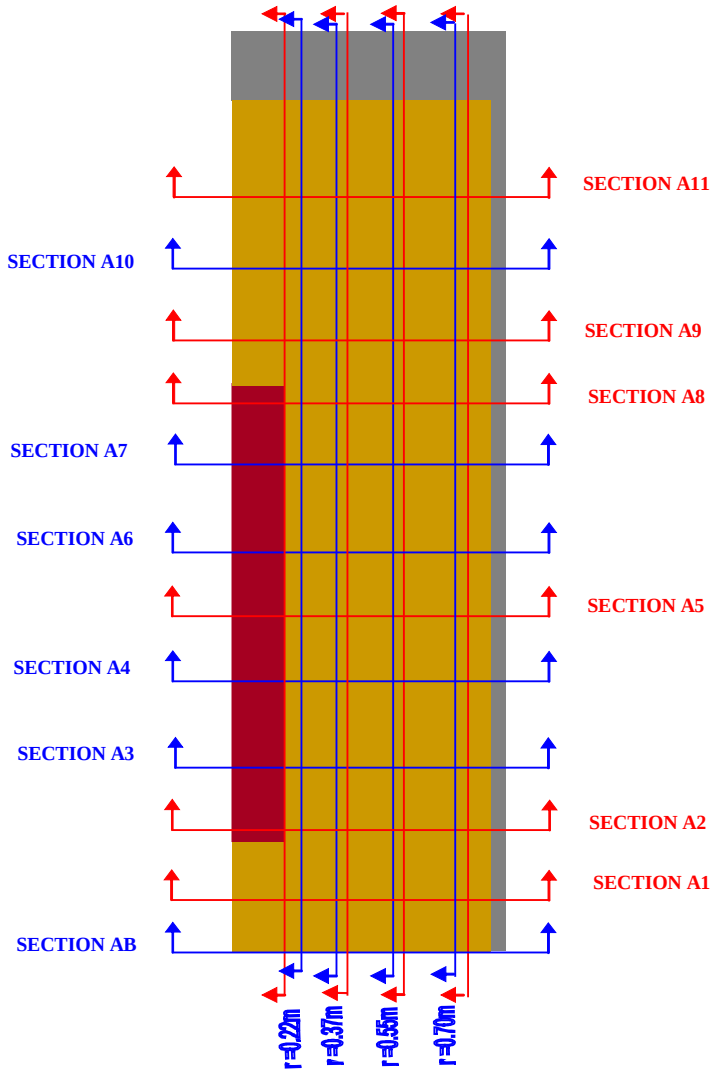

Figure 60. Longitudinal and transversal cross-sections. The schemes correspond to the Zone A only. In the Zone B, there are other similar instrumented cross sections symmetrically placed with respect to Section AB

The experimental values shown in the comparisons between model results and experimental data have been supplied by CIEMAT. The last record considered in the comparisons to be presented in this report corresponds to the day 5840 from the switching on of the heaters (i.e. around 16 years of testing).

In the following Sections the initial and boundary conditions assumed in the simulations are presented as well as a reference to the constitutive laws adopted. Afterwards, the most important results obtained during the operational stage are introduced.

4.2.1 Features of the analysis

Initial conditions

Thermal

An initially uniform temperature of 20 ºC is assumed for the entire domain. This is consistent with CIEMAT Report (2002) data.

Hydraulic

The initial water content of the bentonite is 14 %. That corresponds to a global degree of the saturation of the barrier of 58.1 %. Before the start of the heating, the mock-up test was flooded to try to achieve the closure of the gaps between the bentonite bricks prior to the performance of the main test. The procedure used and the events observed during and after the flooding are described in ENRESA (1997). During this flooding stage there was a total intake of 634 kg of water into the barrier. This implies a global degree of saturation of the barrier close to 71.50 %. An initial suction of 105 MPa has been adopted for the whole barrier, this suction is close to those measured (in average terms) in the central and internal zones of the barrier before the heater was switched on. According to the retention curve adopted, this implies an initial degree of saturation close to 65.2 %. In order to ensure that the test and the model have the same initial amount of water at the beginning of the heating, an initial (isothermal) hydration has been simulated until the global degree of saturation of the mock-up model reach the same value of the test (i.e. 71.50 %).

Mechanical

A hydrostatic value of 0.11 MPa has been adopted, approximately equal to the weight of the bentonite at the mid diameter of the buffer.

Boundary conditions

Thermal

The thermal boundary conditions at: r = 0.15 m, radial coordinate of the heater elements are:

- 0 - 6 days constant power 250 W/heater
- 6 days - t_{100} constant power 500 W/heater
- > t_{100} T = 100 ºC

where t_{100} is the time at which the temperature reaches 100 ºC at some point in the bentonite. In the performed analysis, t_{100} is 15.6 days.

On the external boundary, the following radiation condition has been applied:

$$j_e = \gamma_e \left(T^0 - T \right) \tag{43}$$

where j_e is the heat flow, T^0 is the prescribed temperature (T^0 = 20 ºC) and γ_e is the radiation coefficient. A coefficient γ_e =5 has been adopted. This value has been adjusted in order to ensure the prescribed condition (T^0) on the outer boundary.

Hydraulic

A water pressure of 0.55 MPa is applied in the geotextile (*i.e.* at the interface between steel and bentonite) in accordance with CIEMAT Report (2002) data. Regarding the gas pressure it is not absolutely clear if the experiment is airtight or not. The analysis presented herein assumes that the test is airtight.

Mechanical

A stress free outer boundary has been prescribed.

Constitutive laws adopted in the OBC analysis

This section presents the numerical analysis based on the OBC model. This model is the same as the one used during the simulations of the infiltration tests discussed in section 3.2.1. However, in this analysis a 2D axis-symmetric model has been adopted. The main constitutive laws adopted in the OBC analysis of the mock-up test for the thermal, hydraulic and mechanical problems together with the required material parameters have been presented in the description of the conventional formulation (section 2.1.2)..

4.2.2 Results of the numerical analysis

The results of the 'OBC' analysis are presented and discussed in relation to their comparison with observed values. Both, point variables and global test parameters are examined. The evolution of the mock-up test is analysed considering the thermal, hydraulic and mechanical problem separately. The sections used in the comparisons presented hereafter have been shown in Figure 60.

Thermal

It can be stated that the model yields good results regarding the thermal problem. This is reflected in the evolutions of the power emitted by the heaters, a global variable of the test Figure 61. The model tendency indicates a slow increment of the heater power as the barrier is hydrated; this is due to the increase of thermal conductivity as saturation increases. At a later stage of the test, the thermal condition of the test was changed to one of constant power, as reflected in Figure 61.

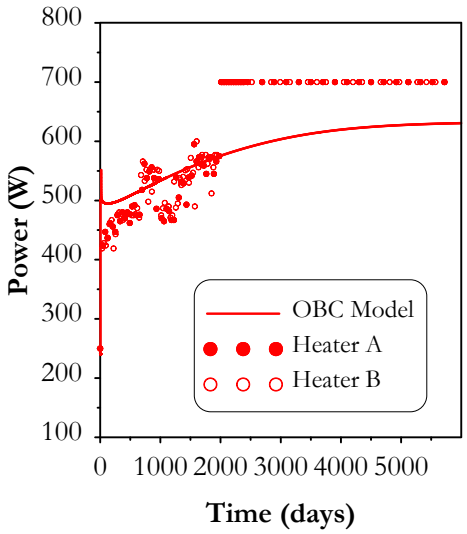

Figure 61. Evolution of heater power in the mock-up test. Observed and computed values (OBC model).

Satisfactory results are also obtained in terms of local variables, such as the evolution of temperatures at different points of the barrier (Figure 62 and Figure 63). It can be noted that there are some small differences in the temperature field, especially in zones close to the heater. They may be the effect of a somewhat lower thermal conductivity in the discontinuity that may exist between heater and bentonite. Also the temperature at different radii of the barrier increases slowly as hydration goes on.. It can be observed that the global tendency of the test is generally well captured by the model.

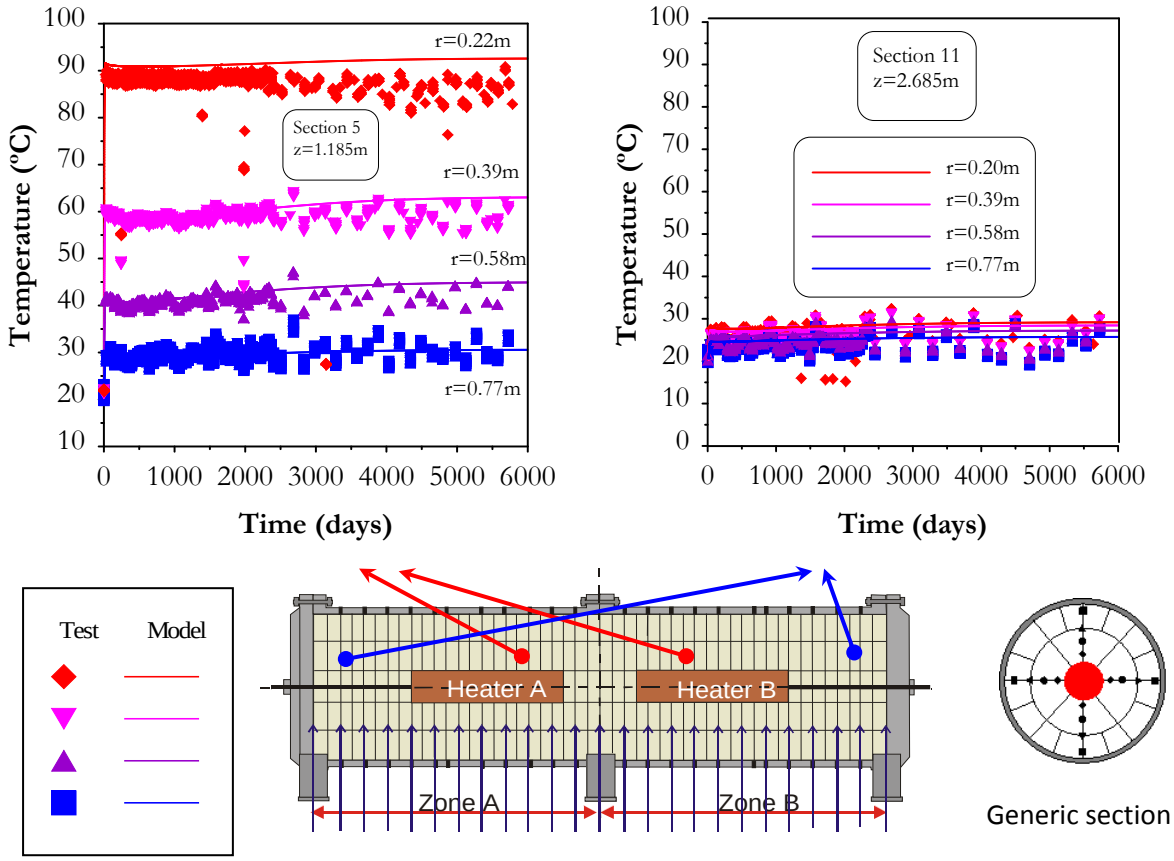

Figure 62. Evolution of temperature in the mock-up test. Sections A5-B5 (‘hot cross-section’) and A11-B11 (‘cold cross-section’). Observed versus computed values (OBC model).

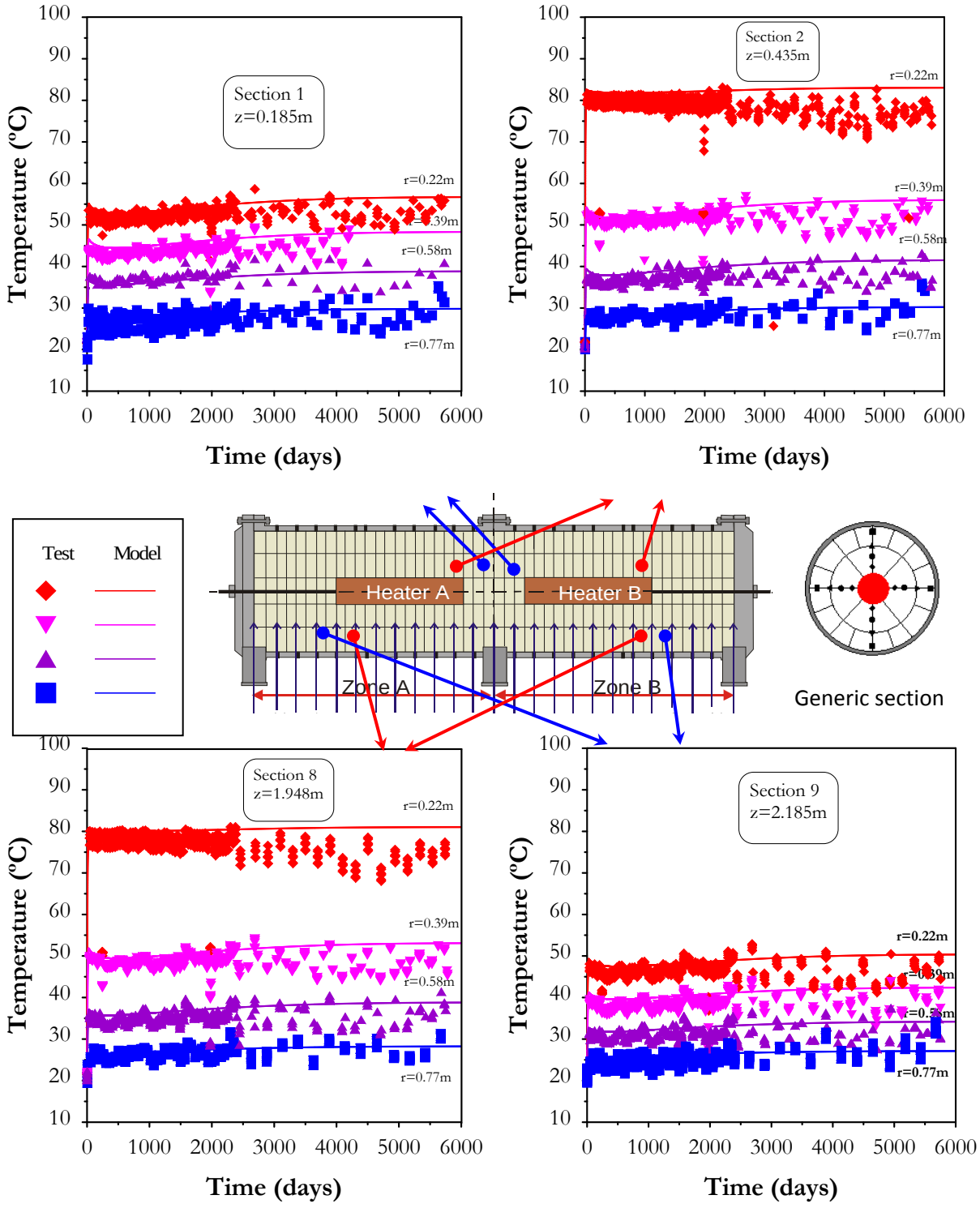

Figure 63. Evolution of temperature in the mock-up test. Sections 1, 2, 8 and 9. Observed versus computed values (OBC model).

Hydraulic

Observing the hydraulic global variables of the test, water entry and rate of water entry, it can be stated that the OBC model predictions can be considered good until the day 900 (approximately) with differences between model results and test data lower than 10% (Figure 64). Regarding the local variables, a similar comment can be made, that is, until the day 900 the

model offers a good reproduction of the evolution of relative humidity (Figure 65). Up to that time, the overall behaviour of the test is the expected one, i.e. an increasing saturation in the zones close to the hydration boundary and an intense drying in the regions close to the heaters followed by a slow hydration. The behaviour of zones close to a radius of 0.37 m shows an initial wetting, due to the condensation of the water vapour coming from the inner region followed by drying due to heating.

From about day 900, some differences are observed between the hydraulic behaviour of the test and model predictions. In terms of the water entry, the model results move away progressively from the experimental data. This fact can be clearly detected in terms of the rate of water intake, in which the test data (from day 900 of the test) undergo an important reduction in comparison with the output of the 'OBC' model.

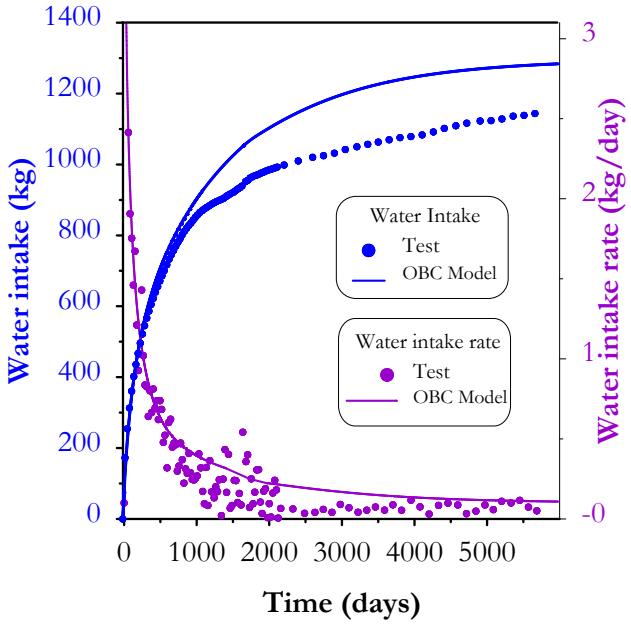

Figure 64. Evolution of water entry in the mock-up test. Observed and computed values (OBC model).

A recovery of the observed values of water intake rates can be seen when an overheating episode, on day 1381, took place. Finally the tendency observed before the overheating was recovered, i.e. a clear slowing down of the rate of water intake compared with model predictions

In relation to the evolution of relative humidity in sections involving heaters (for instance, sections A4 and B4, in Figure 65) a significant reduction in the rate of relative humidity increase can be observed. The effects of the overheating can be clearly noted in these sections, during and after the episode. It seems that the transient period induced by overheating was practically over after day 1700. A clear tendency towards a very slow hydration rate in all of the measured radii can be noted when examining advance stages of the results. On the other hand, when sections away from the heaters are examined (for instance, sections A10 and B10, in Figure 65) the hydration deviations are less marked but still perceptible. Note that some small differences between model and test results can also be observed in these sections after day 2000 (approximately). Figure 66 shows the evolution of relative humidity for other sections of the test. The apparent slow hydration observed in Sections A4 and B4 can be also observed in the other sections involving heaters.

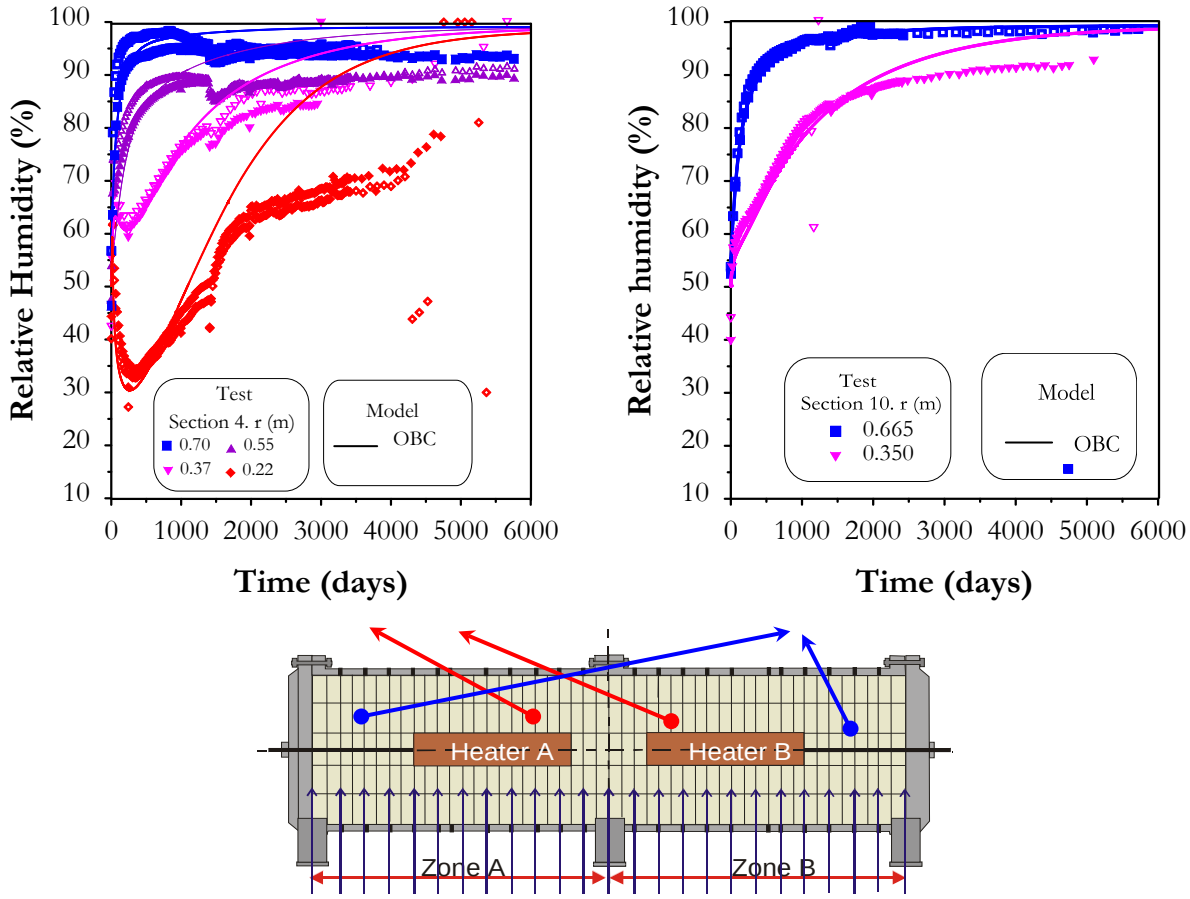

Figure 65. Evolution of relative humidity in the mock-up test. Sections A4-B4 ('hot cross-section') and A10-B10 ('cold cross-section'). Observed versus computed values (OBC model).

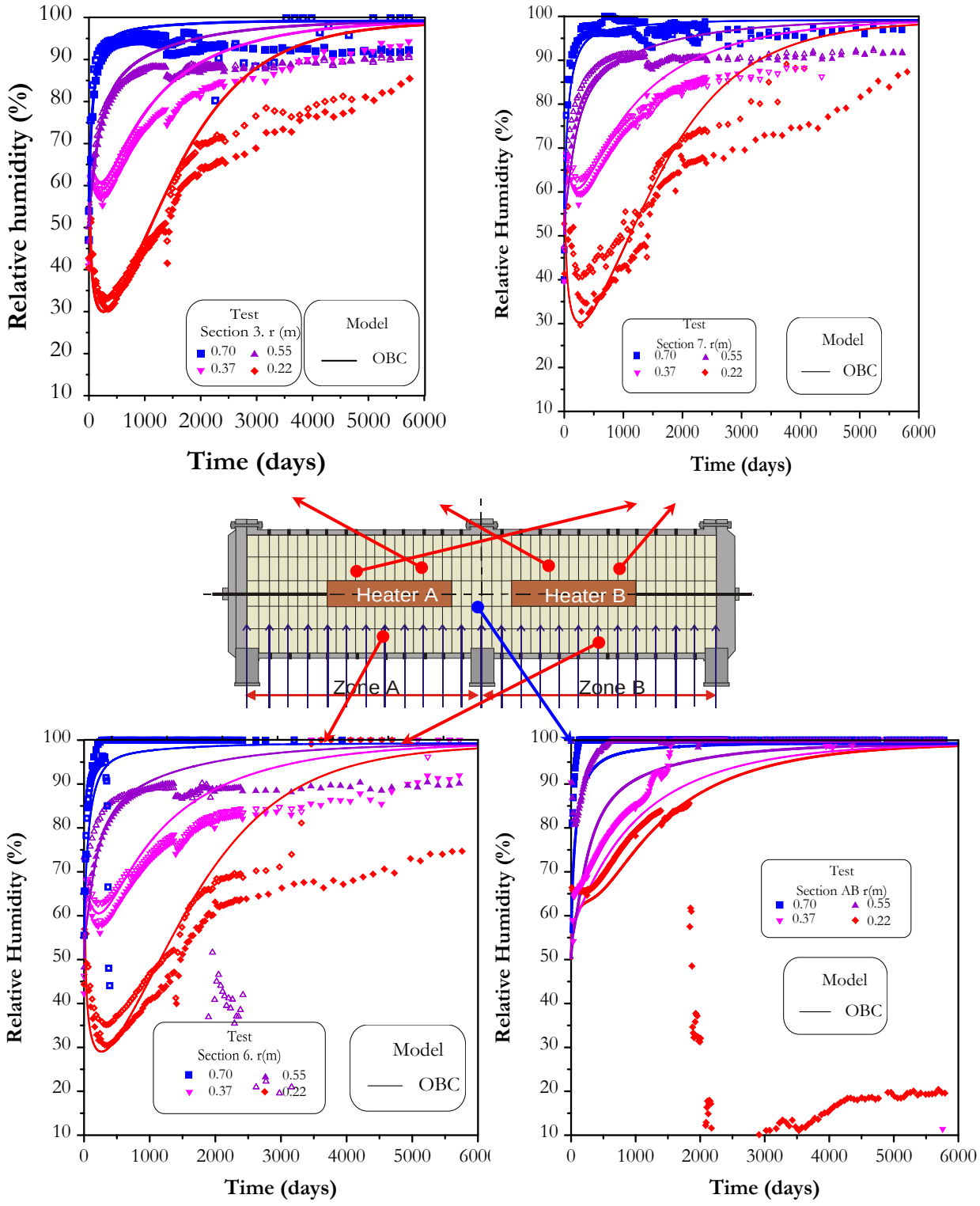

Figure 66. Evolution of relative humidity in the mock-up test. Sections 3, 6, 7 and AB. Observed versus computed values (OBC model).

Figure 67 compiles the results in term of relative humidity for all the instrumented Sections studied and the four different radii observed in this experiment. It is quite clear that the OBC model over-predicts the rate associated with the saturation of the barrier for all the sections instrumented and all the positions analysed, except for the sensors close to the hydration boundary.

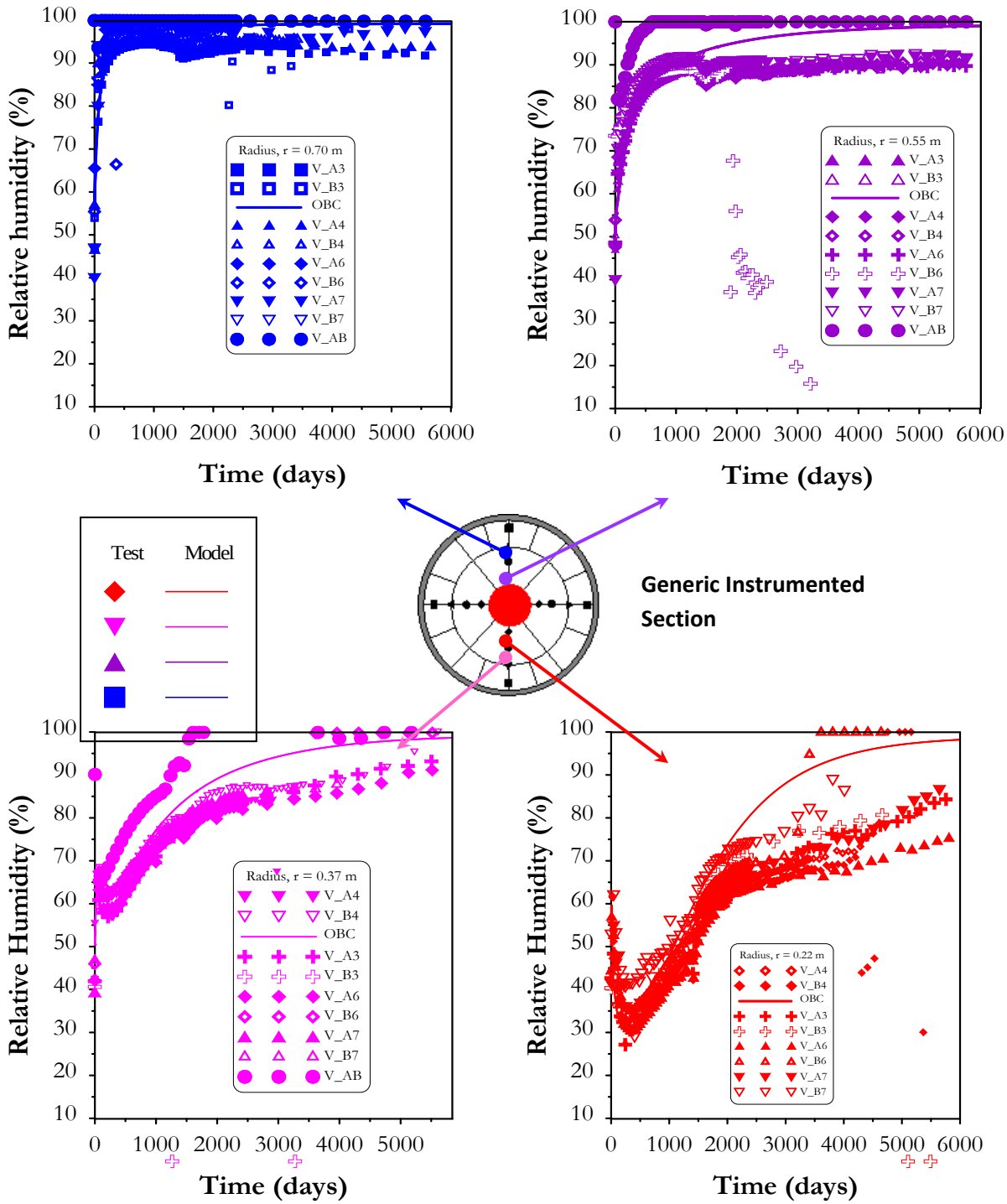

Figure 67. Evolution of relative humidity in the mock-up test, for all the instrumented Sections at the four different radii studied. Observed versus computed values (OBC model).).

Mechanical

Figure 68 and Figure 69 show the time evolution of stresses in selected positions of the barrier, where: P_T: identifies the tangential stress, P_Z the longitudinal stress and P_R the radial stress. Similar trends to the ones observed in the hydraulic problem appear in the mechanical problem. That is, up to day 900 approximately, there is a good agreement between predictions and observations in sections involving the heaters. From that moment on, measured stresses respond to the modifications of the hydration pattern, and a tendency to maintain or reduce stress values can be observed. This is attributed to the strong hydro-mechanical coupling of the problem.

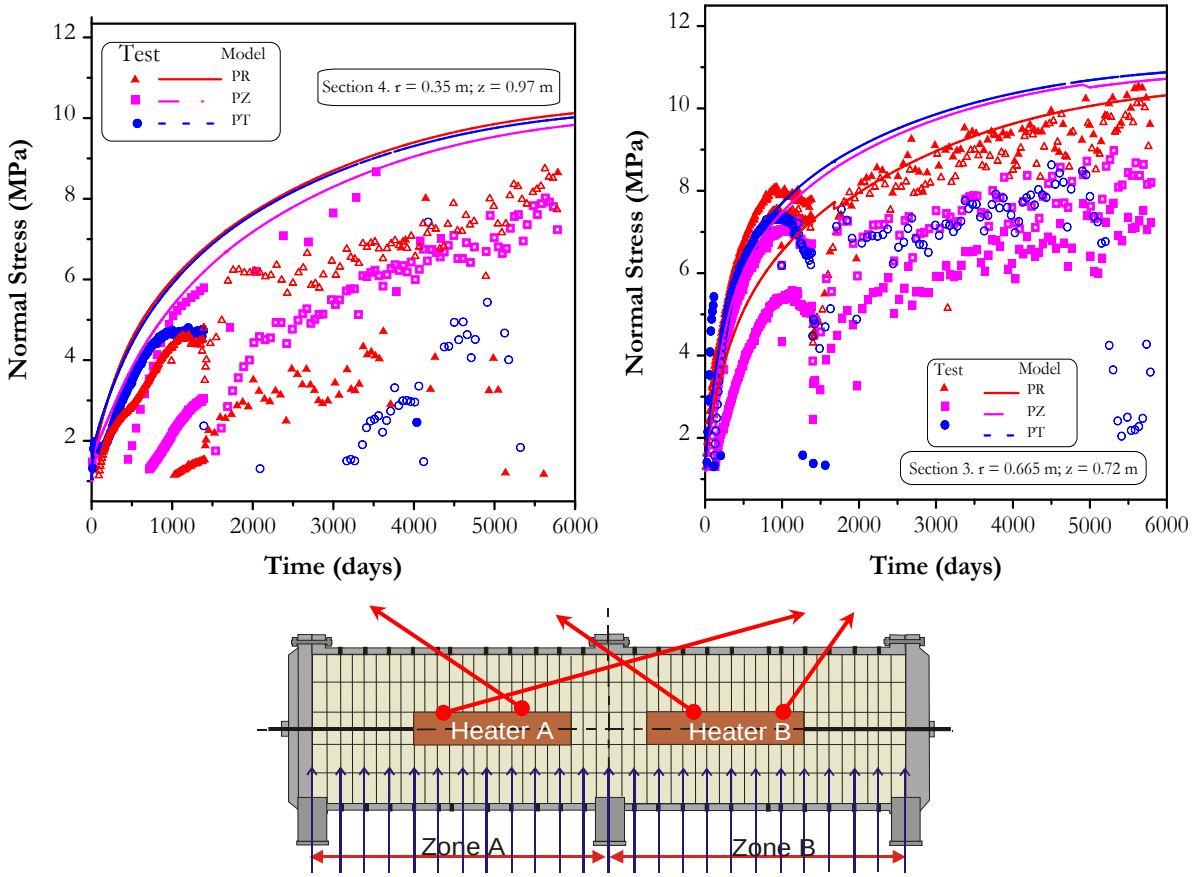

Figure 68. Evolution of stresses in the mock-up test. Sections 3 and 4. Observed versus computed values (OBC model).

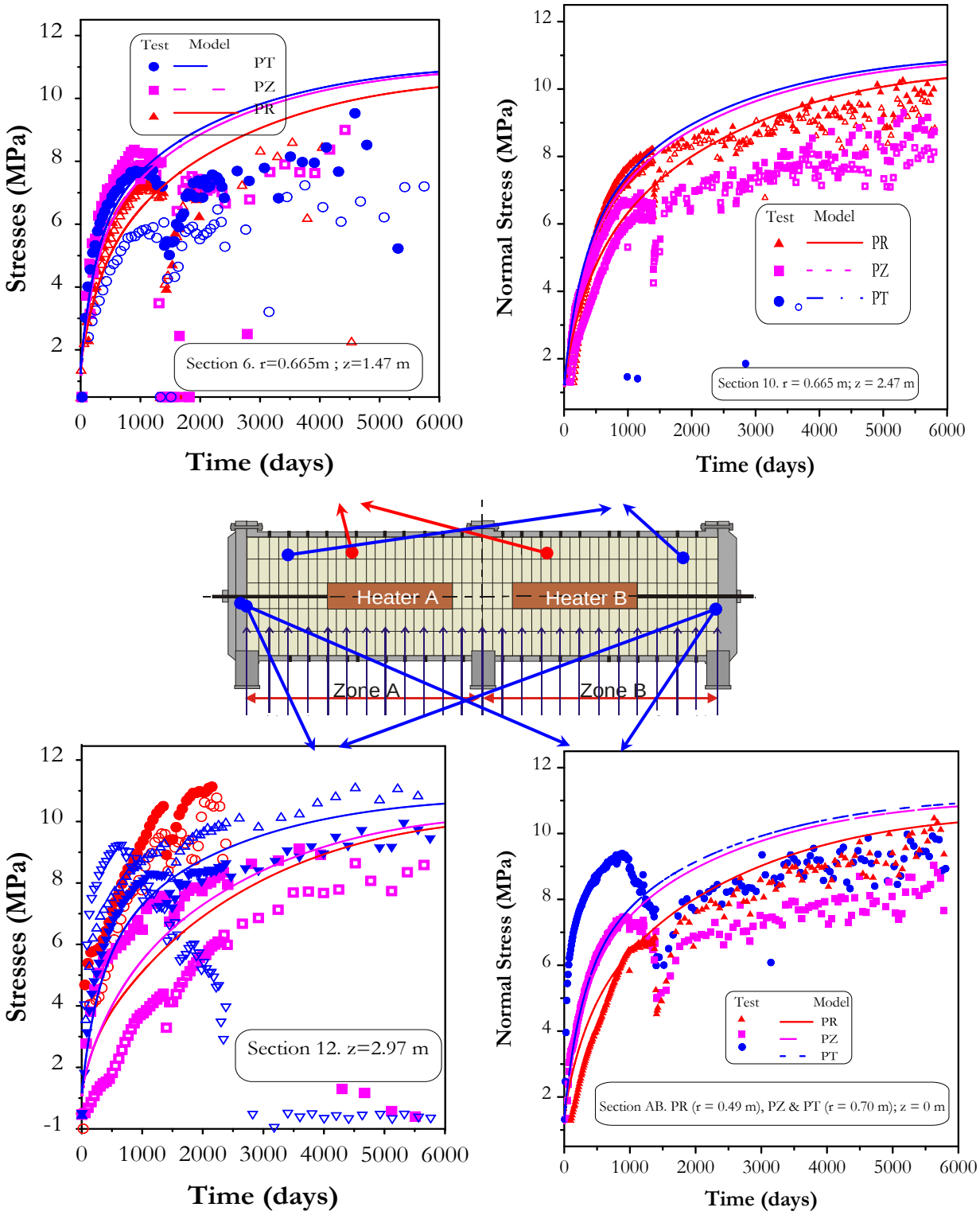

Figure 69. Evolution of stresses in the mock-up test. Sections A6-B6, A10-B10, A12-B12, and AB. Observed versus computed values and long-term predictions (OBC model).

The overheating episode had different influences on mechanical behaviour depending on the sections considered. In sections far from the heaters, the values and tendency recorded before this event have been recovered practically immediately (Section A10 and B10, Figure 69), whereas in sections involving heaters, a more permanent influence on the evolution of the stress field can be observed. An explanation of these observations that required the use of the double structure constitutive model was proposed by Sanchez et al. (2005). Finally, in zones near the ends, the overheating event has no perceptible effects and the model captures very well the measured values of stresses (Section A12 and B12). At advanced stages of hydration the measured maximum stress are moving towards an asymptotic value around 10 MPa.

4.3 Mock-up test analyses using modified formulations

The three phenomena proposed in Section 2 to enhance the conventional THM formulation are also used in this Section to study the evolution of the mock-up test hydration during heating.

4.3.1 Non-Darcy flow (THG)

In this section, the approach that incorporates the presence of a threshold hydraulic gradient (THG) in the flow law is adopted. The discussion will focus on two characteristics groups of sections: i) sections involving the heaters (e.g. Sections A4 & B4); and ii) sections away from the heaters (e.g. Sections A10 & B10). The some model parameters adopted in Section 3.2.2 to simulate the infiltration cell have been assumed in the analyses presented below (i.e. THM parameters for OBC model plus threshold hydraulic gradient = 50 and power law = 180). The results obtained with the OBC model are included as a reference.

Figure 70 shows the evolution of water intake in the mock-up test, taking into account the phenomenon of the threshold hydraulic gradient. It can be noted that the slowing down in the hydration rate obtained with the THG model is noticeable. This means that the model is able to capture the reduction in water intake observed in the experiment. Quite satisfactory numerical results are obtained up to the 4000 days of the experiment. After that time, a tendency of the model to reach a steady state condition is observed, resulting in a modest underestimation of model for predicting the measured water intake.

Regarding the relative humidity, it can be observed that there was also an improvement in the model predictions if we compare them with the ones obtained from the OBC model. In sections close to the heater (Figure 71), the model is able to capture the hydraulic behaviour observed in this area especially in the sensors near the heater (i.e. position 0.22 m and 0.37 m).

The model predicts very well the initial drying and the subsequent hydration pattern. However, in the positions where the sensors are away from the heating zone (i.e. positions 0.55 m and 0.70 m), the model still overestimates the measured values. In sections A10 & B10, where there is no influence of the heater, the model predicts very well the trend showed by the experimental data as presented in Figure 72.

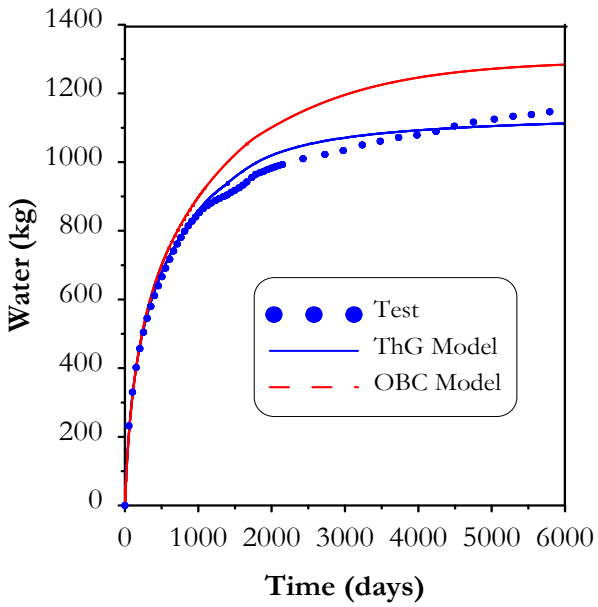

Figure 70. Evolution of water intake during the mock-up test. Measurements (scatter points), THG and OBC model predictions up to 6000 (days).

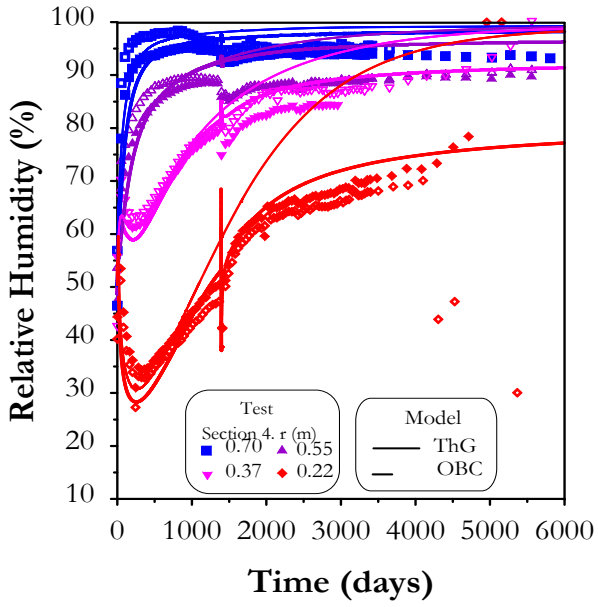

Figure 71. Evolution of relative humidity in sections A4 and B4 during the mock-up test. Measurements (scatter points), THG and OBC model predictions up to 6000 days.

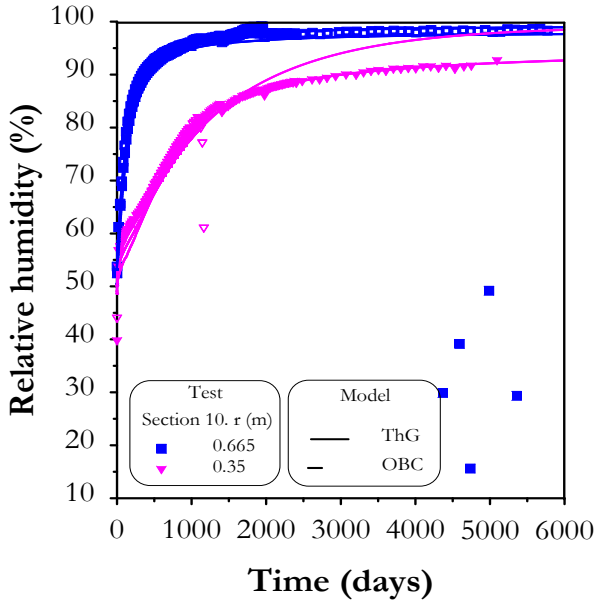

Figure 72. Evolution of relative humidity in sections A10 and B10 during the mock-up test. Measurements (scatter points), THG and OBC model predictions up to 6000 days.

In summary, the inclusion of the threshold hydraulic gradient (THG) model in the conventional formulation improved the predictions obtained in the numerical analysis. The model was able to reproduce quite satisfactorily the evolution of the main hydraulic variables due to its capability to slow down the hydration rate in the bentonite barrier. The adopted parameters, however, appear to underpredict the long-term saturation of the barrier.

Naturally, the relevance of this prediction depends on the existence of a threshold gradient in the FEBEX bentonite and, if this is this case, on the adequacy of the model and parameters adopted here. Therefore, the result presented should be considered only as an exercise with the object to explore the hypothetical response of the barrier under these assumptions, until the hypotheses regarding the existence and magnitude of a threshold gradient and associated parameters are independently confirmed by experiment.

4.3.2 Thermo-osmosis (THO)

In this section, the formulation incorporating the presence of Thermo-osmotic (THO) flow in the hydraulic model is adopted. The discussion will also focus on the same two characteristics groups of sections: i) sections involving the heaters (as e.g. the Sections A4 & B4); and ii) sections away from the heaters (e.g. Sections A10 & B10). The same model parameters adopted in Section 3.2.3 to simulate the infiltration cell have been assumed in the analyses presented below (i.e. THM parameters for OBC model plus a coefficient K_{HT}=2.73 x10^{-13} m^2/K/s). The results obtained with the OBC model are included as a reference. It is important to recall that thermo-osmosis is related to the movement of water as liquid in the presence of thermal gradients. At advanced stages of this test, when the hydraulic gradient becomes small, thermo-osmosis effects may become relevant.

The following figures show the evolution of water intake and relative humidity during the mock-up test. The solid lines correspond to model predictions considering the thermo-osmosis (THO) effect and the dashed lines correspond to the results obtained from the Operational Base Case (OBC).

Regarding the results in terms of the water intake (Figure 73), it can be seen that the inclusion of the thermo-osmosis model has a positive effect on the numerical results. As expected, there was

a reduction in the rate of water intake and the computed values became closer to the measured ones. However, after the 1000 day, there was an overestimation of the observed values.

Figure 74 shows the results of relative humidity in sections A4 & B4 up to 6000 days. It can be noted the overall improvement on the numerical results (especially in the positions close to the heater) when the THO model is considered in the analysis. The model is able to capture very well the observed pattern up to 2000 days. After that time, the model predictions start to move apart from the measurements, leading to an overestimation of the experimental data. The results in Figure 75 for sections A10 & B10 show no change respect to the OBC model since this part of the system is not affected by temperature incraese and therefore thermo-osmosis has no effect.

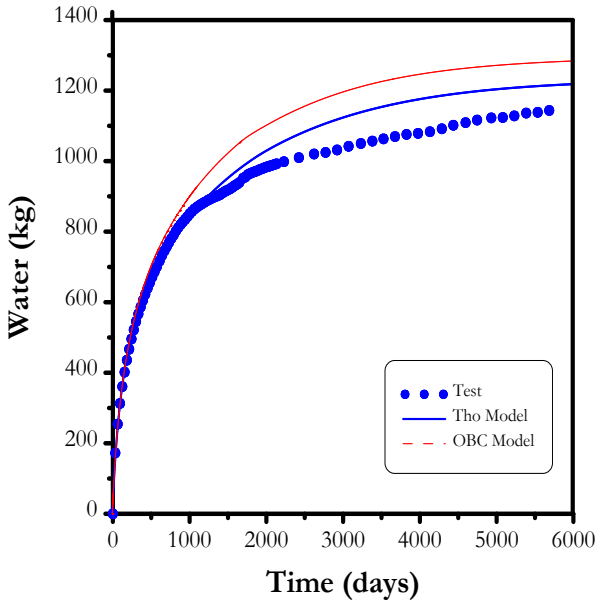

Figure 73. Evolution of water intake during the mock-up test. Measurements (scatter points), THO and OBC model predictions up to 6000 days.

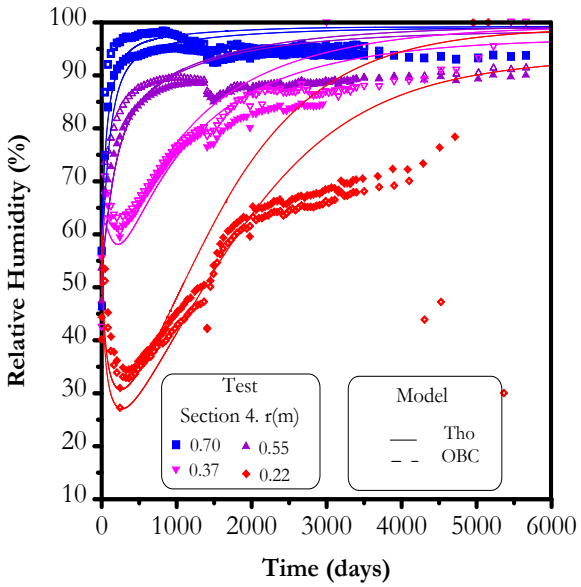

Figure 74. Evolution of relative humidity in sections A4 and B4 during the mock-up test. Measurements (scatter points), THO and OBC model predictions up to 6000 days.

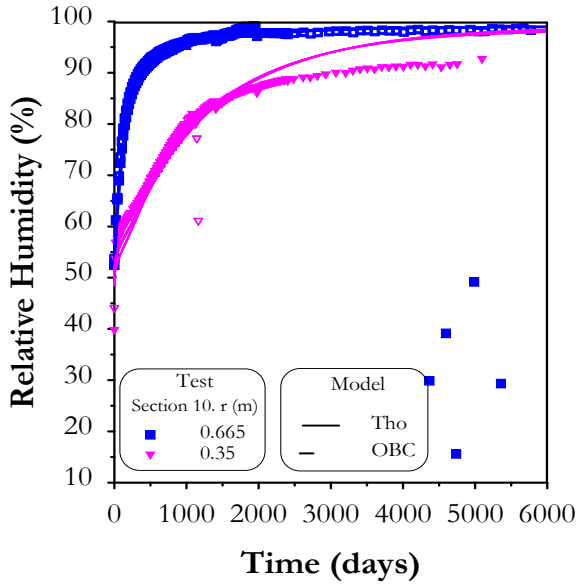

Figure 75. Evolution of relative humidity in sections A10 and B10 during the mock-up test. Measurements (scatter points), THO and OBC model predictions up to 6000 days.

In summary, the addition of the thermo-osmosis effect to the conventional formulation has contributed to the improvement of the model predictions by slowing down the hydration rate inside the barrier. This results in a quite satisfactory agreement between observations and computed values especially in zones near the heat source at the earlier stages of the test but the model overestimates the values at advanced stages of the test (after 2000 days). It does not reproduce the observed slow hydration in the 'cold section' either.

4.3.3 Micro-fabric evolution (DS)

In this section, the double structure (DS) model has been adopted in the analysis to study numerically the main THM variables measured during the heating and hydration of mock-up clay barrier. The discussion again will focus on the same two characteristics groups of sections: i) sections involving the heaters (as e.g. the Sections A4 & B4); and ii) sections away from the heaters (e.g. Sections A10 & B10). The double structure model adopted in Section 3.2.4 to simulate the infiltration cell has been assumed in the analyses presented below with one exception. The difference is in the permeability law. In the simulation below the assumed intrinsic permeability is K=3.0x10^{-21}, the initial macro porosity ϕ_M=0.12, and power parameter b=12 (Equation 42).

The following figures show the evolution of temperature, water intake and relative humidity measured during the mock-up experiment with the corresponding model predictions. The results obtained with the OBC model are included as a reference Figure 76 shows the evolution of temperature in sections A5 & B5 for a period of 6000 days. It can be observed the model is able to reproduce quite well the thermal field.

The evolution of water intake is presented in Figure 77. It can be observed that the model predicts satisfactorily the trend observed in the experiments. A notable improvement was achieved in the numerical results when compared to those obtained by the OBC model.

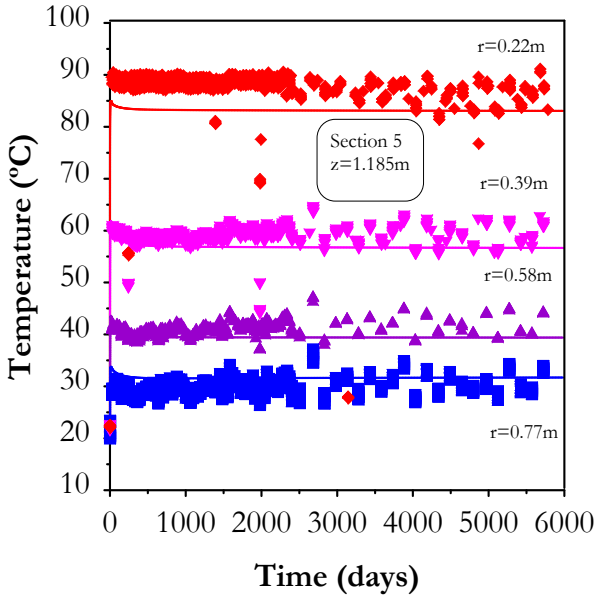

Figure 76. Evolution of temperature in sections A5 and B5 during the mock-up test. Measurements (scatter points) and DS model predictions up to 6000 days.

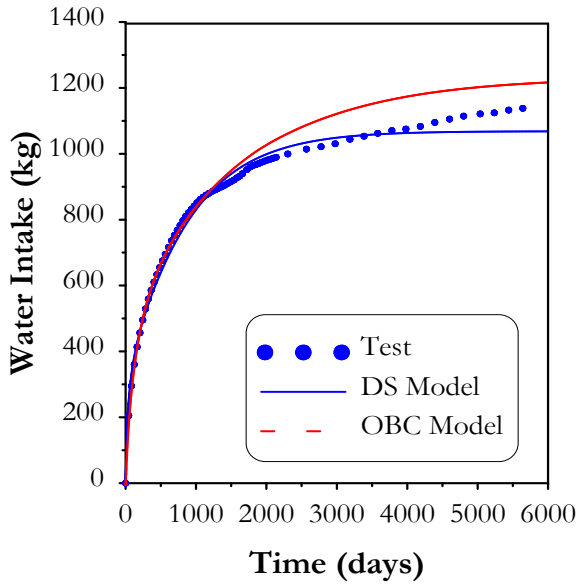

Figure 77. Evolution of water intake during the mock-up test. Measurements (scatter points), DS and OBC model predictions up to 6000 days.(Tengo que cambiar esta grafica, no corresponde)

The results of relative humidity for some typical cross sections involving heaters (i.e. A3 & B3; A7 & B7, A6 & B6; and A4 & B4) are presented in Figure 78. As these Figures show, significant improvements in the numerical results are achieved when compared to those obtained with the OBC model, especially in zones close to the heater (i.e. r = 0.22 m and r = 0.37 m). The model was able to reproduce the slowdown observed in the hydration rate of the mock-up barrier. This resulted in a better agreement with the measured values. Another important observation is that after 6000 days, the bentonite will still be unsaturated. Figure 79 presents the numerical results associated with the sections A10 & B10 (i.e. sections located outside the heater zone), there is not a significant difference between the two model predictions (i.e. OBC and DS).

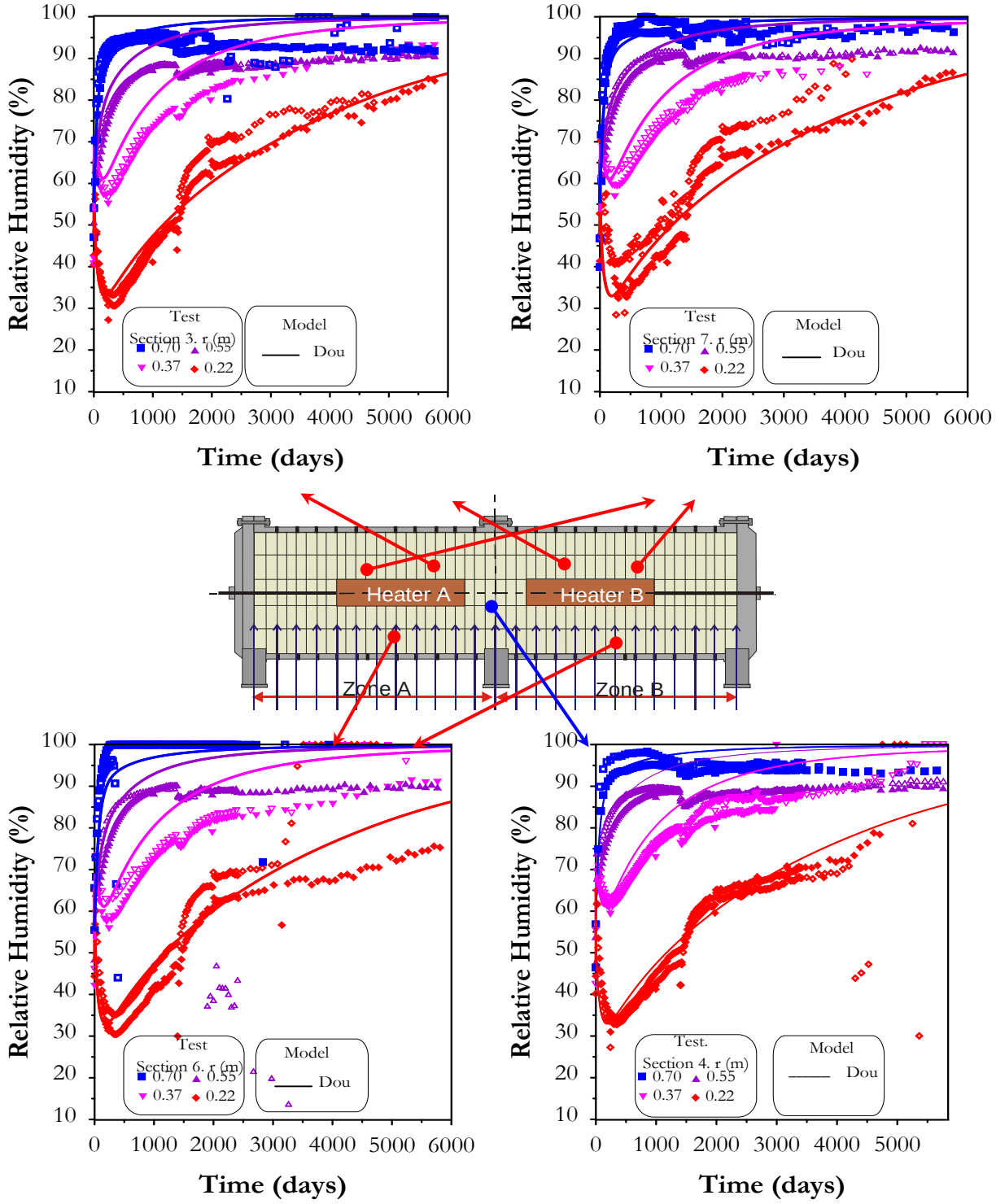

Figure 78. Evolution of relative humidity in the mock-up test. Sections 3, 7, 6 and 4. Observed versus computed values (DS and OBC models) up to 6000 days.

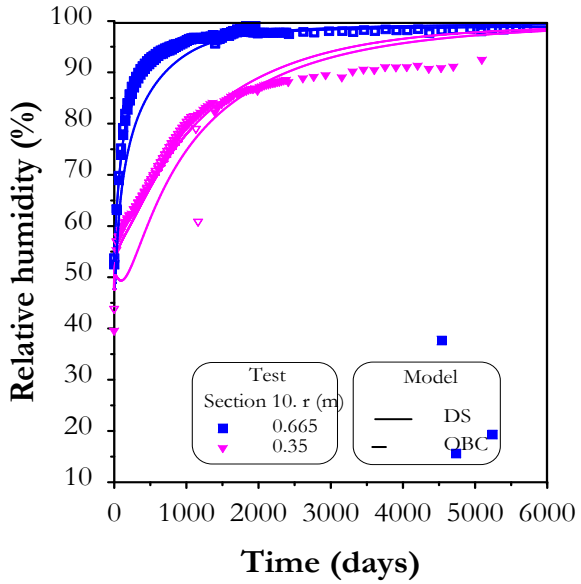

Figure 79. Evolution of relative humidity in sections A10 and B10 during the mock-up test. Measurements (scatter points), DS and OBC model predictions up to 6000 days.

Figure 80 compiles the comparison between DS model and experimental observation up to 6000 days, in term of relative humidity for all the instrumented Sections studied and the four different radii studied in this experiment. It is quite clear that the DS model is able to replicate quite satisfactorily the barrier hydration for most of the instrumented sections involving heaters.

Figure 81 extends the comparison between DS model and experimental observation for the long term (up to 10950 days, i.e. 30 years), in term of relative humidity for all the instrumented Sections studied and the four different radii studied in this experiment for the . The DS model predicts that the barrier tends towards (almost) full saturation in all zones, including areas near the heater.

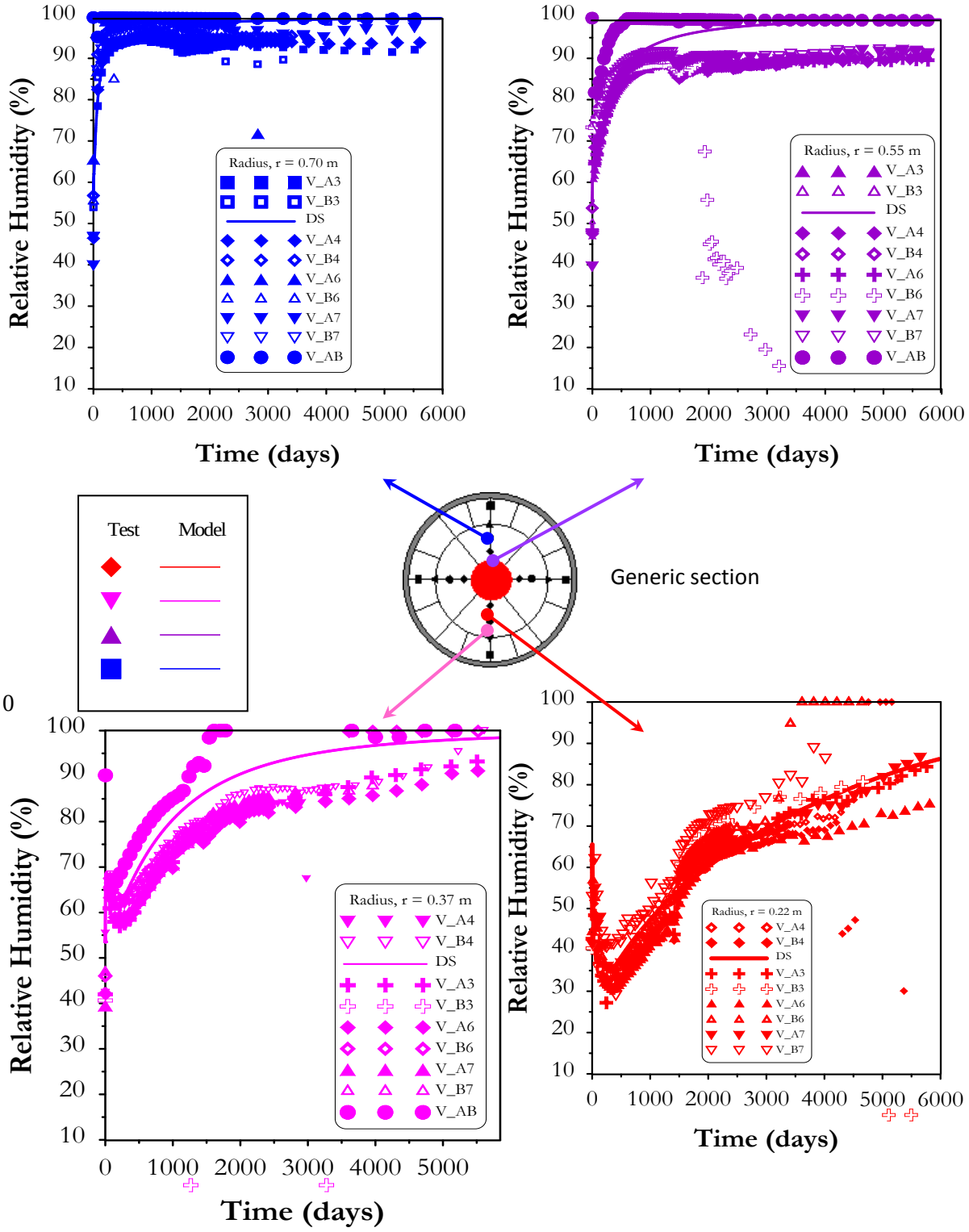

Figure 80. Evolution of relative humidity in the mock-up test, for all the instrumented Sections at the four different radii studied. Observed versus computed values (DS model) up to 6000days..

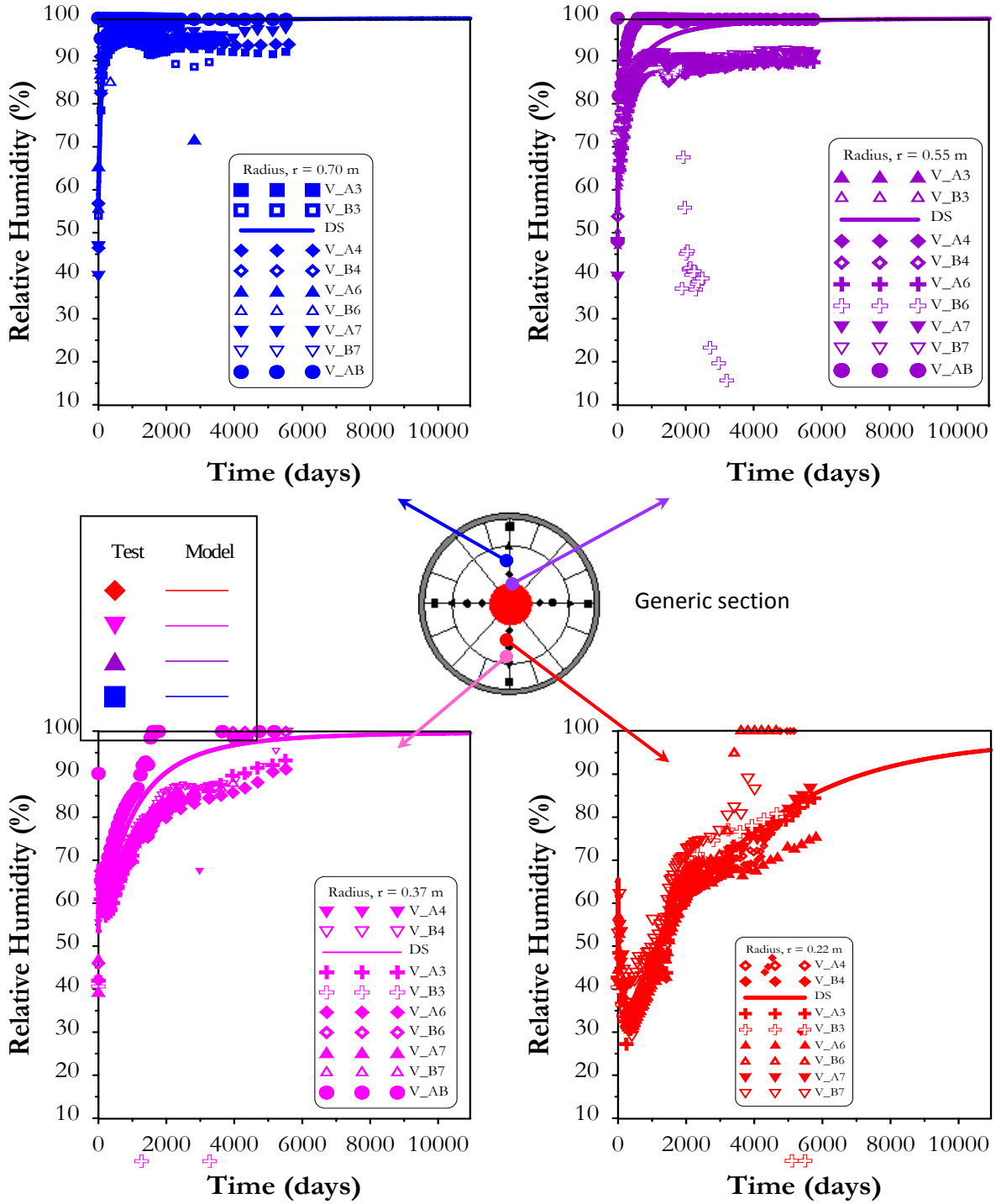

Figure 81. Evolution of relative humidity in the mock-up test, for all the instrumented Sections at the four different radii studied. Observed versus computed values (DS model) for long term predictions up to 10950 days.

5. SUMMARY AND CONCLUSIONS

In this report, the main activities related to the coupled THM analysis performed in relation to the FEBEX mock up test and of the long-term infiltration tests performed by CIEMAT in the framework of the PEBS project have been reported. Particular attention has been placed to the identification of relevant phenomena and processes that control the thermo-hydraulic-mechanical (THM) behaviour of the engineered clay barrier.

The 'OBC' models was formulated using the conventional THM formulation for a single porosity medium, in which all of the processes and couplings deemed relevant were considered. The comprehensive laboratory works carried out in the context of the FEBEX and NF-PRO projects have allowed the identification of the main model parameters required for this conventional THM model. However, the results obtained cannot be considered as totally satisfactory, because the simulation overpredicts the hydration rate of the barrier and thermal gradient infiltration cell during the later stages of the test. Comparing experimental data versus model results, a slowing down in the rate of hydration of the test was observed. Water vapour escaping form the experimental setup could be a contributing factor in this hydration slowing down but it is unlikely to provide a full explanation for the observations especially in the case of the mock up test. Changes in the conventional constitutive laws used or in the parameters adopted could not reproduce accurately the test evolution (e.g. Sanchez, 2004).

It was considered possible that the conventional THM model may have some shortcomings when reproducing the barrier behaviour described above. Generally, the formulation considers a progressive increment of the hydraulic conductivity as saturation progresses, especially due to the increment of relative permeability. However, experimental evidence shows that the behaviour of expansive clays under hydration is more complex. The difficulties of the OBC model to obtain good agreement with experimental results in the infiltration cells and mock-up test might be attributed to the presence of other processes or phenomena, which were not contemplated in the original 'OBC' model. A series of developments were performed in order to incorporate in the analyses some additional phenomena that could explain the barrier behaviour. Three main cases have been considered: i) non-Darcy flow due to the existence of a threshold gradient; ii) presence of a thermo-osmotic flow; and iii) evolution of clay micro-fabric.

The three hypotheses (and a combined one) used in the resulting enhanced formulation are able to model reasonably accurately the hydration of the mock-up test at early and later stages. Although the PEBS project is not designed to establish experimentally the potential existence and effects of those three phenomena, the performance of THM modelling of the FEBEX mock-up test (16 years of observations) gives some useful information on the effects likely to be associated with each one of the individual hypotheses considered.

Numerical modelling has shown that each of these possibilities is capable of providing results in reasonable good agreement with observations. However, numerical analysis, on its own, is unable to identify with certainty which is the phenomenon (or combination of phenomena) underlying the observed slowing down of hydration. However, there are noticeable differences between the predictions of the different hypotheses for the longer-term situation. Therefore, availability of long-term observations of the mock-up test may help in identifying the relevant phenomena at the later stages of hydration.

ACKNOWLEDGMENT

The research leading to results presented in this report has received funding from the European Atomic Energy Community's Seventh Framework Programme (FP/7 2007-2011) under grant agreement 249681.

REFERENCES

Alonso, E., Gens, A. & Josa, A. (1990). "A constitutive model for partially saturated soils". *Géotechnique*, 40, 3, pp. 405-430.

Alonso, E., Vaunat, J. & Gens, A. (1999). "Modelling the mechanical behaviour of expansive clays". *Engineering Geology*, 54, pp. 173-183.

Batchelor, G:K: (1983). "Fluid Dynamics". *Cambridge University Press.*

Bear, J. (1972). "Dynamics of fluids in porous media". *Dover Edit.*, 164 pp.

CIEMAT Report, (2002). "19th Data Report Mock-Up test". *Informe 70-IMA-L-9-96. CIEMAT*. Madrid.

CODE_BRIGHT User's Manual (2014). *UPC Geomechanical Group*.

Cui, Y., Loiseau, C. & Delage, P. (2001). "Water transfer through a confined heavily compacted swelling soil". *Proc. 6th International Workshop on Key Issues in Waste Isolation Research, Paris*, pp. 43-60

Djeran, I. (1993). "Étude des duffusions thermique et hydraulique dans una argile soumise á un champ de température". *Sciences et techniques nucléaires rapport*. Commission des Communautés européennes, ISBN 1018-5593.

Dixon, D., Gray, M. & Hatiw. (1992). "Critical gradients and pressures in dense swelling clays". *Can. Geotech. Jnl*., 29, pp. 1113-1119.

Dixon, D., Graham, J. & Gray, M. (1999). "Hydraulic conductivity of clays in confined tests under low hydraulic gradients". *Can. Geotech. Jnl*., 36, pp. 815-825.

ENRESA (1997). "Reunión de urgencia para analizar incidencias durante la hidratación de la maqueta y decidir eventuales actuaciones". *Acta de Reunión 70-ST-C-9-27.* Madrid.

FEBEX Report (1998). "Preoperational Thermo-Hydro-Mechanical (THM) modelling of the 'mock-up' test". *Publicación Técnica Nº 10/98. ENRESA*. Madrid.

FEBEX Report (2000). "Full-scale engineered barriers experiment for a deep geological repository for high level radioactive waste in crystalline host rock". *Final project report.* EUR 19612 EN, European Commission, Brussels.

FEBEX II Report (2004). "Final report on thermo-hydro-mechanical laboratory tests". Deliverable D17/3. UPC-L-7-13.

Fernández, A. Mª. (2004). "Caracterización y modelización del agua intersticial de materiales arcillosos: Estudio de la bentonita de Cortijo de Archidona". *Phd Thesis*. Madrid. pp 559.

Gens, A. 1995. "Constitutive Laws". In *Modern issues in non-saturated soils, A. Gens P. Jouanna & B. Schrefler (ed.)*: Wien New York: Springer-Verlag. pp. 129-158.

Gens, A. & Alonso, E.E. (1992). "A framework for the behaviour of unsaturated expansive clays". *Can. Geotech. Jnl*., 29, pp. 1013-1032.

Gens, A., Garcia Molina, A, Olivella, S., Alonso, E.E. & Huertas, F. (1998). "Analysis of a full scale in-situ test simulating repository conditions". *Int. Jnl. Numer. Anal. Meth. Geomech*, Vol. 22, pp. 515- 548.

Gens, A., Sánchez, M. (2014), Formulation of a model suitable for long term predictions. Deliverable D3.5-2. PEBS project.

Gens, A., Olivella, S. (2001). "THM phenomena in saturated and unsaturated porous media". *Revue française de génie civil*, 5: 693-717.

Gens A., Sánchez, M., Guimarães, L. do N., Alonso, E.E., Lloret, A., Olivella, S., Villar, M.V., Huertas, F. (2009). "A full-scale in situ heating test for high-level nuclear waste disposal: observations, analysis and interpretation". *Geotechnique*, 59, 377-399

Guimaraes L., Gens A., Sánchez M., Olivella S. (2001). "Chemo-mechanical modelling of expansive materials". *6th International Workshop on Key Issues in Waste Isolation Research.* Paris.

Hansbo, S. (1960). "Consolidation of clay with special reference to influence of vertical sand drains". *Swedish Geotech. Inst. Proc.* Nº 18 Stockholm.

Huertas F, Farina P, Farias J, Garcia-Sineriz JL, Villar MV, Fernandez AM, Martin PL, Elorza FJ, Gens A, Sanchez M, Lloret A, Samper J, Martinez MA. (2006). Full-scale engineered barrier experiment. Updated Final Report, Technical Publication 05-0/2006, Enresa, Madrid.

Lloret, A. & Villar, M (2001). "Variation of the intrinsic permeability of expansive clays upon saturation". In *Clay Science for Engineering, Adachi & Fukue (ed.)*. Balkema Rotterdam; pp. 259-266.

Lloret, A., Villar, M.V., Sánchez, M., Gens, A., Pintado, X., & Alonso, E. (2003). "Mechanical behaviour of heavily compacted bentonite under high suction changes". *Géotechnique*, 53(1): 27-40

Martin P.L., Barcala J.M. (2005). "Large scale buffer material test: mock-up experiment at CIEMAT", *Engineering Geology*, 81(3): 298–316.

Martin, P.L., Villar, M., (1997). "Propiedades hidráulicas del geotextile utilizado en el ensayo de maqueta del proyecto FEBEX". Informe Técnico *ENRESA: 70-IMA-L-3-32.*

Mitchell, J. (1993). "Fundamentals of soil behaviour". *2nd ed. John Wiley & Sons*, 437 pp.

Neuzil, C. (1986). "Groundwater flow in low-permeability environments". *Water resources research*, Vol 22, Nº 8, pp. 1163-1195.

Olivella., S. (1995). "Non isothermal multiphase flow of brine and gas through saline media". Ph.D. Thesis, Universitat Politecnica de Catalunya, UPC.

Olivella, S., Carrera J., Gens, A. & Alonso, E.E. (1994). "Non-isothermal multiphase flow of brine and gas through saline media". *Transport in porous media*, 15, pp. 271-293.

Olivella, S., Gens, A., Carrera, J. & Alonso, E.E. (1996). "Numerical formulation for a simulator (CODE-BRIGHT) for the coupled analysis of saline media". *Engineering Computations*, 13, 7, pp. 87-112.

Pintado, X. (2002). "Caracterización del comportamiento termo-hidro-mecánico de arcillas expansivas". *Phd Thesis*, Geotechnical Engineering Department, Technical University of Catalunya, Spain.

Pollock, D.W. (1986). “Simulation of fluid flow and energy transport processes associated with high-level radioactive waste disposal in unsaturated alluvium”. Water resource research Vol. 22 (5), pp. 765-775.

Pousada, E. (1984). “Deformabilidad de arcillas expansivas bajo succión controlada”. *PhD Thesis, Technical University of Madrid, Spain.*

Russell, A., & Swartzendruber, D. (1971). “Flux-gradient relationship for saturated flow of water through mixtures of sand, silt and clay”. *Sols Sci. Soc. Amer. Proc.* 35, pp. 21-26.

Sánchez, M. (2004). “Thermo-Hydro-Mechanical coupled analysis in low permeability media”. *PhD Thesis, Technical University of Catalonia, Spain.*

Sánchez, M.; Gens, A., Guimarães, L., & Olivella. S. (2005). “A double structure generalized plasticity model for expansive materials”. *Int. Jnl. Numer. Anal. Meth. Geomech.* 29: 751-787.

Sánchez, M., Gens, A., Olivella, S. (2012). “THM analysis of a large scale heating test incorporating material fabric changes” *International Journal Numerical and Analytical Methods in Geomechanics*, 36: 391-421.

Soler, J. (1999). “Coupled transport phenomena in the opalinus clay: implications for radionuclide transport”. Paul Scherrer Institut Nº 99-07- ISSN 1019-0643.

Soler, J.M. (2001). “The effect of coupled transport phenomena in the Opalinus Clay and implications for radionuclide transport”. *Journal of Contaminant Hydrology*, 53, 63–84.

van Genuchten, R. (1978). “Calculating the unsaturated hydraulic permeability conductivity with a new closed-form analytical model”. *Water Resource Research*. 37(11), pp. 21-28.

Villar, M.V. (2000). “Thermo-hydro-mechanical characterization of Cabo de Gata Bentonite (in Spanish)”. *Ph. D. Thesis*, Complutense University, Madrid.

Villar, M.V. & Cuevas, J. (1996). “Caracterización geoquímica de bentonite compactada. Efectos producidos por flujo termo-hidráulico”. *Informe Técnico 70 IMA-M-0-02.*

Villar, M. V., Gómez-Espina, R. (2009). Report on thermo-hydro-mechanical laboratory tests performed by CIEMAT on FEBEX bentonite 2004-2008, Madrid, pp. 67.

Villar, M. V., Martín, P. L. , Bárcena, I., García-Siñeriz, J.L., Gómez-Espina, R., and Lloret, A. (2012). Long-term experimental evidences of saturation of compacted bentonite under repository conditions. *Engineering Geology*, 149-150, 57-69.

Villar M.V., Sánchez, M., Gens, A. (2008). “Behaviour of a bentonite barrier in the laboratory: Experimental results up to 8 years and numerical simulation”. *Physics and Chemistry of the Earth*, 33, S476-S485.

APPENDIX

Thermal Problem. Complementary constitutive laws and parameters

The internal energy for the medium is computed assuming that it is additive in relation to the various phases. Therefore, the following expression has been used:

$$E = E_s \rho_s \left(1-\phi\right) + E_l \rho_l S_l \phi + E_g \rho_g S_g \phi \tag{A.1}$$

where E_s, E_l and E_g are the specific internal energies corresponding to each phase, i.e., the internal energy per unit mass of phase. ρ_s, ρ_l, ρ_g, are the densities of the three phases, ϕ is the porosity and S_g is the gas fraction with respect to the pore volume.

The gas phase energy is generally expressed as:

$$E_g \rho_g = \left(E_g^w \omega_g^w + E_g^a \omega_g^a \right) \rho_g = E_g^w \theta_g^w + E_g^a \theta_g^a \tag{A.2}$$

where E^w_g and E^a_g are the specific internal energies of species (respectively water and air), that is, internal energy per unit of mass of species. ω^w_g and ω^a_g are the mass fraction of water and air species in gas phase, respectively. This additive decomposition is admissible for the gaseous phase in the assumption of a mixture of gasses. It is not so obvious that the same decomposition is also valid for the liquid phase, however the same assumption will be made since the significance of the internal energy of dissolved air is small:

$$E_l \rho_l = \left(E_l^w \omega_l^w + E_g^a \omega_l^a \right) \rho_l = E_l^w \theta_l^w + E_g^a \theta_l^a \tag{A.3}$$

The values of the specific internal energies for the individual species are (Batchelor, 1983; and Pollock, 1983): E^w_l =4180.0 $(T\text{-}T_0)$ J/kg; E^w_g =2.5e^6+1900.0 $(T\text{-}T_0)$ J/kg; E^a_g =1006.0 $(T\text{-}T_0)$ J/kg and E^a_g =1006.0 $(T\text{-}T_0)$ J/kg.

It can be noted that the specific internal energy of the vapour (water in gas phase) contains an additional term that represents the latent heat in vapour. The thermal consequences of evaporation/condensation are therefore taken into account in a straightforward way.

Finally, the law reported in Villar & Cuevas (1996) has been adopted for the internal energy per unit mass of solid phase. This expression is given by:

$$E_s = E_s^o T + c_p T^2 \tag{A.4}$$

where E^0_s = 732.52 and c_p =1.38 (FEBEX Report, 1998). For the steel the values adopted for these parameters are E^0_s = 480 and c_p =0 (Sears & Zemansky, 1966).

Barcelona Basic Model BBM

A detailed description of the Barcelona Basic Model (BBM) model can be found in Alonso et al., (1990) and Gens (1995). Here the more relevant equations used in this work are presented. The BBM yield surface (F_{LC}) is given by Equation (21) and the plastic potential (G) is expressed as:

$$G = \alpha 3J^2 - \left[\frac{g(\theta)}{g(-30^o)} \right]^2 M^2 \left(p + p_s \right) \left(p_0 - p \right) = 0 \tag{A.5}$$

where α is determined from the condition that the flow rule predicts zero lateral strains in a K_0 stress path (Alonso et al., 1990).

The dependence of shear strength on suction and temperature is expressed as:

$$p_s = -k s e^{-\rho \Delta T} \tag{A.6}$$

where k and ρ are model parameters and ΔT is the temperature increment, respect to the reference temperature T_o.

The equation that defines the set of yield p_0 values for the associated suction (i.e. the family of *LC* curves on a *p*-*s* plane) is given by:

$$p_0 = p_c \left(\frac{p_{0T}^*}{p_c} \right)^{\frac{\lambda_{(0)} - \kappa}{\lambda_{(s)} - \kappa}} \tag{A.7}$$

where p_c is a reference stress, κ is the elastic stiffness parameter for changes in net mean stress, p_{0T}^* is the pre-consolidation net mean stress for saturated conditions and current temperature. $\lambda_{(s)}$ is the compressibility parameter for changes in net mean stress for virgin states of the soil, the dependence of which with respect to the suction is expressed as:

$$\lambda_{(s)} = \lambda_{(0)} \left[r + (1 - r) e^{-\zeta s} \right] \tag{A.8}$$

where r is a parameter that defines the maximum soil stiffness and ζ is the parameter that controls the rate of increase of soil stiffness with suction.

In order to identify a single yield curve from (A.7), it is necessary to specify the pre-consolidation net stress for saturated conditions p_{0T}^*, which may be viewed as the hardening parameter of the BBM model. According to Gens (1995), the thermal effect has been included considering a dependence of the hardening parameter on temperature, as follows:

$$p_{0T}^* = p_0^* + 2\left(\alpha_1 \Delta T + \alpha_3 \Delta T \left| \Delta T \right| \right) \tag{A.9}$$

where α_1 and α_3 are model parameters.

The expressions of the elasto-plastic tensors that define the small strain-stress relations are presented in Sánchez (2004) and Sánchez et al. (2005). Here the elastic tensor is presented only, which is evaluated as follows:

$$\mathbf{D}_e = \begin{bmatrix} K + \frac{4}{3}G_t & K - \frac{2}{3}G_t & K - \frac{2}{3}G_t & 0 & 0 & 0 \\ & K + \frac{4}{3}G_t & K - \frac{2}{3}G_t & 0 & 0 & 0 \\ & & K + \frac{4}{3}G_t & 0 & 0 & 0 \\ & & & G_t & 0 & 0 \\ symm & & & & G_t & 0 \\ & & & & & G_t \end{bmatrix} \tag{A.10}$$

where K is the global bulk modulus and G_t is the shear modulus. The macrostructural bulk modulus for changes in mean stress is computed as:

$$K = \frac{(1 + e)}{\kappa} p \tag{A.11}$$

The shear modulus G_t can be obtained from a linear elastic model with constant Poisson's coefficient:

$$G_t = \frac{3(1-2\mu)K}{2(1+\mu)} \tag{A.12}$$

where μ is the Poisson's coefficient.

The macrostructural bulk modulus for changes in suction has been computed considering the following law:

$$K_s = \frac{(1+e)(s+p_{atm})}{\kappa_s} \tag{A.13}$$

Finally the macrostructural bulk modulus for changes in temperature is evaluated through the expression (Gens, 1995):

$$K_T = \frac{1}{(\alpha_0 + 2\alpha_2 \Delta T)} \tag{A.14}$$

The stress invariants are defined as:

$$p = \frac{1}{3}(\sigma_x + \sigma_y + \sigma_z) \tag{A.15}$$

$$J^2 = 0.5 \ \ \text{trace}(\mathbf{s}^2) \tag{A.16}$$

$$\theta = -\frac{1}{3}\sin^{-1}\left(1.5\sqrt{3}\ \det \mathbf{s} / J^3\right) \tag{A.17}$$

$$\mathbf{s} = \boldsymbol{\sigma} - p\mathbf{I} \tag{A.18}$$

$$\boldsymbol{\sigma} = \boldsymbol{\sigma}_t - \mathbf{I}p_f \tag{A.19}$$

where:

$p_f = p_g$ *if* $p_g > p_l$; otherwise $p_f = p_l$ (A.20)

$\boldsymbol{\sigma}_t$ is the total stress vector and **I** is the identity tensor.